Université de Neuchâtel unine

Measurement of the linewidth enhancement factor of singlemode room temperature continuous wave quantum cascade lasers

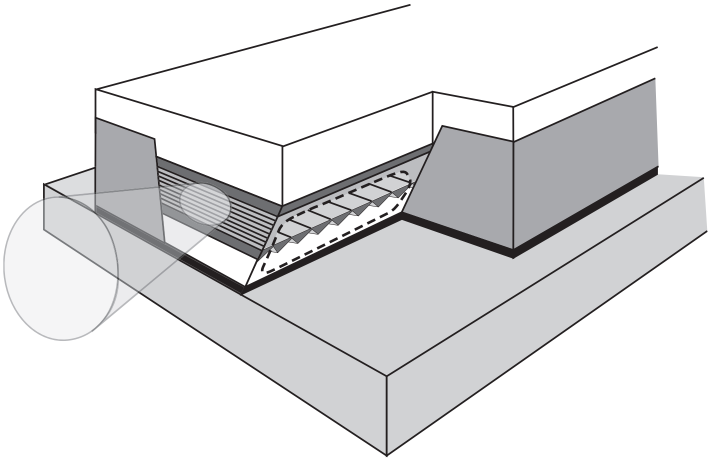

THESE

présentée à la Faculté des Sciences de l'Université de Neuchâtel
pour obtenir le grade de docteur ès sciences

par

Thierry Aellen

Neuchâtel, mai 2008

Université
de Neuchâtel unine

Measurement of the linewidth enhancement factor of singlemode room temperature continuous wave quantum cascade lasers

THESE

présentée à la Faculté des Sciences de l'Université de Neuchâtel
pour obtenir le grade de docteur ès sciences

par

Thierry Aellen

Neuchâtel, mai 2008

UNIVERSITÉ DE
NEUCHÂTEL

Faculté des sciences
Secrétariat-décanat de Faculté
Rue Emile-Argand 11
2000 Neuchâtel - Suisse
Tél: + 41 (0)32 718 2100
E-mail: secretariat.sciences@unine.ch

IMPRIMATUR POUR THESE DE DOCTORAT

La Faculté des sciences de l'Université de Neuchâtel autorise l'impression de la présente thèse soutenue par

Monsieur Thierry Yan AELLEN

Titre: Measurement of the linewidth enhancement factor of single-mode room temperature continuous wave quantum cascade lasers

sur le rapport des membres du jury:

- Prof. Philipp Aebi, Université de Neuchâtel, directeur de thèse
- Prof. Jérôme Faist, ETH Zürich
- Dr Daniel Hofstetter, Université de Neuchâtel

Neuchâtel, le 16 mai 2013

Le Doyen, Prof. P. Kropf

To my parents

Abstract

The invention of the laser source in 1960 has led to a wide range of applications showing a widespread impact in every aspect of our today life, including for example hospital, factory or simply at home. In particular, recent developments originating from the compact, highly efficient and common semiconductor lasers that are simply supplied by an electrical current. The diode coherent light sources are characterized by the fact that their constituent semiconductor materials define their emitted wavelength, or colour for visible light. For the long-wavelength range, i.e. in the mid-infrared spectra, lead-salt semiconductor crystals are the standard material used. Another approach that differs in a fundamental way from the diode laser one, consists to engineer the emission wavelength by a multiple quantum wells design achieved through nanoscale layer alternation of two different semiconductor materials. Demonstrated in 1994, this type of optical emitter called intersubband, unipolar or quantum cascade laser is the subject of this work. The names are coming from the cascade design of the unipolar optical gain media engineered in a way so that an electron (matter) is injected and recycled in a periodic multiple quantum wells stack and produce as much photons (light) as the repeated stacks in the structure. The laser transition in one of the stacks is achieved in the called active region, i.e. where the electron population inversion occurs, ensures by the electron reduce lifetime on the lower radiative state. Two of different scattering relaxation mechanisms for electronic lifetime reduction are presented, the optical phonon resonance and the tunneling trough superlattice. A correlation between the doping, i.e. the amount of electrons in the reservoir following the active regions in a stack, and the performance of quantum cascade lasers is also exposed.

An important chapter in the history of information in modern society consists to the de-

velopment of telecommunication based on optical fibre and semiconductor laser technologies. One of the essential building blocks for the lightwave communication progress was the first continuous-wave room-temperature laser diode operation in the near-infrared spectrum demonstrated in 1970. Since then, the advance of other semiconductor laser sources with different light spectra to expand this technology for suitable nowadays applications is strongly related to their room-temperature continuous-wave operation. As for example, the recently developed blue laser diode in 1996 dedicated to the information storage and processing systems (compact audio disks, video disks, optical data disks, laser printers, laser bar code scanners, etc.). This report contains the achievement of a distributed feedback quantum cascade laser operating at room temperature in continuous-wave operation. This result is based on the specific laser device fabrication with an embedded active region associated to a flip chip mounting to increase the Joule heating dissipation induced by the driving current. The light feedback in the laser cavity is ensured by the addition of a grating close to the laser gain media that acting as a filter for a single-frequency emission.

For a free-running laser, the single-frequency emission is not strictly a monochromatic Dirac delta function. It is limited by the noise associated to quantum processes leading to a certain fundamental spectral linewidth, first derived by Schawlow and Townes. This phenomenon can be interpreted by the presence of the spontaneous emission in the laser modes that perturbing the existing phase with random phases in the laser cavity. It was then later introduced by Henry that the optical gain and refractive index change related to the carrier density variation could increase the Shawlow-Townes linewidth. Note that the optical gain is related to the refractive index, and vice-versa (Kramers-Kronig dispersion relations). This linewidth enhancement factor is called Henry factor or alpha factor. Unlike a semiconductor diode laser, an intersubband laser shows a low Henry factor and is in that respect closer to a gas laser characteristic based on discrete atomic transitions. The quantum cascade laser alpha-factor is specific to the narrow and essentially symmetric gain spectrum associated to its lasing transition occurring between parallel subbands, or nearly parallel when restricted by the nonparabolicity. The direct measurement of the low Henry factor by heterodyning of an amplitude-modulated quantum cascade is performed in this study.

Although the employment of this single frequency laser is suited to free space optical communication while two atmosphere transmission windows in mid-infrared exist, the interest of this source is mainly sensing oriented. The fundamental vibrational and rotational molecule modes of material occur in the mid-infrared region and similar to a fingerprint can be used as an identification by the direct precise atomic absorption of the discrete light coming trough a distributed feedback laser. Note that the appearance of semiconductor lasers made a revolution in spectroscopy, especially for Raman and photoacoustic technics, this later is especially used to increase the sensitivity of direct detection.

Résumé

L'invention des sources lasers en 1960 à conduit à un bon nombre d'applications qui ont un impact répandu dans tous les aspects de notre votre vie actuelle, citons notamment l'exemple des hôpitaux, de l'industrie ou simplement dans notre lieu de vie. Les derniers développements sont en particulier issus des compacts, très efficace et populaires lasers semiconducteurs qui sont simplement alimentés par un courant électrique. Les sources diodes cohérentes sont caractérisées par le fait que la matière semiconductrice qui les qui compose définie leur longueur d'onde d'émission, ou dite couleur pour la lumière visible. Pour les grandes longueurs d'onde, i.e. dans le spectre infrarouge, les cristaux semiconducteurs à base de sel de plomb constituent le matériau standard utilisé. Une autre possibilité, qui se différencie fondamentalement de celle des diodes lasers, consiste à recourir à l'ingénierie pour définir la longueur d'onde d'émission par le design de multiples puits quantiques obtenus grâce à l'alternation de couches nanométriques de deux matériaux semiconducteurs différents. Démontré en 1994, ce type de d'émetteur optique appelé laser à cascade quantique, intersousbande ou unipolaire constitue le sujet de ce travail. Ces appellations sont inhérentes au design en cascade du milieu dans lequel le gain optique unipolaire est réalisé de telle manière qu'un électron (matière) est injecté et recyclé dans une répétition priodique de plusieurs puits quantiques ou il produit autant de photons (lumière) que de répétitions dans la structure. La transition laser dans une des répétitions se produit dans la zone dite active, i.e. l'endroit où l'invesion de population se manifeste, assurée par la faible durée de vie de l'électron sur l'état final de la transition radiative. Deux des différents mécanismes de relaxation par diffusion afin de réduire le temps de vie électronique seront présentés, la relaxation par résonnance avec un phonon optique et l'effet tunnel dans un super-réseaux.

Une corrélation entre le dopage, i.e. le nombre d'électrons présents dans le réservoir suivant la zone active d'une répétition, et les performances des lasers à cascade quantique est aussi décrits.

Un chapitre important de l'histoire de l'information dans la société moderne repose sur le développement des télécommunications à base des technologies que sont la fibre optique et le laser semiconducteur. Un des piliers essentiels relatant du progrès de la communication lumineuse a été le premier fonctionnement d'une diode laser en mode continu à température ambiante dans le spectre du proche infrarouge démontré en 1970. Depuis lors, l'avancée des autres sources lasers semiconductrices émettant dans les différent spectres lumineux afin d'étendre cette technologie aux applications souhaitables actuellement est éminemment lié à leur opération en continu à température ambiante. Comme exemple, le développement récent d'une diode laser bleue en 1996 dédiée pour le stockage de l'information et les systèmes de traitement (disque compact audio, disque vidéo, disque optique informatique, imprimante laser, scanner à code barres laser, etc.). Cet ouvrage comporte la réalisation d'un laser à cascade quantique à contre-réaction répartie opérant à température ambiante en mode continu. Ce résultat est basé sur la fabrication spécifique de l'élément laser comprenant une région active intégrée allié au montage à puce retournée pour augmenter la dissipation de l'effet Joule suscité par le courant de pilotage. La contre-réaction de la lumière dans la cavité laser est garantie par l'addition d'un réseau proche de la zone de gain du laser qui agit comme un filtre pour une émission à fréquence unique.

Pour un laser non stabilisé, l'émission à fréquence unique n'est pas rigoureusement une fonction delta de Dirac monochromatique. Elle est limitée par le bruit associé aux processus quantiques qui produit un élargissement spectral fondamental, établi en premier lieu par Shawlow and Townes. Ce phénomène peut tre interprété comme la présence de l'émission spontanée dans les modes lasers, perturbant la phase existante dans la cavité laser par des phases aléatoires. Introduit ultérieurement par Henry, le changement de gain optique et d'indice de réfraction induit par la variation de la densité de porteur peut augmenter l'élargissement de la largeur de ligne de Shawlow-Towns. A noter que le gain optique est en relation avec l'indice de réfraction et vice-versa (relations de Kramers-Kronig). Ce facteur d'élargissement est appelé le facteur de Henry ou facteur alpha. Contrairement à la diode laser semiconductrice, le laser intersousbande possède un faible facteur de Henry et est à ce titre proche des caractéristiques d'un laser à gaz basées sur une transition atomique discrète. Le facteur alpha d'un laser à cascade quantique est représentatif de son gain spectral étroit et est essentiellement symétrique relatif à sa transition laser qui s'établit entre les sousbandes parallèles, ou quasi parallèles lorsqu'elles sont régies par la non-parabolicité. La mesure directe par détection hétérodyne du faible facteur de Henry d'un laser à cascade quantique modulé en amplitude est réalis ée dans cette étude.

Bien que l'emploi de ce laser à fréquence unique est approprié pour la communication optique dans l'air libre puisque deux fenêtres de transmission dans l'atmosphère se situent dans le moyen infrarouge, l'intérêt évident de cette source se situe dans le domaine des senseurs. Les modes fondamentaux de vibration et de translation moléculaire d'un matériau ont lieu dans la région du moyen infrarouge et semblable à une empreinte digitale peuvent être utilisés pour l'identification par l'absorption atomique précise directe par de la lumière discrète provenant d'un laser à contre réaction répartie. Il est à noté que l'apparition des lasers semiconducteurs ont suscité une révolution dans la spectroscopie, spécialement pour les techniques Raman et photo-acoustique, cette dernière étant spécifiquement utilisée pour augmenter la sensibilité de la détection direct.

Contents

List of Figures

List of acronyms used throughout this work

AM	Amplitude modulation
APD	Avalanche photodiode
BH	Buried heterostructure
DFB	Distributed feedback
DTGS	Deuterated triglycine sulphate
CW	Continuous-wave
FM	Frequency modulation
FP	Fabry-Perot
FTIR	Fourier Transform Infrared Spectrometer
FWHM	Full Width at Half Maximum
MBE	Molecular Beam Epitaxy
MCT	Mercury-cadmium-telluride
MIR	Mid-infrared
ML	Multilayer
MOCVD	Metalorganic chemical vapor deposition
MOVPE	Metalorganic vapour-phase epitaxy
NDR	Negative Differential Resistance
PBS	Polarizing beamsplitter
PECVD	Plasma-enhanced chemical vapor deposition
QW	Quantum Well
QC	Quantum Cascade
QCL	Quantum Cascade Laser
SEM	Scanning electron microscopy
SMSR	Sidemode suppression ratio
STM	Scanning tunneling microscope
TEM	Transmission Electronic Microscope
α	Henry factor
α_m	Mirror losses
α_{tot}	Total losses
α_w	Waveguide losses
g	Gain coefficient
Γ	Overlap factor
j	Current density
j_{th}	Threshold current density
j_{ndr}	Maximum current density

Chapter 1

Introduction

1.1 Motivation

The mid-infrared region of the electromagnetic spectrum, covering the wavelength range from 3 to 20 μm, is sometimes referred as underdeveloped because of its lack of convenient coherent optical sources. For comparison, in the visible (400 to 800 nm) or the near-infrared spectral range (800 nm to 3 μm), interband semiconductor lasers are now produced very economically with room temperature continuous wave (CW) output powers of tens of milliwatts. These devices have become key components in CD and DVD players or in fiber-optic communication systems, respectively.

Nevertheless, there is a strong interest to develop sources in the mid-infrared range because molecules exhibit strong fundamental vibrational and rotational absorption bands in this region. The identification and quantification of particular molecular species has led to a wide range of useful spectroscopic application fields such as medical diagnostics, environmental sensing, process control or drug/explosive/contaminants detection.

In the range of 3 to 30 μm, available emitter technology based on leadsalt semiconductors was limited in optical power and CW operation temperature [1]. Most other existing technologies are so far limited to wavelengths below 4 μm for instance. There are type I or II tunable antimony-based quantum-well diode lasers, based on an interband cascade principle [2, 3] or no cascade design [4] and two types of parametric frequency conversion of near-IR lasers using a non linear crystal (optical parametric oscillator and difference frequency generation based sources). On the other hand, Gas lasers, such as the CO_2 laser which has emission wavelength bands around 9.6 and 10.6 μm, can be used in CW operation with several hundreds of watts but for discrete spectral lines only.

In contrast to diode lasers, the quantum cascade (QC) laser - an intersubband semiconductor laser - can be tailored within a wide wavelength emission range of 3.4 to 24 μm and is not limited in operation temperature (details in following Sections). This type of laser is now able to operate single-mode in CW at room temperature with high output powers (>50 mW) and narrow linewidths (few megahertz without stabilization). Since trace gas detection systems are characterized by their sensitivity, selectivity, fast response time and compactness, such performances of QC lasers are especially attractive. Up to now, systems using QC lasers, in particular by F.K. Tittel and colleagues, have been used to detect gas concentrations in the parts-per-billion range [5]. The CW operation and high optical power operation are also suitable for other application fields, such as counter-measures or free-space optical data transmission communication systems exploiting atmospherical windows between 3-5 μm and 8-12μm.

In the following section, a brief introduction to intersubband transitions and QC laser engineering and performances is presented. The last section is devoted to the structure of the manuscript and will describe the different parts of the technological work that was carried out at the University of Neuchâtel.

1.2 Intersubband transition

After a brief introduction to interband lasers and their functioning, intersubband transitions in heterostructures are described and advantages of lasers based on this type of transition are discussed.

The suggestion that semiconductors could be used as laser material appears in the early 1960s. This early work resulted in the demonstration of laser action across gallium arsenide (GaAs) p-n homojunctions by current injection at a temperature of 77K. In this laser, emitted photons are produced by electron-hole recombination across the semiconductor bandgap. Because of the two types of carriers and the resulting rectifying behavior, these lasers are also called diode lasers. Toward the end of the 1960s, double heterostructure laser diodes were developed [6]. They consist of a semiconductor with a narrow energy bandgap which is sandwiched between two layers with a wider energy bandgap semiconductor to form a quantum well. Thanks to the quantum well, this structure exhibits a lower threshold-current density compared to bulk semiconductor lasers, mainly due to the confinement of photons and the reduced inverted volume of charge carriers. The confinement creates new subbands inside the energy bands and carriers occupy discrete energy levels in the quantum well as shown in Fig. 1.1 a). The corresponding energy subbands have dispersion relations with opposite curvature (two -dimensional system, kinetic energy of free electron $\hbar^2 k^2/2m^*$). As a result, the gain spectrum is broad and asymmetric, limited by the step-like shape of the joint density of states and the population distribution given by the Fermi-Dirac statistics. The optical photon (radiative transition), relative to the bandgap separation, has a much larger energy than the energy of the phonon (non-radiative transitions). Due to the dominant radiative relaxation, the upper subband lifetime is quite long, namely about 1 ns. Nevertheless, the Auger recombination, a non-radiative transition which occurs between impurity states, becomes important when the temperature increases. An increase of this influence is observed for narrow bandgap material (Auger process is typically significant at around 50 degrees for 1.5 μm devices, 70 degrees at 1.3 μm, and $\geq$ 120 degrees for devices operating at 0.9 μm or less).

With the appearance of heterostructures, a new type of transition appears, namely the transition which occurs between the energy states in the same subband; it is also called intersubband transition. In contrast to interband transitions, different features are associated to this transition as illustrated in Fig. 1.1 b). The dispersion curves corresponding to the different energy states are nearly parallel, affected only by a small nonparabolicity (effective mass is a function of energy). The comparable curvatures lead to an atomic-like shape of the joint density of states (delta-like function when the broadening is neglected) and a relatively narrow and symmetric gain spectrum (Gain is described in Chapter 2). The dominant non-radiative process in intersubband transitions is the phonon scattering which has maximal efficiency for an energy separation between states corresponding to the phonon energy (resonance), but which occurs also between larger separations (lifetime is described in Chapter 2). This efficiency decreases the value of the upper state lifetime strongly to values on the order of 1 ps.

For emission wavelengths of $\lambda > 4$ μm, a laser based on intersubband transitions offers some advantages compared to an interband source. The operating temperature of the device can be increased since the phonon process is less sensitive to temperature than Auger effect (in spite of electron and hole comparable effective masses that reduce the Auger recombination, continuous operation of interband lead-salt lasers has not exceeded 223 K at 5 μm [1]). The emission wavelength can be chosen in a larger range by adjusting the thickness of the quantum well and thus the spacing of the states in the subband (not fixed by the bandgap energy). Only one type of carriers (unipolar) is involved in an intersubband transition, which means a higher device reliability (no damage due to electron-hole recombination at the facets). Lasing action in indirect-gap material is allowed because the bandgap does not influence transitions between subbands (semiconductors based on indirect-gap materials have a nearly zero radiative interband transition rate due to the complex interaction that involves at the same time both a phonon and a photon at a low phonon density). Additionally, a higher frequency modulation in the order of 100 GHz is theoretically possible without relaxation oscillation due to the shorter upper state lifetime (details in Chapter 2). Furthermore, a zero value of the linewidth enhancement factor is expected due to the symmetric shape of the gain spectrum (details in Chapter 2). As a result, the spectral linewidth is as narrow as predicted by the Shawlow-Townes formula and no chirp occurs for frequency modulation. Whether this statement is really true, will be one of the main questions of this thesis; it will be discussed in detail in the last chapter of the manuscript.

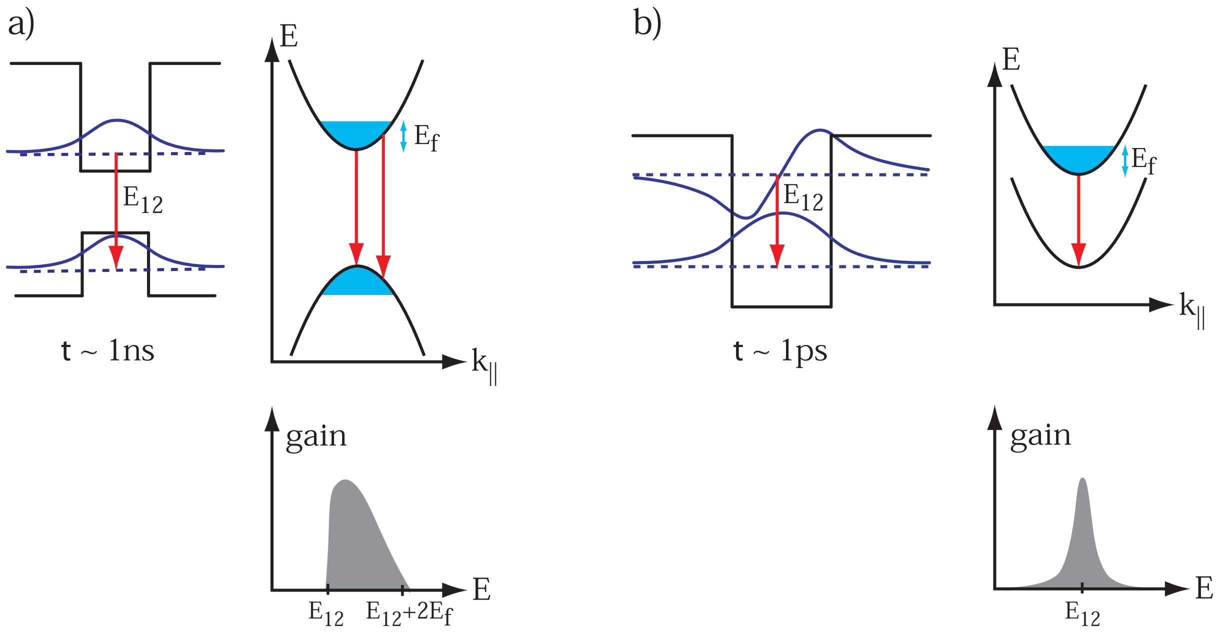

Figure 1.1: Real space band diagram, dispersion of the electronic subbands in k-space and joint density of state for a) interband and b) intersubband transitions.

1.3 QC laser design and materials

In 1972, the first proposal of light amplification using intersubband transitions has been published by R. F. Kazarinov and R. A. Suris [7, 8]. The design in this proposal is based on a strongly biased superlattice where the light emission is generated between two states in adjacent wells by a photon assisted tunneling process.

During the 1980s and in the early 1990s, the subject of intersubband transitions has seen intense theoretical [9, 10, 11, 12, 13, 14, 15] and experimental (absorption [16], in particular luminescence [17, 18]), activities.

In 1994, the first laser based on intersuband transitions, called quantum cascade (QC) laser, has been demonstrated by J. Faist and coworkers in the group of F. Capasso at Bell Laboratories [19]. The conduction band diagram of such a QC laser under a strong applied electric field is reported in Fig. 1.2. The structure consists of a repetition of one basic stage, called period. A period is composed by a gain region, where the photon assisted tunnelling transition occurs, and an injection/relaxation region, where the electron distribution is cooled down by a non-radiative phonon process, from where they are reinjected in the next period by resonant tunnelling. The population inversion, necessary to obtain stimulated emission and laser action, does not naturally occur in a subband and has to be engineered. A necessary condition of the population inversion is a longer non-radiative relaxation time in the upper than in the lower lasing state. In this design, this is ensured by an increase of the upper lasing state lifetime via a diagonal transition where the spatial overlap of the wavefunctions is decreased. In parallel, the lower state lifetime is shortened by efficient resonant phonon relaxation. This is achieved by the presence of a state below the lower lasing state with an energy spacing which corresponds to the phonon energy. The use of an injection/relaxation region is new in comparison with the first proposal. The latter helps for both the relaxation (prevention of backfilling of electrons into the lower radiative state) and the injection. Moreover, the injection/relaxation region is doped, acting as an electron reservoir and preventing the formation of space-charge domains. The cascaded geometry is an important feature of the structure, since the electron - which is recycled in the following periods - can in principle emit a number of photons corresponding to the number of periods in the structure. As a result, high power QC lasers can be obtained due to the high internal quantum efficiency. In contrast, the applied voltage is also proportional to the number of periods and a trade-off between electrical power consumption and high optical power emission has to be found. The successful achievement of quantum cascade laser heterostructures is tightly related to a sophisticated growth technique based on molecular beam epitaxy (MBE) developed by A. Y. Cho at Bell laboratories[20]. This technique is based on the reaction of thermal atomic beams, generated from heated effusion cells, on a heated crystalline surface in ultra high vacuum environment ($<10^{-10}$ mbar). The thin single-crystal epitaxial layer deposition leads to controlled heterostucture interfaces (less than one monolayer interfacial roughness).

After the demonstration of the QC laser based on a diagonal transition (also called 3 quantum-well design), design engineering of QC lasers showed an impressive development. Devices based on a population inversion induced by a superlattice [21](multi-QW), a chirped supperlattice [22], a vertical transition [23] (2 QW), and non-parabolicity [24] (1 QW) have been demonstrated. In 2001, a new design has been presented, called two-phonon resonance design [25] (4 QW). The specificity of this structure is its optimization for high temperature operation with the introduction of two states separated each by an optical phonon energy below the lower state of the laser transition (more details in Chapter 3). This double resonance strongly reduced the lower state population and the thermal backfilling. Another solution was to replace the ladder of two states by a miniband [26](more details in Chapter 4). This so-called bound-to-continuum approach offers the advantage of a broad gain emission.

Until now, QC laser structures based on heterostructures composed in InGaAs/InAlAs materials and grown on an InP substrate were discussed. With these materials, laser emission at wavelengths between 3.4 [27] and 24 μm [28] has been reported. Performances of long wavelength lasers are limited by losses due to free carrier absorption that increase quadratically with the wavelength. At the shorter wavelength side, the limitation comes from the electron escape to the continuum by tunnelling through the barriers. In order to obtain shorter wavelength emission ($\lambda \leq 6$ μm), the conduction band discontinuity must be increased by the use of strain-compensated materials ($0.52 \rightarrow 0.71$ eV for 1 percent compressive/tensile strained material) where the compressive strain in the InGaAs is compensated by the tensile strain in the AlInAs.

QC lasers based on other III-V compounds with different band discontinuity were also investigated. In 1998, laser action in the GaAs/AlGaAs material system has been demonstrated by C. Sirtori and coworkers [29]. This demonstration has shown both the independence of the QC laser concept from the material system used and the possibility to fabricate devices in one of the most advanced semiconductor materials. The wavelength emission range of lasers based on these materials is currently limited between 7.2 [30] and 23 μm [31] with lower performances than for InGaAs/AlGaAs based devices. However, due to its mature growth technology, the first demonstration of terahertz (THz) emission of a quantum cascade laser by A. Tredicucci and colleagues in collaboration with University of Cambridge in 2001 was based on GaAs/AlGaAs material [32]. As a result, the wavelength emission range of QC lasers is now extended to the far-infrared region, between 67 μm (4.4 THz) for the first laser demonstration to $\sim$ 190 μm [33] according to recent developments. These devices operate at cryogenic temperatures. This remarkable demonstration has shown that QC lasers can even operate for transition energies lower than the phonon energy.

Lasing operation has also been demonstrated in InAs/AlSb material system [34] in 2003. This material is especially interesting for its large band discontinuity (2.1 eV) and its ability to emit at short wavelengths. Recently, operation at a wavelength of 3.1 μm up to 230 K [35] has been reported. In 2004, lasers based on InGaAs/AlAsSb material have also been realized [36]. The band offset of 1.6 eV is also well suited for short emission wavelengths. Room temperature operation at wavelengths of 3.9 μm [37] have been reported as well.

In this context, and based on the demonstration of intersubband absorption at 1.4 μm [38], a laser based on AlGaN/GaN material might further extend the short wavelength limit of QC structures. However, the growth of this material is very challenging due to the lack of lattice matched substrates and the fact that QC structures are very sensitive to interface roughness. An other interesting project is the achievement of a QC laser based on Si/SiGe materials to interconnect microelectronic and optoelectronic base materials. Intersubband electroluminescence of this type of structure has already been demonstrated in the mid-infrared [39] and far-infrared region [40]. The realization of a QC laser based on an indirect-gap semiconductor and hole carriers would be the demonstration that QC structures are truly independent from the material gap and type of carriers.

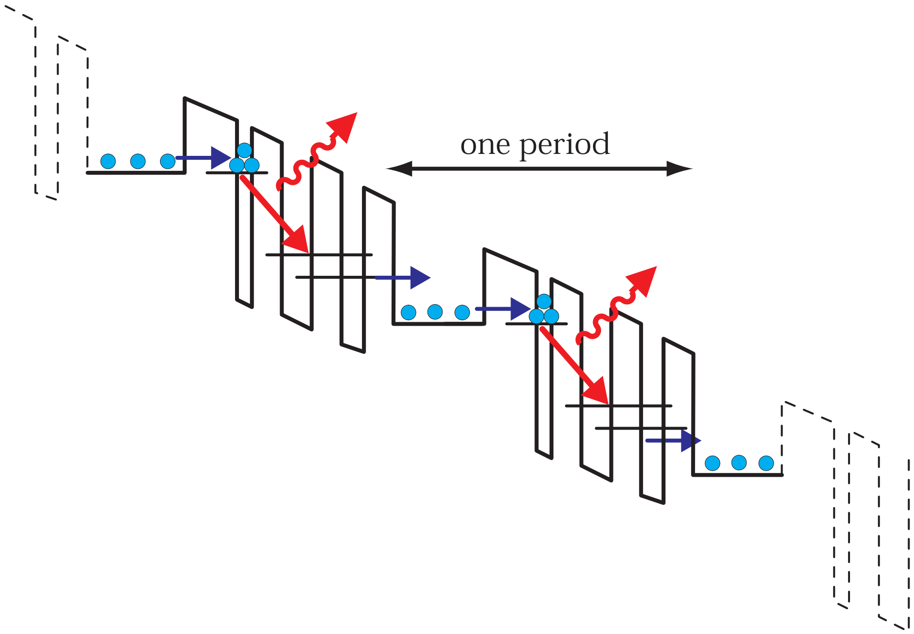

Figure 1.2: Principle of cascading: an electron cascades down emitting photons at each step.

1.4 State-of-the-art in 2005

1.4.1 CW operation

In this section, we will talk briefly about some important historical aspect of CW operated QC lasers. In order to introduce the main results of this thesis, we will outline the development of these devices until 2005. The theoretical and experimental activities in this field is still intensive as its interest for applications with more and more systems based on QC lasers.

In 2002, the first CW operated QC laser at room temperature and a wavelength of 9 μm has been demonstrated by M. Beck and colleagues [41] giving promising perspectives of compact system implementation for sensitive trace gas analysis. This achievement was the result of several optimizations. First, the use of the two-phonon design that was studied for high temperature operation improved the gain region (based on this design, CW operation near room temperature on a Peltier cooler had already been reported with the help of a junction down mounting and facet coating [42]). A second step was the reduction of the waveguide losses by fabricating buried heterostructures. In this kind of device, the active region is surrounded by an insulating layer of InP, creating a low-loss lateral waveguide (details in Chapter 4). The following point was the increase of the heat dissipation by both the presence of the lateral InP layer and junction down mounting. Finally, the mirror losses were reduced by the deposition of high reflection coatings on both facets.

In 2003, CW operation on a Peltier cooler for shorter wavelength emission at 5.6 μm was demonstrated using similar optimizations [43]. This result was also the first demonstration of a high temperature operation QC laser based on strain-compensated materials. Room temperature operation has been achieved the same year by Yu and coworkers at a wavelength of 6 μm [44]. This improvement in high temperature operation is correlated to the fabrication of narrower ridges to reduce waveguide losses and the growth of a lower doped active region to decrease free carrier absorption. Instead of buried heterostructure fabrication, a thick electroplated gold layer around the laser ridges was used to simplify the device processing. Based on a similar technology, the Northwestern University group has subsequently demonstrated room temperature CW operation of QC lasers with high output powers ($>$ 100 mW) at wavelengths of 4.8 [45], 4.3 [46, 47], 5.3 [48], 4.0 [49], 9.5 [50], 3.8 [51] and 7.8 μm [52]. These results are also associated to an excellent material growth based on gas source MBE technology. Buried heterostructure devices were also fabricated resulting in the highest room temperature output power of 640 mW[46].

The growth by metalorganic vapor phase epitaxy (MOVPE) was also investigated. The first lasing action based on this growth technique has been demonstrated at Sheffield University[53, 54] in 2003. In 2005, Troccoli and colleagues from Agilent laboratories at Palo Alto achieved CW operation at room temperature with an optical power of 20 mW based on MOVPE growth [55]. They used narrow ridges and a buried heterostructure employing a lateral overgrowth with Fe-doped InP. The active region design used for this demonstration was based on a diagonal transition. Later, with devices based on a two-phonon design, operation at room temperature with high powers at 8.4 [56] (200 mW) and 5.3 μm[57] (40 mW) has been demonstrated. The MOVPE growth technique shows thus comparable performances to the best MBE results. Moreover, the MOVPE technique is promising for commercial production, mainly because of its single growth step capability, large growth rate for the cladding layer, and a facility for material change without perturbation of a high vacuum environment. However, the growth rate of the active region with MOVPE techniques is similar to the one obtained with MBE (~ 1 μm per hour).

An overview of the highest temperature operation of QC laser in the mid-infrared region both in pulsed and CW operation is presented in Fig. 1.3. To be complete, the best performances of far-infrared QC lasers are also reported. It is obvious that there exists a performance maximum around 5-10 μm.

QC lasers with an incorporated distributed feedback (DFB) grating are of particular interest to most high-resolution spectroscopy applications requiring tunable single-frequency light sources with a narrow linewidth (details in Chapter 5). Performances of this type of devices are usually comparable to the one of Fabry-Pérot lasers. Of course, one has to know precisely the refractive index of the material, the gain curve and the fabrication technology which requires several fabrication cycles. The development of these DFB-QC structures was investigated by the Bell Labs Group [58, 59, 60, 61, 62], TU Vienna [63, 64], the University of Neuchâtel [25, 65, 66], and recently Northwestern University [45, 67]. Recently, single-mode devices emitting CW at room temperature based on bound-to-continuum active region have been developed in collaboration between Alpes Lasers and University of Neuchâtel [68]. This collaboration has led to the demonstration of single-mode CW operation between 7.7 and 8.3 μm from devices fabricated from the same epilayer with different grating periods [69]. The Jet Propulsion Laboratory just chose one of these lasers for the 2009 Mars Science Laboratory mission to participate in the quest for determining whether Mars was ever habitable.

The selection of the single frequency by an external cavity is also an interesting development for expanding the wavelength tunability. Using such an approach, the tuning of a bound-to-continuum QC laser operating in CW over a record frequency span of 175 cm^{-1} around a center frequency of 1850 cm^{-1} has been reported [70]. Within this tuning range, the continuous power was always larger than 10 mW. Coarse tuning was achieved by rotating the grating; fine tuning involved changing of the cavity length and laser device temperature. This narrow linewidth, broadly tunable source is especially well suited for spectroscopy.

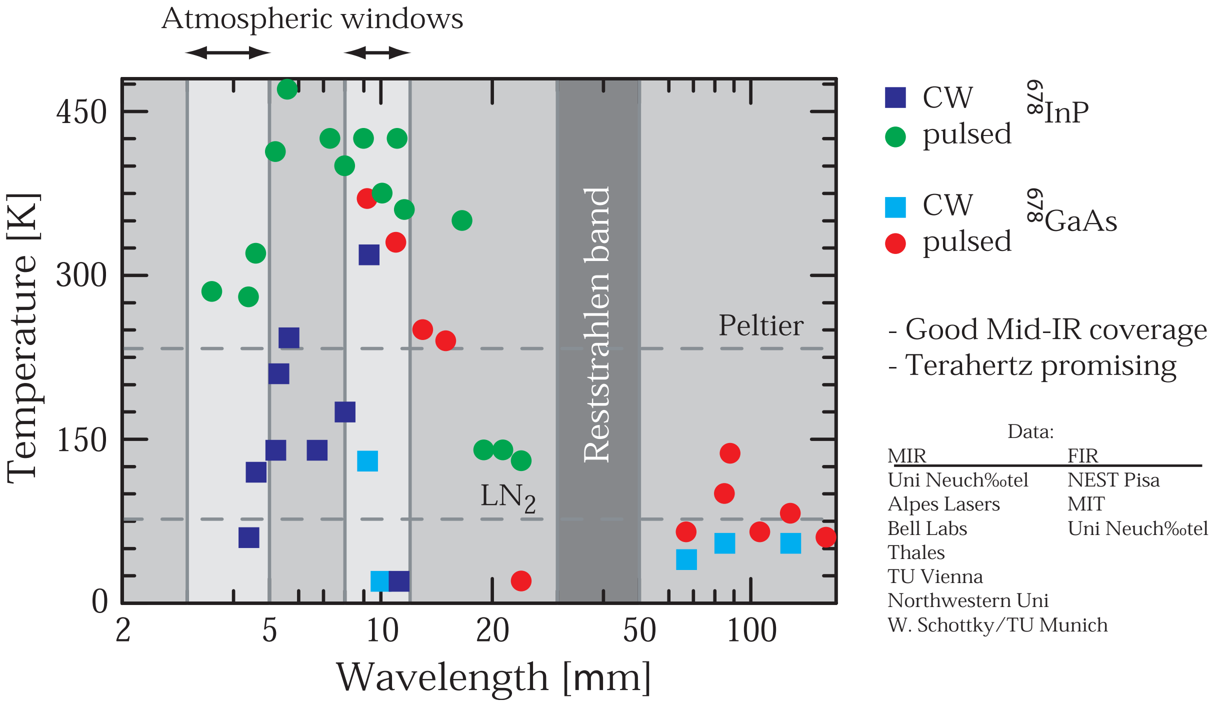

Figure 1.3: State of the art in 2005

1.4.2 Linewidth enhancement factor measurement

According to the Kramers-Kronig relations which predict no variation of the real part of the refractive index for a symmetric shape of the gain spectrum (see Chapter 2), a zero value of the linewidth enhancement factor for intersubband transitions is expected. Based on the sub-threshold gain curve measurement and its transformation (Kramers-Kronig) to obtain the real part of the refractive index, the first techniques to measure the linewidth enhancement factor are called indirect. For different measurements of the gain data, based on the Hakki-Paoli technique and the wavelength shift of the Fabry-Perot resonances with current, values of $\alpha = 0.1$ [71] and $\alpha =$ -0.5 [72, 73] were reported, respectively.

In this work, we propose a direct measurement of the linewidth enhancement factor based on the measurement of the laser chirp (optical frequency modulation added to the injected current modulation). The low measured value of $\alpha = 0.02 \pm 0.2$ achieved with this technique agrees with the first indirect measurements and the theoretical prediction.

Following this experiment, another direct measurement of the α parameter based on feedback self-mixing was demonstrated[74]. If the value is close to zero for currents just above threshold ($\alpha = 0.24$), a significant increase up to $\alpha = 2.6$ for higher pump parameters is reported. Due to a high sensitivity of the α parameter to temperature fluctuations and single mode frequency emission, this result should be confirmed by other measurement techniques to attribute it in an unambiguous way to QC laser characteristics.

1.5 Organization of the thesis

The objective of the present work is to develop QC laser sources for room temperature, CW, and single-mode operation for both applications and fundamental research, in particular measurement of the linewidth enhancement factor. In Chapter 2, a few theoretical aspects about the quantum physics of QC structures as well as an introduction to the α factor and the effect of chirp in high-frequency modulation are shown. The two-phonon resonance design, a structure optimized for high temperature operation, is presented in Chapter 3. The influence of the doping density on pulsed room temperature performances are discussed. The subject of Chapter 4 is the mode selectivity of distributed feedback QC lasers. In order to achieve single-mode CW operation at room temperature, the two-phonon resonance design is combined with a buried heterostructure waveguide for emission wavelength of 9.1 μm. The measurement of the spectral linewidth of a room temperature CW operated single mode distributed feedback laser based on a bound-to-continuum design is also performed. A high frequency setup for direct intensity modulation of QC lasers on a Peltier cooler is addressed in Chapter 5. In Chapter 6, the measurement of a low linewidth enhancement factor based on a high frequency modulation and an heterodyne experiment is discussed. Chapter 7 will summarize the main results obtained in this work and suggest some future perspectives.

Chapter 2

Theory of intersubband processes

This chapter presents the theoretical basics necessary for the understanding of the experimental work of this thesis dedicated to the study of QC lasers.

2.1 Schrödinger equation: electronic states

The QC laser structure is a multiquantum well heterostructure composed in our case by lattice matched InGaAs/InAlAs material grown by MBE technique. The wavefunction of an electron in a quantum well can be described by the envelope function formalism as [75, 76]

$$\psi(\vec{r}) = \sum_{n} \zeta_n(\vec{r}) u_{n,\vec{k}}(\vec{r}) \tag{2.1.1}$$

where $\zeta_n(\vec{r})$ is the envelope function and $u_{n,\vec{k}}$ the part of the Bloch function corresponding to the lattice crystal period. As we are only interested to the conduction band, the total eight band model (with the heavy-hole, light-hole, split-off valence bands and the spin-orbit coupling) is simplified by a two-model band where one effective valence band only is coupled to the conduction band [77].

Assuming the Kane approximation(the in-plane wavevector $\vec{k}_{\parallel} = (k_x, k_y) = 0$)[75] and the potential dependence in z-direction only ($\perp$ to the layers) in a heterostructure, the equation can be spatially decoupled. Including the non-parabolicity [78] in terms of an energy-dependent effective mass $m^*(E,z) = m^*(0)(1+\frac{E-V(z)}{E_G})$, the Schrödinger equation can be written in one dimensional form

$$(-\frac{\hbar}{2}\frac{d}{dz}\frac{1}{m^*(E,z)}\frac{d}{dz} + V(z))\psi(z) = E\psi(z) \tag{2.1.2}$$

where $m^*(0)$ and (E-V(z)) are the effective mass (values of $0.043m_0$ and $0.072m_0$ for InGaAs wells and InAlAs barriers, respectively) and the energy of the eigenstate, respectively, measured from the bottom of the conduction band, and E_G the energy gap of the material (0.79 eV).

Assuming a weak interaction with the valence band, the conduction band wavefunction is a good approximation of the electron wavefunction ($\psi(z) \cong \psi_C(z)$). By applying the continuity at the interfaces of ψ_c and of $\frac{1}{m^*(E,z)}\frac{d\psi_c}{dz}$ [75], the numerical solution of this equation predicts the correct energies with an accuracy of a few meV.

The problem of this assumption is that the computed conduction band wavefunctions are not orthogonal. This implies the solution of the general two-band model to derive the normalization in accordance with the valence band written as[77]

$$\left\langle \psi_{c,i} \left| 1 + \frac{E-V(z)}{E-V(z)+E_G} \right| \psi_{c,j} \right\rangle = 1 \quad . \tag{2.1.3}$$

The dipole matrix element, relative to the optical coupling between states, is thus defined by the following form

$$z_{ij} = \frac{\hbar}{2(E_j - E_i)} \left\langle \psi_{c,i} \left| \frac{d}{dz}\frac{1}{m^*(E_i,z)} + \frac{1}{m^*(E_j,z)}\frac{d}{dz} \right| \psi_{c,j} \right\rangle \quad . \tag{2.1.4}$$

The effect of the applied electric field on the heterostructure is taken into account in the program by dividing the potential in very thin steps and enclosing the whole structure in a large quantum well.

In the mid-infrared range (5-10 μm), for high energy states in the active region, and an assumed thermal population, the states are weakly influenced by the doping. However, if we consider the injector/relaxator states to determine the free-carrier intersubband absorption, then the doping is relevant. To be complete, the Poisson's equation is used self-consistently to take into account the doping of the structures.

2.2 Electron-phonon relaxation

The non radiative intersubband transitions are generated by electron scattering to an optical phonon, an acoustic phonon, an other electron, the interface roughness or an impurity. The main scattering mechanism for a subband separation larger than the optical phonon energy $\hbar\omega_{LO}$ is given by the optical phonon scattering. In this particular case, the scattering rate τ_{if} for bulk optical phonon emission between the subbands i and j, computed using the electron-optical phonon Fröhlich interaction (with $\vec{k}_{\parallel} = 0$), is given by[79, 80, 81]

$$\frac{1}{\tau_{ij}} = \frac{m^* e^2 \omega_{LO}}{2\hbar^2 \varepsilon_p} \int dz \int dz' \psi_i(z)\psi_j(z) e^{-q_{ij}(z-z')} \psi_i(z')\psi_j(z') \tag{2.2.5}$$

where $q_{ij} = \sqrt{\frac{2m^*(E_{ij}-\hbar\omega_{LO})}{\hbar^2}}$ is the momentum exchanged in the transition with $E_{ij} = E_i - E_j$ the transition energy. ε_p is defined via $\varepsilon_p^{-1} = \varepsilon_\infty^{-1} - \varepsilon_s^{-1}$, where ε_∞ and ε_s are the high-frequency and static relative permittivity of the material. The estimated lifetime in InGaAs/InAlAs material for a subband spacing equal to the optical phonon in a 10 nm square well is $\tau \sim 0.25$ ps and is in good agreement with the experiment [**?**].

As we are interested to high temperature operation, the dependence of the scattering rates of an optical phonon with temperature can be approximated by

$$\frac{1}{\tau_{ij}(T)} = (1+n)\frac{1}{\tau_{ij}} \tag{2.2.6}$$

where $n = (e^{\frac{\hbar\omega_{LO}}{kT}} - 1)^{-1}$ is the Bose-Einstein factor. For the phonon absorption scattering rates, a similar treatment can be followed by changing the expression q_{ij} in Eq. 2.2.5 into $q_{ij} = \sqrt{\frac{2m^*(E_{ij}+\hbar\omega_{LO})}{\hbar^2}}$ and the coefficient (1+n) in Eq. 2.2.6 into n.

As a conclusion, the shortest lifetime is obtained if the two subbands are separated by exactly one optical phonon, corresponding to a low momentum exchanged. This property is exploited in QC laser design to allow a fast electron escape from the lower state. As a result, the decreasing of optical phonon lifetime with temperature (similar for bulk material) strongly influences the QC laser performances (as shown in section 2.4.1, the threshold current increases and the slope efficiency decreases).

2.3 Electron-photon interaction

2.3.1 Spontaneous emission, absorption and optical gain

According to Einstein's equations and Fermi's golden rule, the radiative rate for spontaneous photon emission τ_{rad}^{-1} induced by an electromagnetic field is[82]

$$\tau_{spon}^{-1} = \frac{e^2 n_{eff}}{3\pi c^3 \varepsilon_0 \hbar^4} E_{ij}^3 z_{ij}^2 \tag{2.3.7}$$

where $n_{eff} = \sqrt{\varepsilon/\varepsilon_0}$ is the refractive index of the medium and z_{ij} the dipole matrix element. The selection rule leads to the result that only an electromagnetic field oriented in the growth direction can induce an electronic transition (TM polarization).

Assuming a Lorentzian shape (homogeneous broadening), the peak material gain, or absorption, between subbands i and j can be written as[82, 83]:

$$G_p = \frac{4\pi e^2}{\epsilon_0 n_{eff} \lambda} \frac{z_{ij}^2}{2\gamma_{ij} L_p} (n_i - n_j) \tag{2.3.8}$$

where $2\gamma_{ij}$ is the full width at half maximum of the transition in energy units (determined from the luminescence spectrum), L_p the length of a period of the active region, $n_{i,j}$ are the subband electron sheet densities, and λ the emission wavelength. The peak modal gain G_m is defined as $G_m = G_p \Gamma$, where the confinement factor $\Gamma = \Gamma_p N_p$ is the product of the number of periods and the overlap factor. The gain cross section g_c corresponds to the product of Γ with the overall Equ. 2.3.8 without the differential population term.

Following this expression, we see that a population inversion has to be engineered in order to obtain gain between subbands. The condition for a laser oscillation in an optical resonator is realized when the gain overcomes the total losses ($G_m = \alpha_{tot}$). In a semiconductor laser, the losses originate from two sources; the mirrors that ensure an optical feedback and the waveguide. The mirror losses $\alpha_m = -\frac{1}{L}\ln R$ are characterized by the facet reflectivity R and the length L of the resonator and can be reduced by facet coatings or the device length. The waveguide losses α_w originate from free-carrier absorption, which can be calculated using the Drude model (with scattering time $\tau = 0.2 - 0.5ps$[84]), and the intersubband absorption at the laser wavelength. To minimize the optical losses, the doping region around the waveguide and the injector, where most of the electron density of each period resides, have to be carefully designed.

2.3.2 Linewidth enhancement factor α

The linewidth enhancement factor, also known as Henry's α-factor is:

$$\alpha = \frac{\partial\chi_r/\partial n}{\partial\chi_i/\partial n} \tag{2.3.9}$$

where $\chi = \chi_r + i\chi_i$ is the susceptibility and n the carrier density in the active region. According to a fundamental theorem of the theory of complex variables, the real and imaginary part of a complex function are related by the Kramers-Kronig transformation. The relation of the susceptibility χ with the complex refractive index n_{comp}, $\varepsilon_0 n_{comp}^2 = 1 + \chi$, make the link with the other parameters used in this chapter.

This α parameter accounts for the effect of carrier density fluctuations n on the optical electromagnetic field. In particular, C. H. Henry has shown that the spectral broadening exceeds the Schwalow-Townes linewidth by a factor of $1+\alpha^2$ [85]. The increase in laser noise represented by α is due to the fact that the random modulation of the carrier density by spontaneous emission must also modulate the index of refraction and thus the frequency of the interband semiconductor medium.

It is thus no surprise that a deliberate modulation of the carriers by a radio frequency current should have a similar effect. In particular, under a direct sinusoidal current modulation (AM), a frequency modulation (FM) proportional to α is added to the expected emitting AM spectrum. This FM, called frequency chirping, is considered undesirable for long-distance and high-bit-rate optical communications systems. In contrast, this effect can be exploited to perform a direct measurement of α by a deliberate current modulation of the lasers (Chapter 6). For interband semiconductor lasers, α values are commonly between 1 - 8 [86].

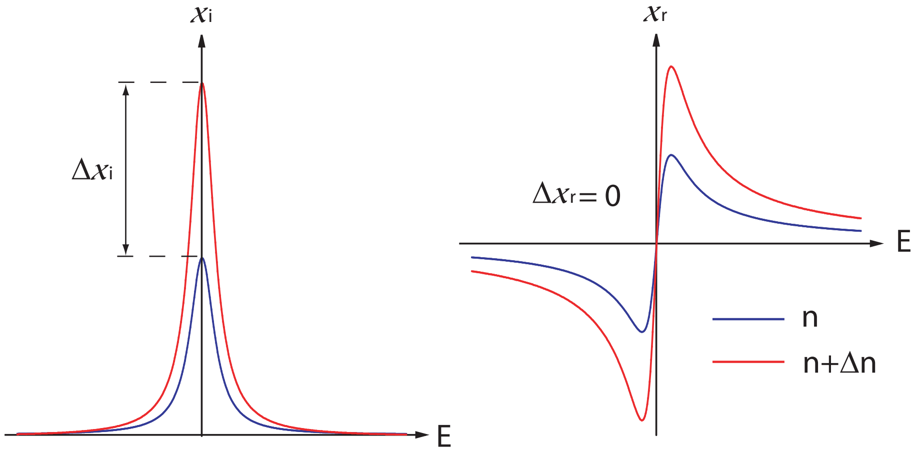

Figure 2.1: Dispersion of the electronic subbands in k-space a)imaginary part χ_i and b) Real part χ_r of the susceptibility variation that occurs for a carrier density variation in intersubband transition

In contrast, α should be zero for intersubband lasers as they show a narrow and symmetric lasing gain spectrum similar as gas lasers. This can be confirmed by using the Kramers-Kronig transformation of the gain curves to obtain the refractive index change as shown in Fig. 2.1. We see that the expected refractive index change χ_r will be zero at the gain peak. As a result, the expected linewidth enhancement factor is zero in a QC laser structure designed to lase at the gain peak curves. Consequently, QC lasers should have a negligible chirp, and thus their optical output should have a negligible FM with a modulating drive current.

2.4 Carrier transport

2.4.1 Rate equations: threshold current

The transport across the active region can be described by the rate equations of a three level system as illustrated in Fig. 2.2. The sheet densities and respective estimated nonradiative rates of the lower and upper lasing states are n_2, $\tau_2^{-1} = \tau_{21}^{-1} + \tau_{2i}^{-1}$ and n_3, $\tau_3^{-1} = \tau_{32}^{-1} + \tau_{31}^{-1}$, respectively. For a photon density S per unit length per period, the rate equations read [**?**]

$$\frac{dn_3}{dt} = \frac{J}{e} - \frac{n_3}{\tau_3} - Sg_c(n_3 - n_2) \tag{2.4.10}$$

$$\frac{dn_2}{dt} = \frac{n_3}{\tau_{32}} + Sg_c(n_3 - n_2) - \frac{n_2 - n_2^{therm}}{\tau_2} \tag{2.4.11}$$

$$\frac{dS}{dt} = \frac{c}{n_{eff}}[(g_c(n_3 - n_2) - \alpha_{tot}]S - \beta\frac{n_3}{\tau_{spon}}) \tag{2.4.12}$$

where n_2^{therm} is the thermal population of the lower lasing state. The contribution of spontaneous emission to the photon density is neglected since only a very small fraction (β=0.001) of the spontaneously emitted power enters to the lasing mode. By setting the left side of the equations equal to zero, and attributing a zero value of S, we obtain a relation between the upper state population $n_3 = J\tau_3/e$, the electrical pumping, and the population inversion $n_3 - n_2 = \frac{J\tau_3}{e}(1 - \frac{\tau_2}{\tau_{32}}) - n_2^{therm}$ from the two first equations, respectively. This latter relation shows that lasing can occur only for $\tau_{32} > \tau_2$. This means that electrons must be supplied at a rate greater than their rate of loss due to intersubband relaxation.

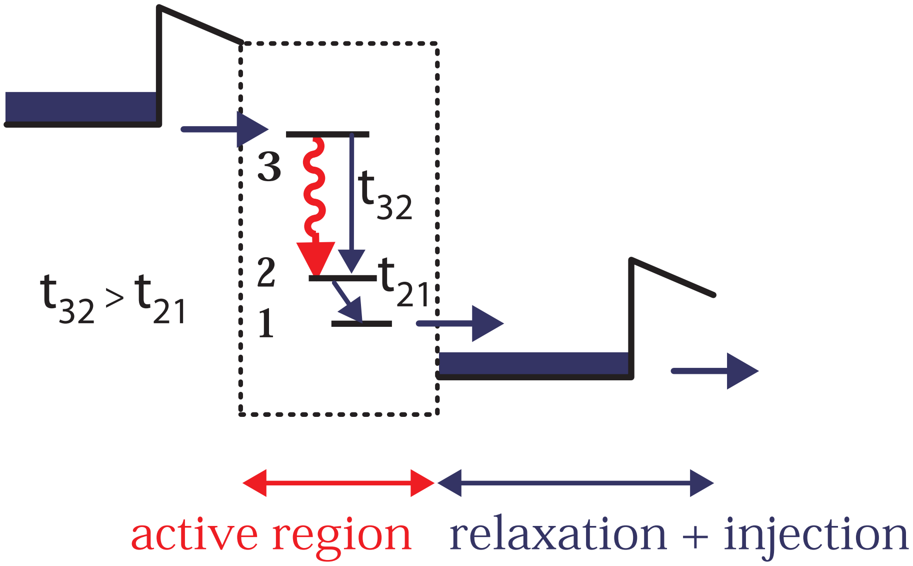

Figure 2.2: three level system in the active region followed by the relaxation/injection region.

The threshold current density derived from the equation of population inversion with the condition $(n_3 - n_2)g_c = \alpha_{tot}$ can be written as follows

$$J_{th} = e\frac{1}{\tau_3}\frac{(\alpha_{tot}/g_c + n_2^{therm})}{1 - \tau_2/\tau_{32}} \tag{2.4.13}$$

The slope efficiency per facet can also be deduced by a similar treatment and is given by

$$\frac{dP}{dI} = \frac{1}{2}N_p h\nu\alpha_m\frac{dS}{dJ} = \frac{1}{2}N_p\frac{h\nu}{q}\frac{\alpha_m}{\alpha_m + \alpha_w}\frac{dS}{dJ} \tag{2.4.14}$$

where $h\nu$ is the laser photon energy. Although the individual carrier numbers can increase above threshold, their difference stays constant.

2.4.2 Photon-assisted tunnelling transition: maximum operating current

The resonant tunnelling transport of electrons between the injector g and the upper lasing state 3 was first derived by Kasarinov and Suris [8, 7, 87], and is described by (from density matrix formalism)

$$J = qN_s \frac{2|\Omega|^2 \tau_\perp}{1 + \Delta^2 \tau_\perp^2 + 4|\Omega|^2 \tau_3 \tau_\perp} \tag{2.4.15}$$

$$\hbar\Delta = E_g - E_3 = ed(F - F_r), d = |z_{gg} - z_{33}| \tag{2.4.16}$$

where $2\hbar|\Omega|$ is the energy splitting at resonance between the ground state of the injector (level g) and the upper lasing state, $\hbar\Delta$ is the energy detuning from resonance, d is the spatial separation between the centroids of the two electron probability distributions, F is the average electric field applied over a distance d, and F_r is the electric field which brings the upper lasing state and ground state of the injector in resonance. The time constant $\tau_\perp$ is the relaxation time for the momentum in the plane of the layers. The sheet density N_s is the electron density in the energy injector level g. The maximum attainable current is obtained at resonance if $\Delta = 0$.

2.5 Direct intensity modulation

2.5.1 Rate equations: frequency response

Based on the short lifetime involved in intersubband transitions, a QC laser possesses unique high-frequency characteristics. In particular, a theoretical direct intensity modulation in the terahertz bandwidth regime without relaxation oscillation frequency has been suggested using the second-order system model [88, 89, 90]. These properties are promising for high-speed free-space optical telecommunication or time resolved spectroscopy. On the other hand, by modulating a laser, we can measure directly the α factor as outlined in the following section.

An approximate expression using simplified rate equations (Eq. 2.4.12) to examine the direct intensity modulation of QC lasers is derived [89, 90]. The rate equation is simplified with the assumption that the second-level population is negligible (only the upper radiative state is considered with a population n). Thus, as is standard for small signal approach, the current term $J = J_0 + J_1 \exp(i\Omega t)$ splits into steady-state and dynamic terms varying at the modulation angular frequency Ω. The current modulation defines as well the small-signal deviation n_1 and S_1 to the carrier population and the photon density steady-states by $n = n_0 + n_1 \exp(i\Omega t)$ and $S = S_0 + S_1 \exp(i\Omega t)$. Inserting the following expression in Eq. 2.4.12 leads to

$$i\Omega n_1 = \frac{J_1}{e} - S g_c n_1 - (\frac{1}{\tau_3} + \frac{1}{\tau_{stim}})n_1 \tag{2.5.17}$$

$$i\Omega S_1 = \frac{1}{\tau_{stim}\tau_{phot}\alpha_{tot}} n_1 \tag{2.5.18}$$

where $\tau_{stim}^{-1} = g_c S_0$ is the stimulated lifetime and $\tau_{phot}^{-1} = \frac{c}{n_{eff}}\alpha_{tot}$ the photon lifetime. Solving these coupled equations for $\eta = \frac{S_1}{J_1}(\Omega)$ leads to

$$\eta(\Omega) = \frac{-\frac{1}{e}\frac{1}{\tau_{stim}}\frac{1}{\tau_{phot}}\frac{1}{\alpha_{tot}}}{\Omega^2 - i\Omega(\frac{1}{\tau_{32}} + \frac{1}{\tau_{stim}}) - \frac{1}{\tau_{phot}}\frac{1}{\tau_{stim}}} \tag{2.5.19}$$

As a result, the QC laser modulation response is that of a second-order system. This expression is quite general. In fact, it looks like the response of interband lasers provided that the lower laser state has a negligible population [**?**]. However, the important quantitative difference concerns the value of the carrier lifetime. To convince ourselves, let us write the two poles of the laser modulation response in the following complex frequencies form

$$\Omega_{\pm} = \frac{i}{2}(\frac{1}{\tau_{34}} + \frac{1}{\tau_{stim}}) \pm \sqrt{\frac{1}{\tau_{stim}}\frac{1}{\tau_{phot}} - \frac{1}{4}(\frac{1}{\tau_{34}} + \frac{1}{\tau_{stim}})^2} \tag{2.5.20}$$

For interband lasers, the poles are purely real because the photon lifetime dominates ($\tau_{phot} \simeq 1ps$), with an upper lasing lifetime estimated to $\tau_{phot} \simeq 4$ ns). As a result, relaxation oscillation frequency appears in the modulus square of the frequency response (Eq. 2.5.19) as reported in Fig. 2.3. In contrast, due to their ultrashort carrier lifetime (τ_{34} is around the picosecond), QC lasers have typically purely imaginary poles. Experimentally, a laser with a low constant driving current was used and a stimulated time of $\tau_{stim} \simeq 1$ ps was calculated. Compared to interband device, the frequency response shows a comparable maximum modulation frequency without oscillations. However, as the stimulated time τ_{stim} can be reduced by the increase of the power, it should be possible to have lower stimulated lifetime and thus laser modulation at frequencies around 1 THz. In this configuration, we show that our simple model predict modulation frequency up to 10 times higher than the one of diode lasers as illustrated in Fig. 2.3.

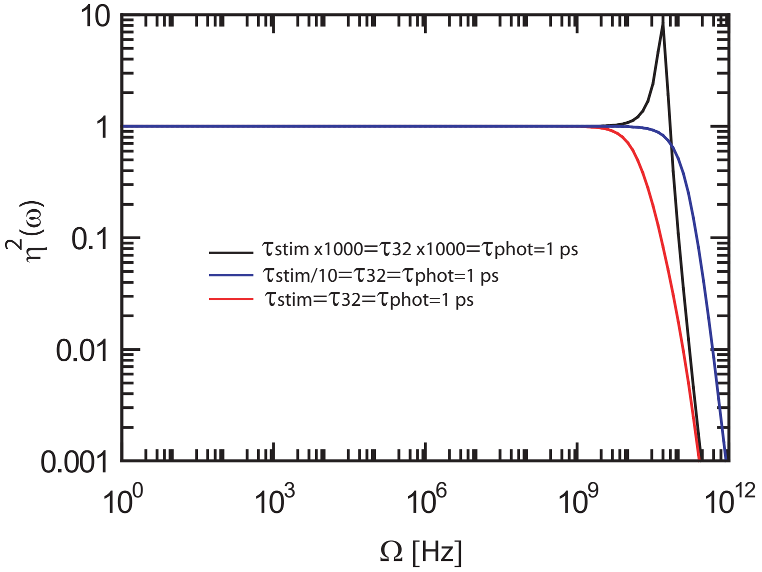

Figure 2.3: Frequency response of the QC laser by small-signal analysis. In the limit of very long scattering time τ_{32} (1 ps), the typical resonant frequency response of a conventional diode laser is achieved. Due to their ultrashort carrier lifetime τ_{34} ($\sim$ 1 ns), no frequency oscillation appears in the response of QC lasers. Based on the simple model, maximum operation up to 1 THz is expected.

2.5.2 FM added to AM

In diode lasers, the direct current intensity modulation (AM) introduces three main frequency modulation (FM) sources in the optically measured intensity spectrum: the temperature and carrier-density effects which are changed with the injection current (dependent on the modulation frequency), and the carrier-density variation associated to the linewidth enhancement factor α (see sect. 2.3.2). If the FM induced by temperature observed in interband lasers below about 100 MHz [91] is also expected in QC lasers (details in sect. 2.5.4), the spatial carrier-density variation in terms of free carrier plasma and anomalous band-edge absorption dispersion effects are neglected for the latter. Based on one type of carrier only and intersubband transitions, the number of free carriers is assumed to remain almost constant and band-to-band effects are ignored. Consequently, for frequencies higher than 100 MHz, only the last FM source is expected for QC lasers and is detailed in the next section.

In Fig. 2.4 are summarized the amount FM modulation induced by an AM modulation. These effects are discussed in the case of intersubband transitions in following sections. They are derived from the rate equations, a simple thermal model and the calculation of the field in the laser cavity. Only the thermal effect for low modulation is expected, otherwise an optical AM modulation is predicted for QC lasers.

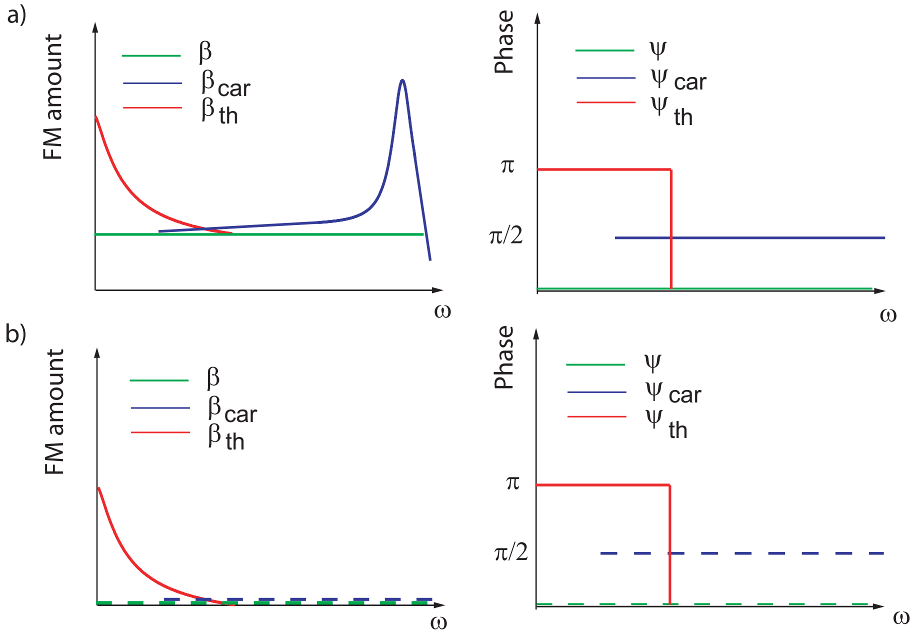

Figure 2.4: The FM amount of modulation induced by an AM as well as the associated phase are described for a) an intersubband and b) an interband laser. In green are the characteristics associated to β=-$\frac{1}{2}\alpha$m (where α is the linewidth enhancement factor), in blue is the carrier dependence (carrier plasma or band edge absorption), and in red is the thermal behavior (heating due to the current for low modulation frequencies))

2.5.3 Electromagnetic field equation: α added FM to AM response

Derived by C. Harder and coworkers [92], the steady-state sinusoidally modulated solution of the field in a cavity mode is

$$E_m(t) = E_1[1 + \frac{m}{2}\cos(\Omega t)]\cos[\omega_1 t + \beta\cos(\Omega t + \psi)] \tag{2.5.21}$$

where E_1 and ω_1 are the amplitude and the frequency of the field, respectively, and ψ is the phase. The parameter β = -$\frac{1}{2}\alpha m$ is the phase modulation index and is proportional to the linewidth enhancement factor α and to the intensity modulation index m. Due to the coupling of gain and refractive index through the Kramers-Kronig relation, an FM proportional to the linewidth enhancement factor and thus to the phase modulation β appears in the field equation. This expression suggests a simple way to obtain the exact direct value of α by measuring the relative sideband strength in the frequency spectrum. A phase ψ=0 is calculated for diode lasers as well as for QC lasers.

2.5.4 Simple thermal model: thermal FM

In fact, the change of the refractive index with temperature is used in DFB QCL's to tune devices. It is thus quite clear that FM modulation originates from thermal effects due to the device heating by the current modulation. A simple thermal model is proposed to understand this behavior. The thermal equation is simplified by assuming that only the active region is heated by the modulated current and is given by

$$CV\frac{\partial(\triangle T)}{\partial t} = \frac{1}{R_{\mathrm{th}}}\triangle T + P \tag{2.5.22}$$

where $\triangle T = T_{\mathrm{act}} - T_{\mathrm{sink}}$ is the difference between the active region temperature T_{act} and the heatsink temperature T_{sink}. The absorbed heat has a value of CV, where C is the heat capacity per unit volume for active material and V is the active region volume. The dissipated power is characterized by a thermal resistance R_{th}. The heat generation power is P=$U_{\mathrm{dc}}I_{\mathrm{dc}}$+$\Delta P\exp(\Omega t)$. The amplitude of the time-dependent part of the electrical power dissipated in the device is assumed to be $\Delta P = \frac{m}{2}I_{\mathrm{mod}}(U_{\mathrm{dc}} + \frac{dU}{dI}I_{\mathrm{dc}})$, where U_{dc} and I_{dc} are the operating voltage and current, respectively, I_{mod} the modulated current, and $\frac{dU}{dI}$ the differential resistance.

Solving the equation by substituting the homogeneous solution of the temperature difference, $\triangle T = T_0(t)\exp(\frac{-t}{CVR_{th}})$, the general solution yields

$$T_{\mathrm{act}} = T_{\mathrm{sink}} + U_{\mathrm{dc}}I_{\mathrm{dc}}R_{\mathrm{th}} + \frac{\frac{m}{2}I_{\mathrm{mod}}(U_{\mathrm{dc}} + \frac{dU}{dI}I_{\mathrm{dc}})}{\Omega CV}\cos\left(\Omega t - \frac{\pi}{2}\right) \tag{2.5.23}$$

The calculated phase difference between induced temperature T_{act} and the power source P is π. This phase difference is attributed to the time delay between the temperature response and the current modulation and is similar to the measured and calculated value for diode lasers[93].

On the other hand, the optical frequency deviation is given by the derivative of the frequency modulation form in Eq. 2.5.21 and can be written as $\triangle\nu = \frac{1}{2\pi}\Omega\beta_{therm}$. The parameter β_{therm} is attributed to the parasitic frequency variation induced by thermal effects added to the carrier-density variation represented by the parameter $\beta = -\frac{1}{2}\alpha m$. For small modulation frequencies, this term is related to the temperature induced modulation frequency $\triangle\nu = \frac{\partial\nu}{\partial T}(T_{\text{act}} - T_{\text{sink}})$, where $\frac{1}{\nu}\frac{\partial\nu}{\partial T}$ is the fractional change of the refractive index. The solving of the to last expressions yields

$$\beta_{therm} = \pi\frac{mI_{\text{mod}}(U_{dc} + \frac{dU}{dI}I_{dc})}{\Omega^2 CV}\frac{\partial\nu}{\partial T} \tag{2.5.24}$$

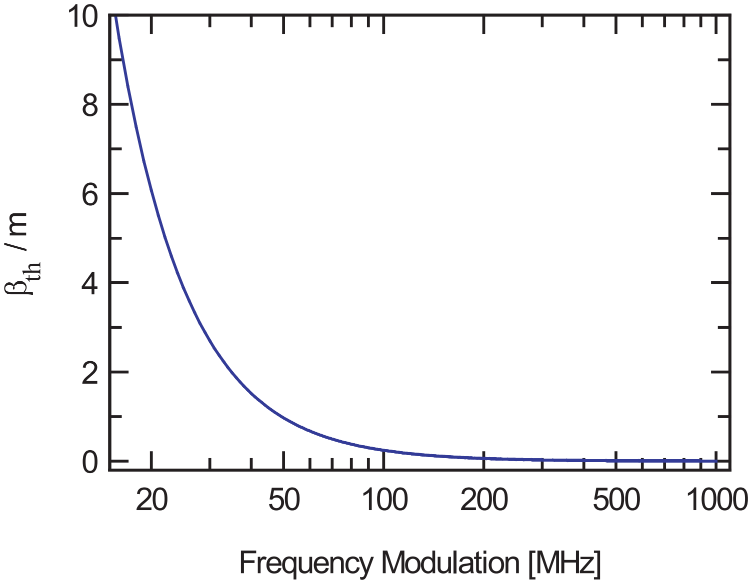

Figure 2.5: Thermal chirping due to the modulation current heating

This expression is used to simulate the experimental data in Fig. 6.6. The used values for our experiment, with the distributed feedback laser described in section 4.4, are I_{mod}=72 mA, $U_{\text{dc}} = 8.9$ V, $I_{\text{dc}} = 0.316$ A, $\frac{dU}{dI} = 5$ Ohm, $C = 1.7$ JK^{-1}cm^{-3} [94], $V = 6.3{\cdot}10^{-8}$ cm^3,

$\frac{1}{\nu}\frac{\partial \nu}{\partial T} = -6.8 \cdot 10^{-5}$ K^{-1}. The result of this calculation is reported in Fig. 2.5. The thermal effect due to the modulation is observed up to 100 MHz.

Chapter 3

Two-phonon resonance QC lasers emitting around 9.1 μm

The optimization of the quantum design focused initially on obtaining devices operating at room temperature with low threshold currents. A particular success was the two phonon resonance active region design which avoids both electron extraction bottleneck and thermal backfilling. The objective of this part of the work was to obtain low threshold current density QC lasers by studying the influence of interface roughness and doping concentration on InAlAs-InGaAs/InP laser performances. As a consequence, the pulsed threshold current density at 300 K dropped to a value of 3 kAcm^{-2}.

3.1 Two-phonon resonance design

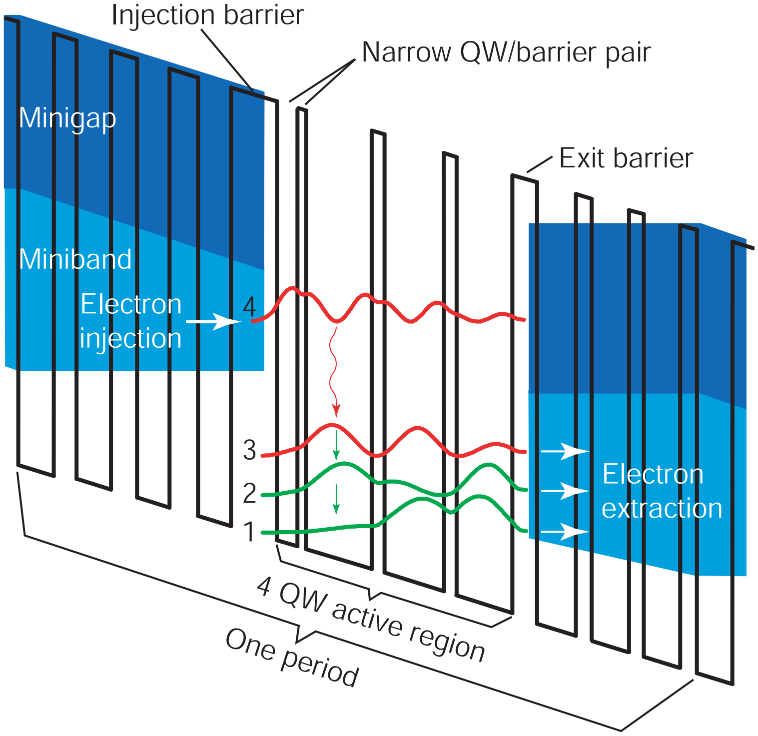

Figure 3.1: Schematic conduction band diagram of one stage of a QCL design for 9.1 μm emission. The moduli squared of the relevant wave function are shown. The layer thicknesses (in angstroms and starting from the injection barrier) are as follows: **40**/19/**7**/58/**9**/57/**9**/50/**22**/34/**14**/33/**13**/32/**15**/31/**19**/30/**23**/29/**25**/29/ where $In_{0.52}Al_{0.48}As$ barrier layers are in bold, $In_{0.53}Ga_{0.47}As$ well layers are in roman, doped layer are underlined. The Si sheet density is $2.5 \cdot 10^{17}$ cm^{-3}.

To reduce the room-temperature threshold current density, active region designs based on a double-phonon resonance and bound-to-continuum transition were developed. In these structures, the injection and extraction efficiency to and from the active region were significantly improved by means of wave function engineering. We present here a QC laser with an active region based on a double-phonon resonance[25] and designed for a lasing transition at an energy of 135 meV (corresponding to 9.1 μm).

The typical schematic conduction band diagram of one period of the active region (S1850) is displayed in Fig. 3.1. Assuming a radiative lifetime based on the emission and absorption of bulk optical phonons, a computed value of $\tau_4 = 0.48$ ps is obtained. A double-phonon resonance between the coupled three lower lasing energy states (levels 1,2 and 3) on the lower radiative state 3 leads to a short electron lifetime τ_3=$[\tau_{32}^{-1} + \tau_{31}^{-1}]^{-1}$=0.18 ps and an efficient extraction. The reduction of the so-called electron extraction bottleneck using the double-photon resonance design was demonstrated with a model that included optical phonon emission and extraction into all points in k-space[26]. This design takes also advantage of the 3QW active region with a thin first injector well that guarantees a high injection efficiency and prevents an important overlap of the wave functions of the injector ground state g with the lower lasing states.

3.2 Growth

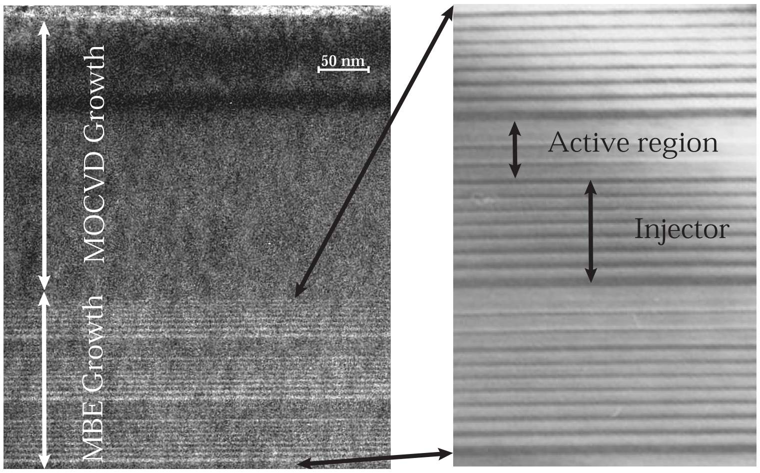

Figure 3.2: a) TEM image of a of the cleaved cross section of a quantum cascade laser active region (sample S1850) composed by a part of an active region (grown by MBE) and an upper cladding layer (grown by MOCVD). b) Enlargement of 3 periods of the active region

The two techniques used in this study for thin film deposition are molecular beam epitaxy (MBE) for the core of the device, and metalorganic vapor phase epitaxy (MOVPE) to complete the growth with waveguide layers. MBE growth of the samples was carried out by Dr. Ursula Oesterle and Dr. Mattias Beck at EPFL Lausanne in the group of Prof. Marc Ilegems, and by Dr. Marcella Giovannini, Dr. Mattias Beck and Mr. Nicolas Hoyler at the University of Neuchâtel in the group of Prof. Jérôme Faist. The growth by MOCVD was performed in the FIRST lab at ETH Zurich by Emilio Gini in the group of Prof. Hans Melchior and Prof. Heinz Jaeckel.

The devices were grown on an n-doped InP (Si, 2×10^{17} cm^{-3}) substrate used as a bottom cladding layer. After the lower waveguide layer (InGaAs, Si, 6×10^{16} cm^{-3}, with 0.2μm), the core of the waveguide consisting of 35 periods of the active region was grown. The active region is composed of sequences of lattice matched $\mathrm{In_{0.53}Ga_{0.47}As/In_{0.52}Al_{0.48}As}$ layers. The part of the structure grown by MBE was then completed with an upper waveguide layer (InGaAs, Si, 6×10^{16} cm^{-3}, 0.3μm thicknesses). The overgrowth by metalorganic vapor phase epitaxy (MOVPE) consists of a top cladding layer (InP, Si, 1×10^{17} cm^{-3}, 2.5μm thickness), a top contact layer (InP, Si, 7×10^{18} cm^{-3}, 0.85μm thickness) and a cap layer (InGaAs, Si, $2 - 3 \times 10^{19}$ cm^{-3}, 10 nm thickness). Thanks to Dr. Massoud Dadras, a transmission emission microscope (TEM) image of the structure can be shown in Fig. 3.2.

3.3 Luminescence spectra

Low temperature luminescence spectra (device S1840, same structure but different doping $4. \cdot 10^{17}$ cm^{-3}) are represented in Fig. 3.3. The emission wavelength of 138 meV is in good agreement with the design wavelength of the radiative transition energy. The large dipole matrix element z_{43}=3.0 nm of the radiative transition confirms that the transition corresponds to a vertical transition. The dipole matrix element between levels 4-2 decreases strongly with applied field while the transition from levels 4 and 1 is always very small (z_{42}=1 nm, z_{41} <1 nm). The electroluminescence spectra correspond to a strong injection regime and transitions from level 5 are experimentally observed. As expected, the transitions 4→2,

g→3 and g→2 are strongly reduced with increased applied bias. In general, the luminescence peaks confirm the strength and the location of the intersubband transitions. The full width at half maximum (FWHM) of the radiative transition at low temperature is 12 meV.
Using a Lorentzian line shape with the single particle approximation[95], an in plane dephasing lifetime of $\tau_{\perp}$=0.07 ps is calculated. The dominant broadening mechanism of the electroluminescence peak is attributed to interface roughness scattering[95, 96, 97].

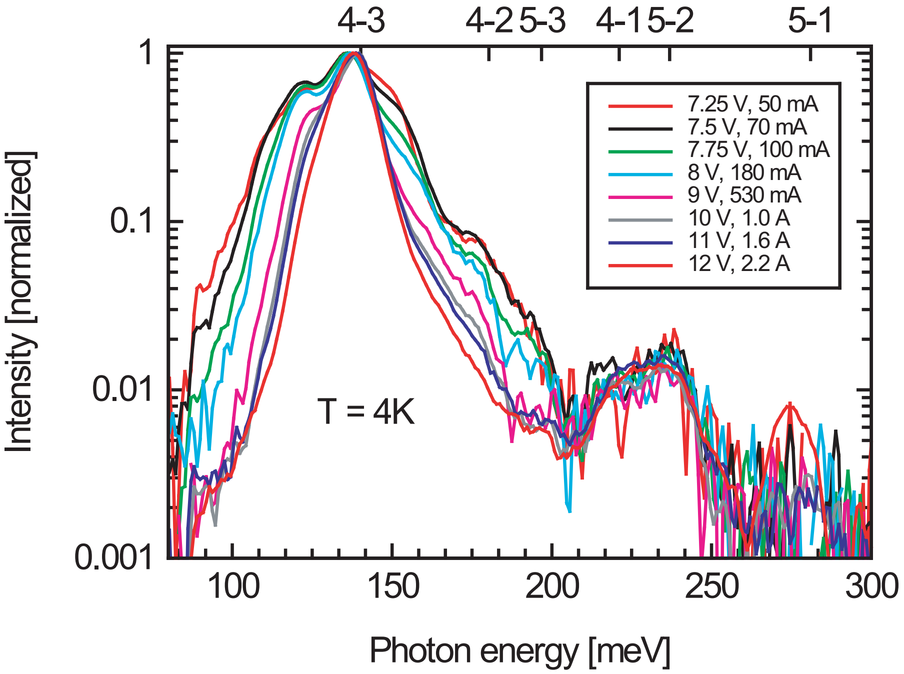

Figure 3.3: Electroluminescence spectra with different applied voltage.

3.4 Design optimization

3.4.1 Alloy disorder and interface roughness

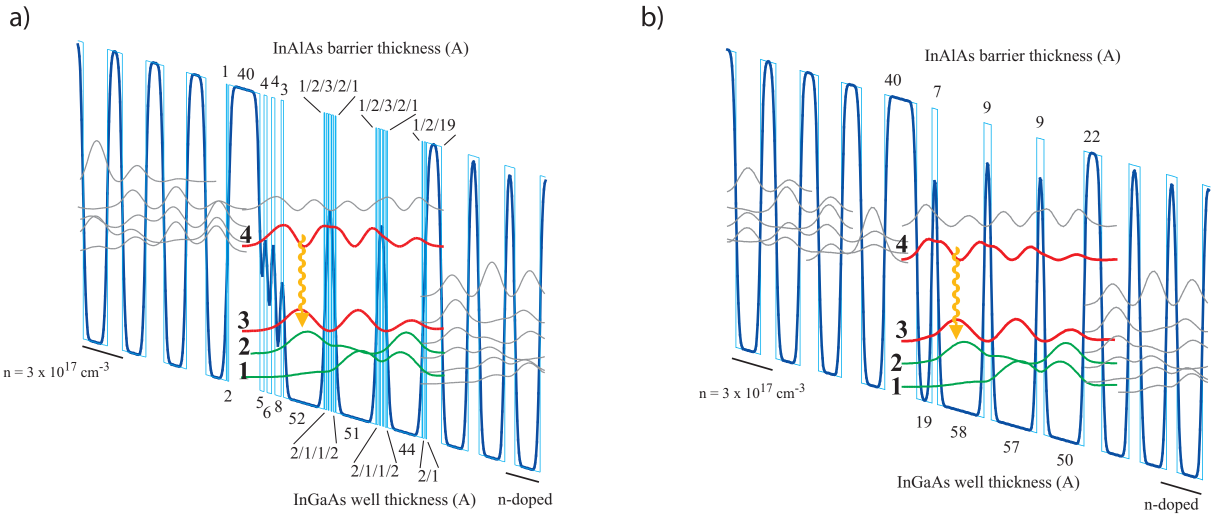

Figure 3.4: Schematic conduction band diagram of one stage of (a) graded and (b) abrupt interface designs. The layer thicknesses of the wells and the barriers of the active region are reported on the band diagram. The Si sheet density is $3.2 \cdot 10^{11}$ cm^{-2}. The potential calculated by taking into account of an interface diffusion length of 0.3 nm is plotted in bold.

In order to study the interfaces of heterostructures, QCL's based on digitally graded interfaces are compared to a structure with an identical 4 quantum well active region but abrupt interfaces. Except for the interfaces, both types of devices are identical and based on a double phonon resonance for wavelength emission at 9.1 μm. The term "digitally graded" means that each sharp interface in the 4 wells of the active region between an InGaAs well and an InAlAs barrier and its neighboring ±0.3 nm was replaced by a 0.1 nm InAlAs - 0.2 nm InGaAs - 0.2 nm InAlAs - 0.1 nm InGaAs interface. The schematic conduction band diagram of one period of both active regions is displayed in Fig. 3.4(a) and 3.4(b) (corresponding to samples S1868 and S1840, respectively). Cross sectional scanning-tunneling microscopy (X-STM) measurements have been performed on the graded and the abrupt interface structures in collaboration with P. Offermans and P. M. Koenraad[98]. A detailed image of the active region of both structures is reported in Fig. 3.5(a) and (b), respectively. The brighter and darker regions within and across the layers indicate the strong presence of alloy fluctuations. These variations are causing strong interface roughness and strongly decrease the effect of the intentional grading of interfaces. The thin barrier in the active region, indicated by arrows, looks the same. In contrast, the injector barriers are clearly different. This is confirmed with the Fig. 3.5(c) where the averaged line profiles of the active region are shown. Taking into account a diffusion model with a Lorentzian broadening at interfaces with an assumed diffusion length of 0.3 nm, a new potential can be defined. The conduction band profiles of the graded and abrupt interfaces calculated with the diffusion model are plotted in Fig. 3.4 (a) and 3.4(b), respectively. The model reproduces the strong difference of injector barriers as observed experimentally.

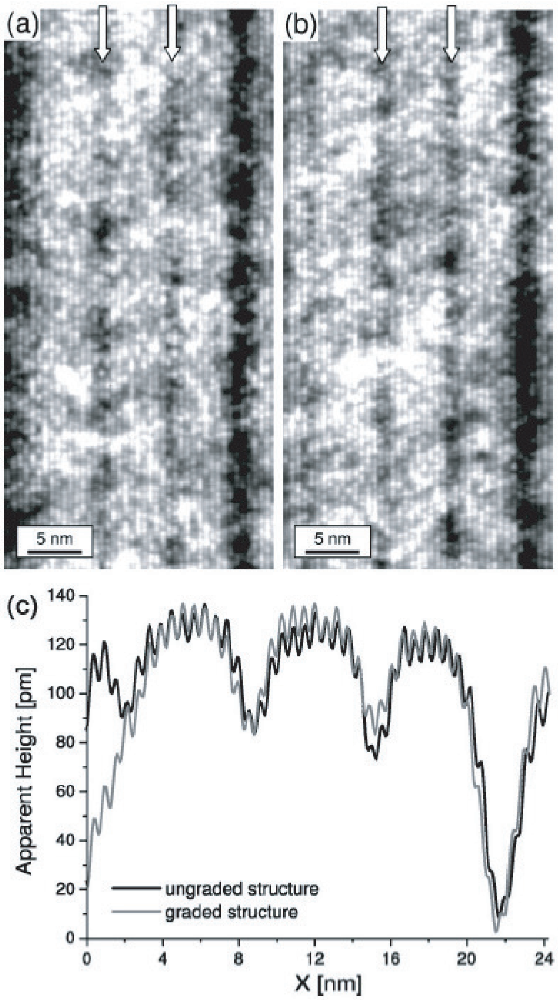

Figure 3.5: STM image of the active region of (a) the structure with graded interfaces and (b) the structure with abrupt interfaces. (c) shows the averaged line profiles of the active region. With courtesy of P.Offermans and P. M. Koenraad.

In order to quantify the sharpness of the interfaces, the distribution of the gallium and aluminium atoms across both interfaces of a 2.5 nm wide barrier is derived by using averaged line profiles of the filled states images. Since the filled states of the sample surface are imaged, the aluminum and gallium atoms themselves are not directly probed but rather the electronic effects these two atomic species have on the surface arsenic atoms. The aluminium distribution is determined by fitting with a concentration profile in the form of c(x)=1/2erf[(L/2+x)/2σ_x]+erf[(L/2-x)/2σ_y], where L is the width of the barrier and σ_x and σ_y indicates the sharpness of the interfaces of the barrier. Figures 3.6 show for both QCL structures the aluminium distribution of a 2.5 nm wide InAlAs barrier with ungraded interface. The analysis was done for profiles taken at different sample voltages and as expected the counted aluminium distribution is independent of the bias. The FWHM of the distribution for both structures is in agreement with the growth menu and in both cases the interfaces have a gradient of 4 ML. This grading is caused by the large scale alloy fluctuations attributed to indium segregation during growth. This means that any additional digital grading of the interfaces of the active region will not have much effect on interface roughness. On the other hand, the grading of the injector barrier changes the injector thickness[99] and the well thickness[95] and prevents to identify the effect of interface roughness on device performance.

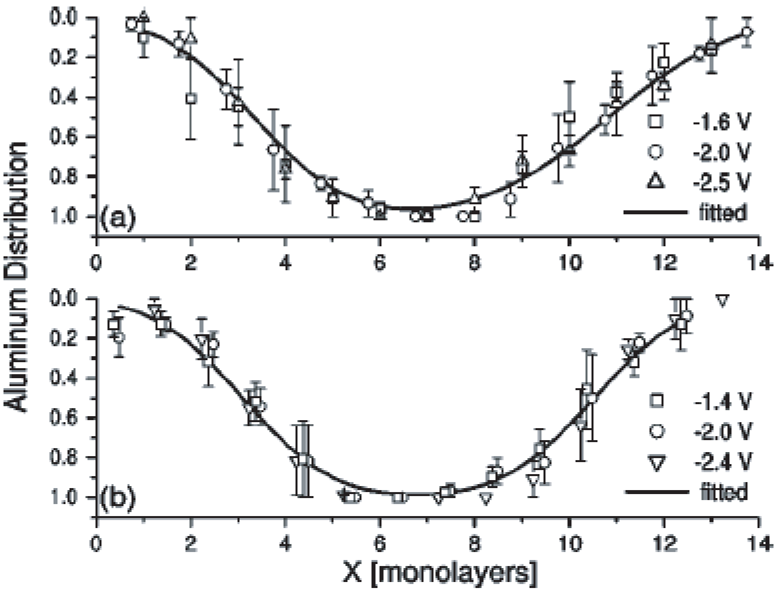

Figure 3.6: Aluminium concentration of a 2.5 nm barrier of the structure with (a) graded and (b) abrupt interfaces. The aluminium concentration was derived from averaged line profiles taken at three sample voltages. With courtesy of P.Offermans and P. M. Koenraad.

Two graded interface designs (see 3.4.1) with injection barriers of 4 and 3 nm, corresponding to samples S1868 and N42, respectively, were compared to confirm the influence of injection barrier thickness on performance for this kind of device[99]. Fig. 3.7(a) shows the normalized luminescence spectra at cryogenic temperatures for both devices. The FWHM of the luminescence peak decreases with the enhancement of the injection barrier thickness, due to the smaller energy splitting at resonance $2\hbar|\Omega|$, and increases the gain (Equ. 2.3.8). On the other hand, the narrowing of the injection barrier improves the injection efficiency[100] between the injector state g and upper lasing state 4. In principle, this measure also increases an undesired coupling of the state g with the lower lasing state 3, but fortunately, this transition was appearantly not affected by the injection barrier thicknesses used here. This was confirmed by similar oscillator strengths derived from the corresponding luminescence spectra. To confirm similar growth conditions of the two different MBE machines (S1840 from Lausanne and N41 from Neuchâtel), similar luminescence spectra of two abrupt interface samples grown just before the injector thickness study are displayed in Fig. 3.7(b). As expected, they exhibit literally identical luminescence spectra. Moreover, as shown in 3.4.3, the dependence of luminescence spectra to the different doping concentrations for the radiative transition is negligible.

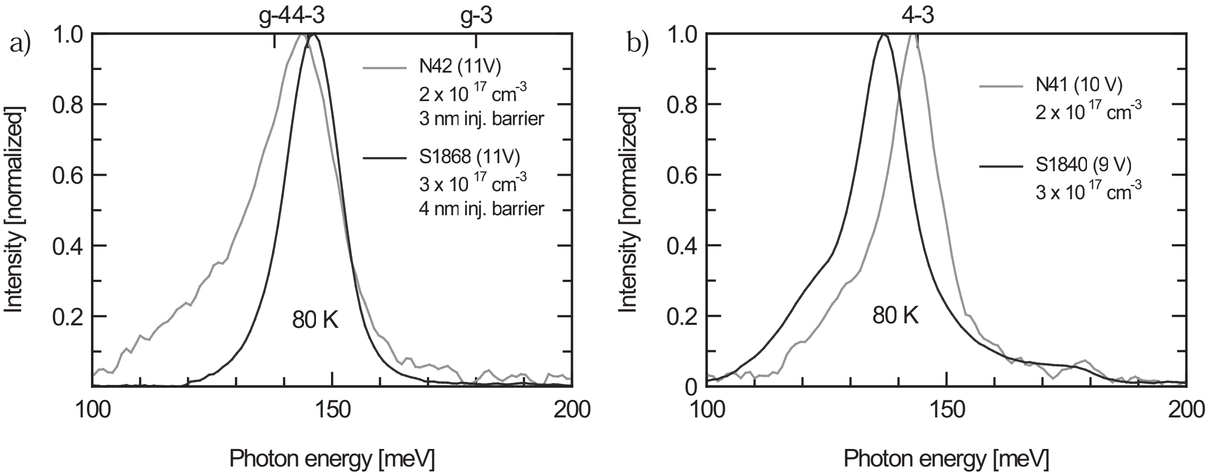

Figure 3.7: Luminescence spectra of (a) graded and (b) abrupt interface devices.

3.4.2 Doping concentration

As seen in the previous section, it is difficult to systematically change growth parameters such as interface roughness or background doping. Therefore, we studied the lasing properties as a function of doping density. For four different sheet densities n_s, one wafer per doping level was grown: Si, 2.6×10^{11}, 2.1×10^{11}, 1.5×10^{11} and 1.0×10^{11} cm^{-2} (corresponding to the runs n67, n72, n69, and n71, respectively, with the same design illustrated in Fig. 3.1). A controlled experiment is guaranteed by a sequence of layers grown consecutively under nominally identical growth conditions. A similar study based on GaAs/AlGaAs lasers emitting in the mid-infrared region was presented in reference [101]. It demonstrated the influence of free-carrier absorption on both the optical losses and the threshold current density[102]. The effect of the doping concentration on the conduction band profile and the resonant alignment was also investigated[103].

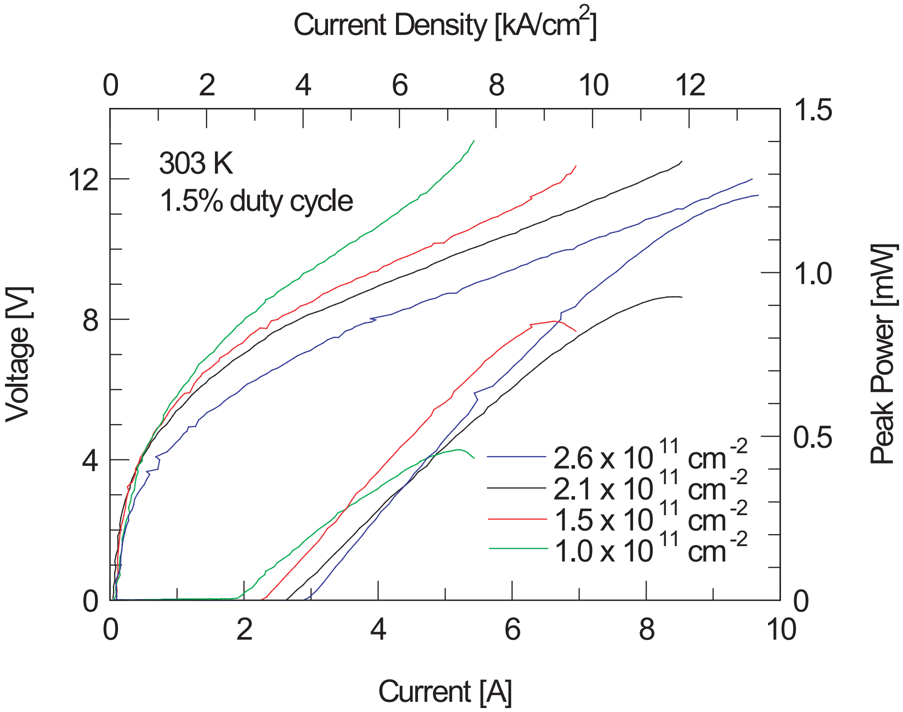

Figure 3.8: Current-voltage and current-optical peak power characteristics of 3 mm-long and 24 μm-wide lasers in pulsed mode at room temperature for four different doping concentrations.

Average output power measured by a calibrated thermopile detector and voltage characteristics as a function of current of four differently doped QCL's are presented in Fig. 3.8. The lasers were operated at a temperature of 303 K using 100 ns long pulses with a repetition frequency of 100 kHz (Alpes Lasers TPG 128 pulse generator). Three lasers per wafer were tested; their current densities agree within 10 % of each other. This small fluctuation is attributed to variations of the laser ridge width across the processed samples. As expected, the measured threshold current densities increase linearly with the doping concentration. The samples with the smallest doping concentration (1.0×10^{11} cm^{-2}) show a threshold of 2.6 kA/cm^2 whereas the one with the highest doping density (2.6×10^{11} cm^{-2}) have a value of 4.0 kA/cm^2 . Similarly, the maximum operating current increases linearly with the doping concentration from a value of 7.2 kA/cm^2 (P_{max} = 460 mW) to a maximum value of 13.5

kA/cm^2 (P$_{max}$ = 1.2 W). The doping concentration therefore determines the laser's dynamic range in terms of current. The best laser performance results from a trade-off between high output power and small current consumption necessary for continuous wave operation.

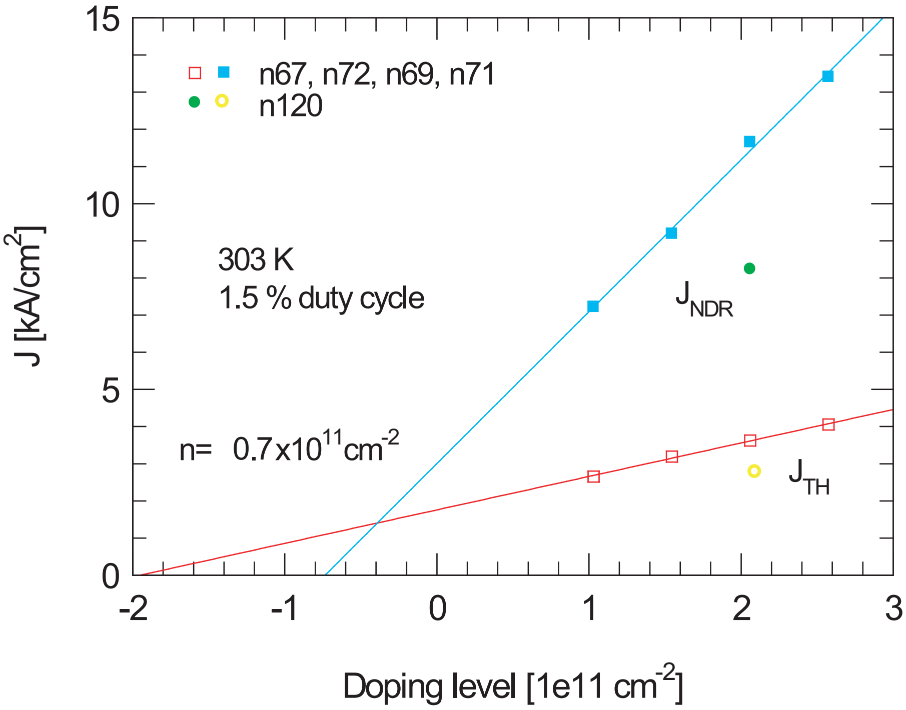

Figure 3.9: The threshold current density J_{TH} is shown as open squares and the maximum current density J_{NDR} as solid squares as a function of sheet densities corresponding to the doping study (n67, n72, n69, n71). In solid lines, fitted curves corresponding to an extrapolated doping offset of $n_{offset} = 0.7 \times 10^{11}$ cm^{-2} added to the active region doping are shown. Open and solid circles represent the threshold and the maximum current densities respectively of a laser grown after a longer MBE running time (n120).

The linear dependence of the maximum current density J_{NDR}, which corresponds to the negative differential resistance (NDR) for all doping concentrations, is shown in Fig. 3.9 (solid squares). The resonant tunnelling of electrons between the injector g and the upper lasing state 4 was first derived by Kasarinov and Suris [8, 7, 87], and can be described by

Equ. 2.4.15. The maximum attainable current is obtained at resonance if $\Delta = 0$. According to this expression, the linear variation of the maximum current with the doping concentration suggests that the electron-electron scattering contribution to the upper state lifetime τ_4 is negligible. Similarly, the measured intersubband luminescence as a function of doping density (see Fig. 3.12) shows no dependence of linewidth with the carrier concentration. This suggests a constant in-plane dephasing lifetime $\tau_\perp = 0.07$ ps (According to the 17 meV of the FWHM of the luminescence spectra). The sheet density N_s in Equ. 2.4.15 is the electron density in the injector ground state g. This electron density can be approximated by $N_s = n_s$ - N_{trans}, where n_s corresponds to the total sheet density in the injector region and N_{trans} to the density of electrons which participate to the transport in the active region. The transport carrier density can then be written as $N_{trans} = J\tau_{trans}/q$, where τ is the time of the electron transit in a period of the active region of length L_p (59.8 nm). First, this electron transport time was estimated to a value of $\tau_{trans} = 1.4$ ps [104] by considering only the transport by phonon after the first intersubband scattering event (by multiplying the optical phonon emission time τ_{ph} (0.2 ps) with the number of optical phonon energy steps of N=$\frac{F \cdot L_p}{\hbar\omega_{LO}} - 1 = 7$, where $\hbar\omega_{LO} = 34$ meV is the optical phonon energy). However, the total transport time in the active region has to be considered, by adding the injection time of 1.53 ps, as reported and calculated by Faist [105].

By fitting the experimental maximum currents in Fig. 3.9 with a corrected value of 3.3 meV for the energy splitting $\hbar|\Omega|$, we obtained a value of τ_{trans}=4.3 ps. The close calculated value is in agreement with the experiment. The experimental data (solid squares) are shifted relative to the theoretical curve which has a zero value for the maximum current ($J_{NDR} = 0$) for an undoped structure ($n_s = 0$). Consequently, an extrapolated n-type sheet carrier density of $n_{offset} = 0.7 \times 10^{11}$ cm^{-2} seems added to the active region doping. This additional sheet density corresponds to a volume density of $N_V = 0.8 \times 10^{17}$ cm^{-3} and can be attributed to an impurity background level in the MBE system.

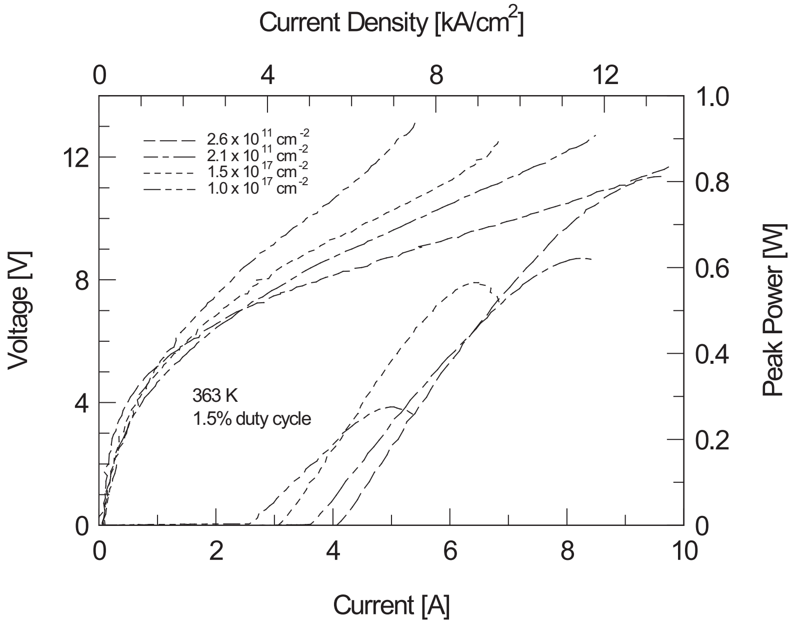

Figure 3.10: Peak power vs current of 3mm-long and 24 μm-wide lasers operated at 363 K with 1.5 % duty cycle for four different doping concentration.

The dependence of the threshold current density J_{TH} on the doping concentration (open squares) is also linear as shown in Fig. 3.9. This dependence is not temperature dependent as shown at 363 K in Fig. 3.10 with values of the threshold current density between 3.6 and 5.7 kAcm^{-2} (for $1.0 \cdot 10^{11}$ and $2.6 \cdot 10^{11}$cm^{-2}, respectively). The optical peak power still reaches 275 ($1.0 \cdot 10^{11}$cm^{-2}) and 813 mW ($2.6 \cdot 10^{11}$cm^{-2}) at this high temperature. Assuming an exponential variation of the threshold current density with temperature ($J_{TH} \sim \exp(T/T_0)$), we extrapolate characteristic temperatures T$_0$ of 178, 175, 195 and 188 K (for 2.6×10^{11}, 2.1×10^{11}, 1.5×10^{11} and 1.0×10^{11} cm^{-2} respectively), as shown in Fig. 3.11. These values are uncorrelated to the doping concentration implying negligible electron backfilling of the lower lasing state. Furthermore, the characteristic temperatures T$_0$ agree with the model which includes the temperature-dependent lifetimes (τ(T)) due to thermal activation of optical phonons. The model used for describing the variation of the threshold current density with doping density is based on a rate equation approach[90] and corresponds to Equ. 2.4.13.

In this expression, the total optical losses $\alpha = \alpha_m + \alpha_w$ are the sum of the mirror losses α_m (4.3 cm^{-1}) and the waveguide losses α_w. The waveguide losses $\alpha_w = \alpha_w^{undoped} + \Gamma\alpha_w^{abs}$ contain the losses of the undoped waveguide structure $\alpha_w^{undoped}$ and the calculated free carrier absorption losses for the different doping concentrations α_w^{abs} (35, 29, 23 and 15 cm^{-1} for 2.6×10^{11}, 2.1×10^{11}, 1.5×10^{11} and 1.0×10^{11} cm^{-2}, respectively). The slope of the doping concentration dependence of the threshold current density reported in Fig. 3.9 leads to close experimental values of intersubband absorption of 42, 33, 25 and 17 cm^{-1}. The number used in this computation are the emission wavelength λ=9.1 μm, the modal refractive index n=3.4, the full width at half maximum of the transition in energy units determined from the luminescence spectrum $2\gamma_{ij}$=17 meV, the dipole matrix element z_{43}=3.0 nm, and the overlap factor Γ=65%. The time constant τ_{43}=2.54 ps represents the lifetime of the transition 4→3 derived from the optical-phonon emission processes and τ_3=0.20 ps is the lifetime of the electron in the lower state of the radiative transition. These values lead to a gain value of g_c= 4.2 10^{-11}. The thermal population in the lower lasing state n_3^{therm} can be neglected in our case. Even when subtracting the doping offset $n_{offset} = 0.73 \times 10^{11}$ cm^{-2} attributed to the background doping of the MBE, the deduced value for the waveguide $\alpha_w^{undoped}$ and mirror losses α_m is 12 cm^{-1} ($n_s = 0$). This large value is attributed to the high absorption of the Si_3N_4 insulating film between the laser ridge and the top ohmic contact.

However, The slope efficiency of current-optical power characteristics (see Fig. 3.8) increases with the doping density, in contrast to the expected trend due to the increase of the waveguide losses α_w. The same effect was observed when measuring shorter devices (1.5 mm long): the slope efficiency would decrease, in opposition to the expected trend. We attribute this behavior to a sublinear dependence of the gain on the current density.

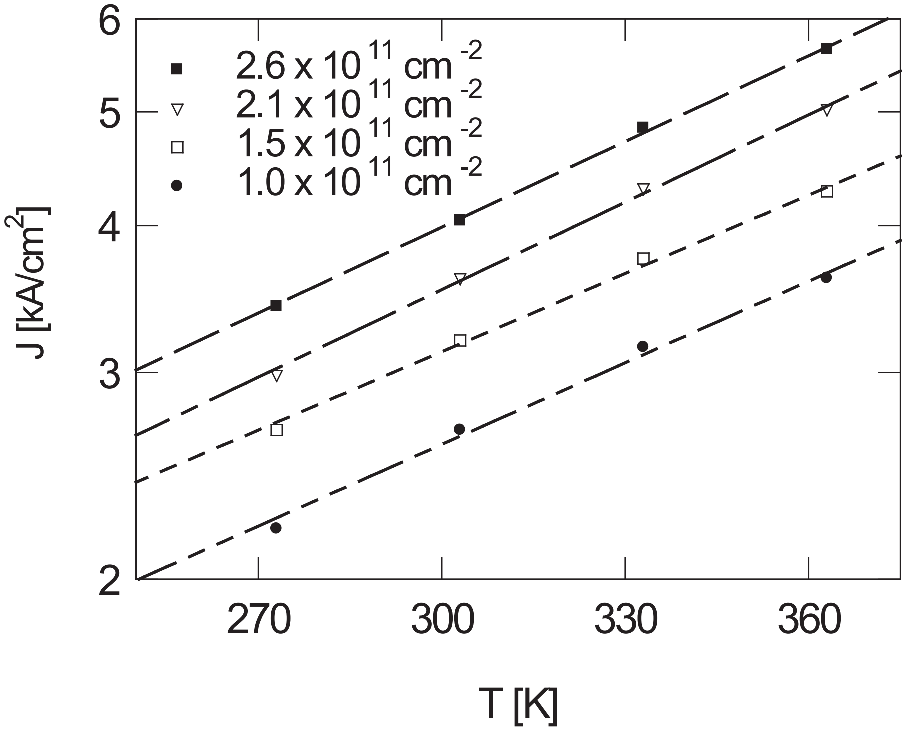

Figure 3.11: Temperature dependence of threshold current density for different doping densities. Characteristic temperatures T_0 of 178, 175, 195 and 188 K (for 2.6×10^{11}, 2.1×10^{11}, 1.5×10^{11} and 1.0×10^{11} cm^{-2} respectively) are extrapolated.

Electroluminescence spectra measurements for three different doping densities were performed and are displayed in Fig. 3.12 (2.6×10^{11}, 1.5×10^{11} and 1.0×10^{11} cm^{-2}). Measurements were made by a Fourier transform infrared spectrometer (Nicolet 860), a mercury cadmium telluride detector and a power supply (HP 8114a). The curves are shifted in energy by the ratio between the nominal and the measured active region thickness as measured by X-ray diffraction. No correlation between the luminescence wavelength and the doping concentration is observed in contrast to GaAs/AlGaAs materials[101]. Furthermore, the full width at half maximum of the radiative transition is insensitive to the doping variation (16.8, 17.6, 16.6, 16.8 meV at 300 K starting from the lower doping concentration). These results are consistent with a negligible contribution from electron-electron scattering to the transition broadening. The electroluminescence spectra correspond to a strong injection regime and therefore transitions from level 5 are experimentally observed. The only noticeable variation with doping concentration is a small increase in the strength of the 5→2 transition. As this peak arises from hot electron transport, we could expect a slight increase of electron temperature of the active region with reduced doping.

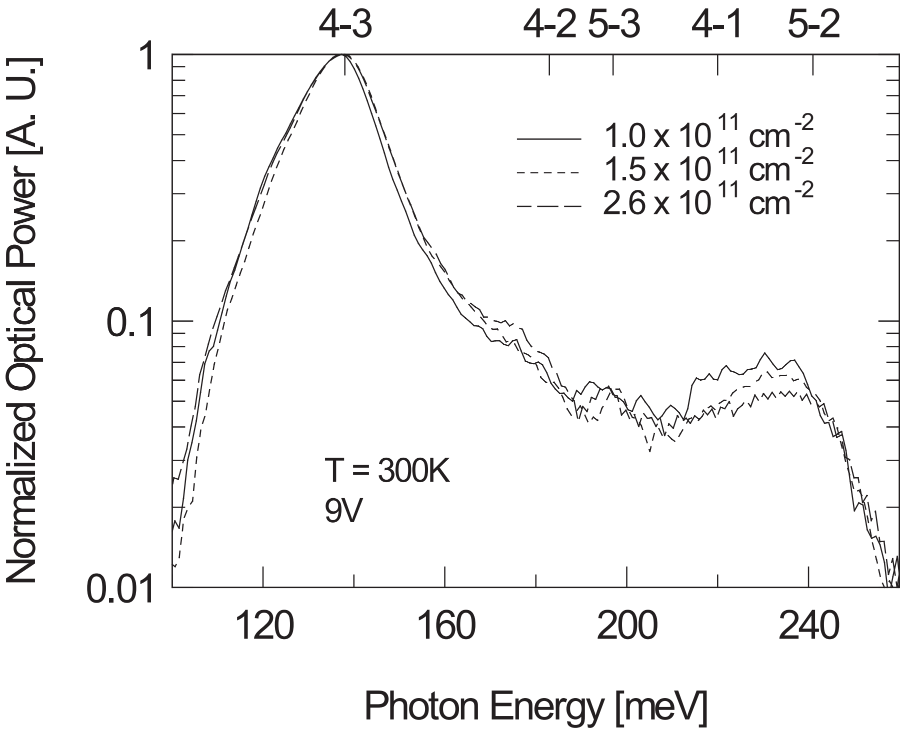

Figure 3.12: Electroluminescence spectra from 180μm × 180μm square mesas under an applied voltage of 9 V at 300 K for different doping concentrations of 2.6×10^{11}, $1.5 \times 10^{11}$and 1.0×10^{11} cm^{-2} (with current densities of 4.6, 3.7 and 3.1 kA/cm^2 respectively). The curves are shifted in energy by the ratio between the nominal and the measured active region thicknesses as measured by X-ray diffraction. Calculated transition energies are shown on the top of the horizontal axis.

3.4.3 Drift of performance due to the growth condition

Usually, the background impurity level tends to decrease with time in an ultra high vacuum environment. In order to check this, a sample identical to n72 was grown after about 2 months of continuous operation of the MBE system. The measured values of J_{NDR} and J_{TH} of this device (n120) are reported in Fig. 3.9 (solid and open circles respectively). As expected, both values are lower and correspond to a situation where no background doping of the MBE appears ($N_V = 0$ cm^{-3}). Considering the device n120 (2.1×10^{11} cm^{-2}) and the sample n71 (1.0×10^{11} cm^{-2}) with its added background doping (0.2×10^{11} cm^{-2} and 1.0×10^{11} cm^{-2} respectively), a comparable total doping concentration is obtained with a similar threshold current density as shown in Fig. 3.9.

These investigations show clearly that optimizations in terms of doping density, thickness of the injection barrier, and abruptness of the interfaces are of crucial importance for the correct functioning of high performance QC lasers. Even more drastically expressed, room temperature CW operation of a QC laser is difficult or even impossible to achieve if these parameters are not carefully adjusted to their optimal values. In the following chapter, we will illustrate that besides, external parameters like junction-down mounting, correct heatsinking, facet coating, and buried, low-loss waveguiding are equally important for the demonstration of a laser to be used in everyday applications.

Chapter 4

Distributed feedback QC lasers

Certain applications quite clearly need single-mode lasers; in particular the narrow linewidths which can achieved. In this context, the addition of a periodic structure in the waveguide leads to a spectral selectivity as described by the coupled-mode theory in the first part of the Chapter. However, like for the diode lasers for telecommunication, this concept was already exploited in 1996 for QC lasers, where distributed feedback (DFB)-QC lasers have been demonstrated at Bell Laboratories by C. Gmachl and coworkers [58]. The fabrication of such devices, with an etched grating in the laser cavity, is outlined in the second part of the Chapter.

Moreover, high resolution spectroscopy based on pulsed QC lasers is typically limited by the fairly wide emission linewidth ($\sim$ 500 MHz) due to thermal chirping (discussed in sec. 2.5.4). Therefore, room temperature CW operated devices with emission linewidths of a few megahertz at 9.1 and 5.4 μm were developed in the last part of the Chapter. As the narrow stripe fabrication is not sufficient for achieving CW operation at a wavelength of 9.1 μm, a buried heterostructure device was realized.

4.1 Mode selectivity and temperature tuning

To understand the behavior of DFB laser structures, the main parameters of the coupled-mode theory developed by H. Kogelnik and C. Shank [106] are outlined. The coupling constant, which defines the amount of feedback via backward Bragg scattering coupled to the forward propagating light, can be written as:

$$\kappa = \frac{\pi}{\lambda_0}\Delta n + \frac{i}{2}\Delta g \tag{4.1.1}$$

where Δn and Δg are the assumed amplitude modulations of the refractive index and the gain, respectively. They are induced by the introduction of a periodic structure in the waveguide. The Bragg reflection condition $\lambda_0 = 2n_{eff}\Lambda$ for a first order grating of periodicity Λ determines the Bragg wavelength λ_0.

The product κL, where L is the structure length, has a strong influence on device performances and a good trade-off between the threshold gain, the sidemode suppression ratio, and the maximum power is usually found if $\kappa \cdot L \approx 1$.

By inserting the coupling constant in the scalar wave equation and solving the resulting pair of coupled differential equations, we obtain the following transcendental equation

$$g_{th} - i \cdot \delta = \pm i \cdot cosh(\gamma \cdot L) = \gamma \cdot coth(\gamma \cdot L) \tag{4.1.2}$$

where α is the absorption index and $\gamma^2 = \kappa^2 - (\alpha - i\delta)^2$ the complex propagation constant. The normalized frequency parameter $\delta = \Delta\beta = \beta - \beta_0 = \frac{n_{eff}}{c}(\omega - \omega_0)$ measures the detuning of the frequency ω from the the Bragg frequency ω_0.

There is no general analytical solution of this equation. For special cases, however, numerical solutions can be computed. Although index modulations imply also a certain amount of gain modulation, our particular devices can usually be approximated by pure index coupling where the single-mode yield can approach values of 50 %. In the particular case of an index-coupled DFB laser, no resonance at the Bragg frequency ω_0 can be observed and two modes on each side of the stop-band are theoretically possible with identical threshold gain. In practice and due to a slight deviation from the facet phase condition, single-mode operation is possible.

The change of the refractive index with temperature $\frac{1}{n_{eff}}\frac{\partial n_{eff}}{\partial T}$ is used in DFB-QC lasers to tune devices. The measured fractional change of the refractive index in QC devices is of the order of $\frac{1}{\nu}\frac{\partial \nu}{\partial T} = -7.0 \cdot 10^{-5}\mathrm{K}^{-1}$. The temperature tuning is associated to the material and is assumed to be a constant parameter. Therefore, the operating wavelength increases with temperature because the refractive index becomes larger.

4.2 Fabrication

Many of the steps for constructing a typical DFB laser are similar to those for constructing a good Fabry-Pérot laser, except for the addition of a grating etched into the epitaxial layers just above the gain region. The first realization was based on a surface grating and has been reported in 1997 by Faist et al. [58]. It was a loss-coupled DFB in which the grating was etched on the top of the device and covered with metal. A picture of a DFB QC laser fabricated with a surface grating but without metal on the top is reported in Fig. 4.1. Although DFB lasers with surface gratings are, among other amenities, quite simple to fabricate, they suffer from their own specific drawbacks. The most important one is the fragile top contact which tends to overheat, and which does not help very much in distributing the heat.

Therefore, for high temperature CW operation, we defined a grating in the cavity as it was first developed by Gmachl et al. [107]. This can be achieved by growing, in a first step, only the active region and the waveguiding layers. The grating, holographically defined, is then etched to a depth of 180 nm into the top InGaAs waveguide layer with a H_3PO_4:H_2O_2:H_2O (2:4:6) solution. In a second epitaxial growth, the InP top cladding is grown, ideally in an MOVPE system. The second InP growth is performed after a thorough cleaning of the surface in concentrated sulfuric acid. Moreover, the top cladding should consist of the same material as the lower cladding layer, thereby protecting the grating.

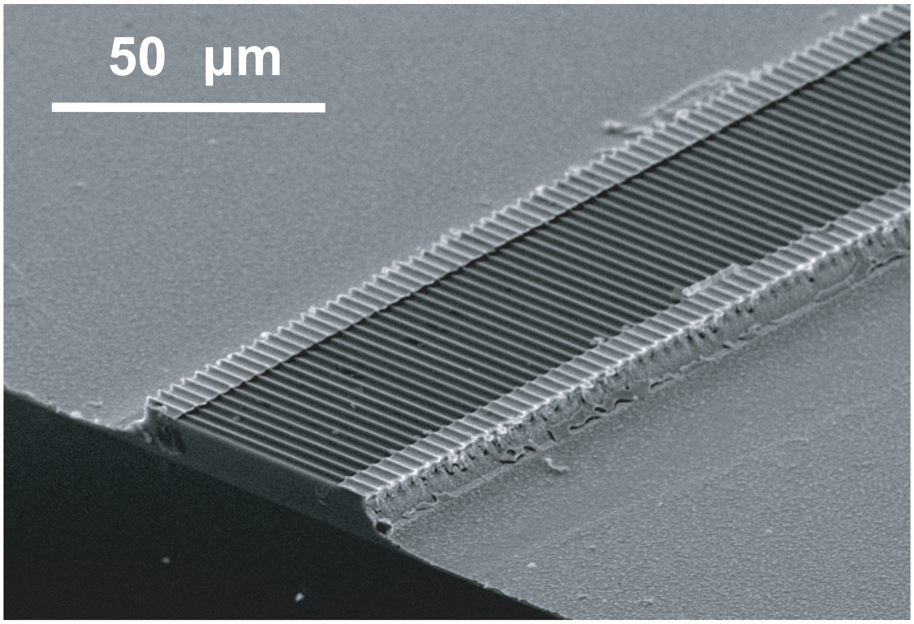

Figure 4.1: Scanning electron microscope (SEM) picture of a DFB-QC laser fabricated without epitaxial regrowth. With courtesy of D. Hofstetter.

4.3 DFB-QC lasers emitting around 9.2 μm

4.3.1 Narrow stripe performances

The epilayer (n120, structure similar as reported in Fig. 3.1 with 2.1×10^{11} cm^{-2} doping concentration) described in the previous Chapter was processed into 15 μm wide ridge waveguides using standard processing. The ridges were cleaved and soldered junction up on copper submounts. The lasers were mounted on the cold finger of an N_2-flow cryostat. The light from the facet was collected by a f/0.8 optics and the output power was measured with a calibrated thermopile detector. CW operation of a back coated 3 mm long device is shown in Fig. 4.2. The laser emitted 15 mW of optical power and exhibited a threshold current density of 3.5 kA/cm^2 and a slope efficiency dP/dI of 75 mW/A at -40 C. In contrast to devices at lower wavelength (i.e. 5.4 μm), the narrowing of the stripe and back facet coating was not sufficient to obtain CW operation at room temperature due to higher free carrier absorption (the Drude model predicts a dependence as $\alpha_w \sim \lambda^2$). The reduction of the waveguide losses by fabricating buried heterostructures is needed as explained in the next section.

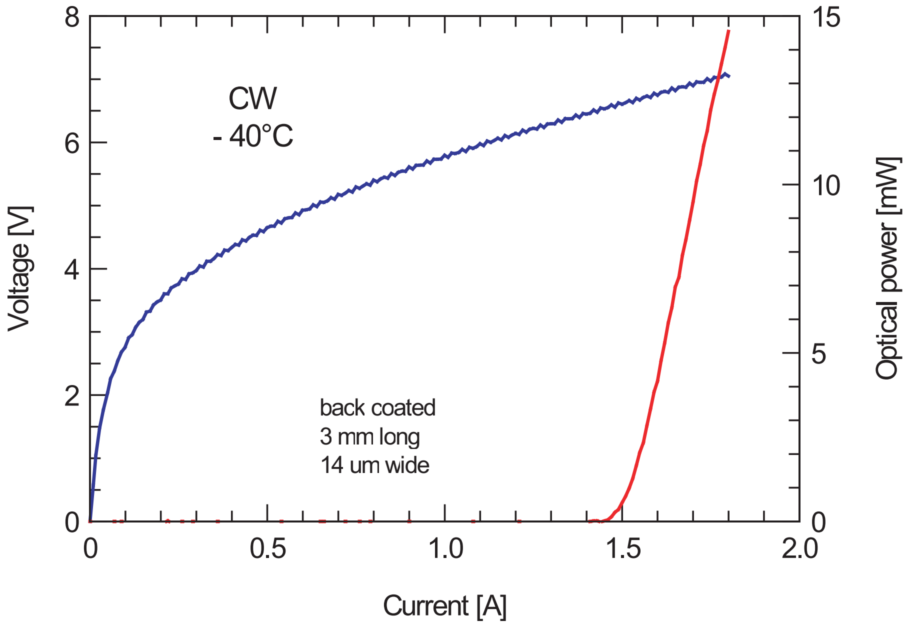

Figure 4.2: L-I and I-V curves of a in CW mode measured at -40 C. The device is back coated and junction-up mounted.

4.3.2 Buried heterostructure fabrication

In standard structures, the side walls of the etched laser ridges (H_3PO_4:H_2O_2:H_2O (1:1:10) solution) were covered by Si_3N_4 or SiO_2 deposited using plasma-enhanced chemical vapor deposition (PECVD), which provided an insulating film between the top ohmic contact of the laser and the n-doped substrate. Lower lateral waveguide losses (smaller Δn_{eff}) and improved lateral heat dissipation can be achieved by substituting the dielectric films by undoped InP. To this end, overgrowth of InP by selective lateral metalorganic chemical vapor deposition (MOCVD) on ridges masked by SiO_2 was performed as illustrated in Fig. 4.3. This approach has the advantage that it yields a planarized structure for junction down mounting and a smaller capacitance in perspective to high frequency modulation. Si_3N_4 was deposited on top of the overgrown InP before contact metallization in order to inject current only on the top of the ridge.

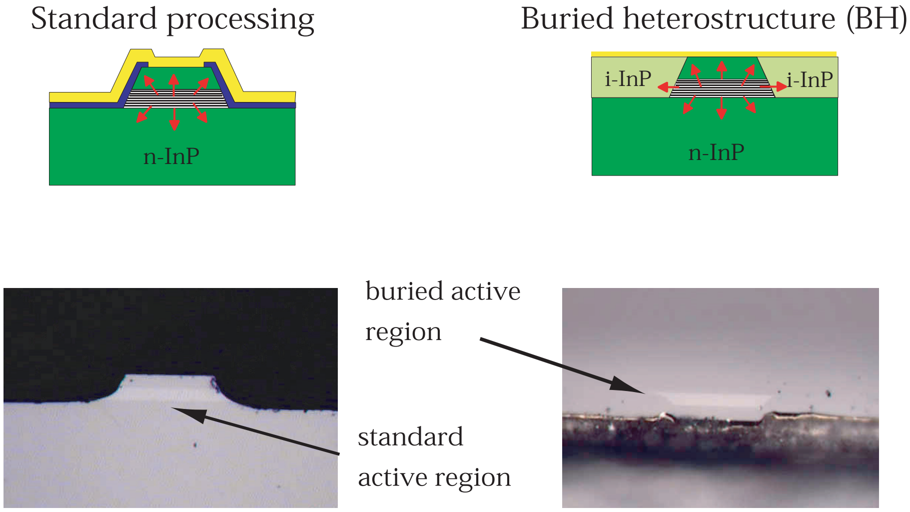

Figure 4.3: Standard processing compared to buried heterostructure configuration

Concerning the heat dissipation, we make the following reasoning[41]: In pulsed mode at low duty cycle, heating effects are negligible. In CW operation, however, the active region temperature T_{act} is much higher than the heat sink temperature T_{sink} due to the high heat dissipation during lasing action; T_{act} can be related to the heat sink temperature by the thermal resistance R_{th}, the voltage U and the threshold current I_{th} via $T_{act} = T_{sink} + U \cdot I_{th} \cdot R_{th}$. This model [108] corresponds to the constant part of the one derived in sec. 2.5.4. Assuming a constant threshold voltage U and the phenomenological relation $\mathrm{J}_{th}= J_0 \exp(T_{act}/T_0)$, the maximum CW operating temperature $T_{sink,max}$ can be expressed as $T_{sink,max}{=}T_0[\ln(T_0 G_{th}/J_0 \mathrm{U})$-1]. Following this model, the temperature dependence of the CW threshold current can then be predicted from the one measured in pulsed mode. As a result, a high value of the characteristic temperature T_0 as well as a good thermal conductance G_{th} are needed for high temperature CW operation.

The choice of a buried stripe greatly improves the heat transport and the thermal conductance G_{th} by allowing heat flow towards all sides from the active region. Additionally, the narrow-stripe geometry also decreases the total amount of strain that builds up in a material subject to a very strong temperature gradient. Indeed, the results from a simulation, done with a commercial finite-elements differential equation solver (PDease2D, [41]), of both thermal transport and thermally induced stress lead to the same conclusions (Fig. 4.4, A) and B). A thermal conductance of 820 W/Kcm^2 is predicted for a buried, 12-μm-wide, junctiondown mounted device, as compared to the calculated value of 510 W/Kcm^2 for a 28-μm-wide, ridge, junction-downmounted device. Similarly, the maximum thermally induced shear stress that builds up at the edges of the active region (Fig. 4.4) decreases from 22 MPa in the ridge device to 3.6 MPa for the buried structure.

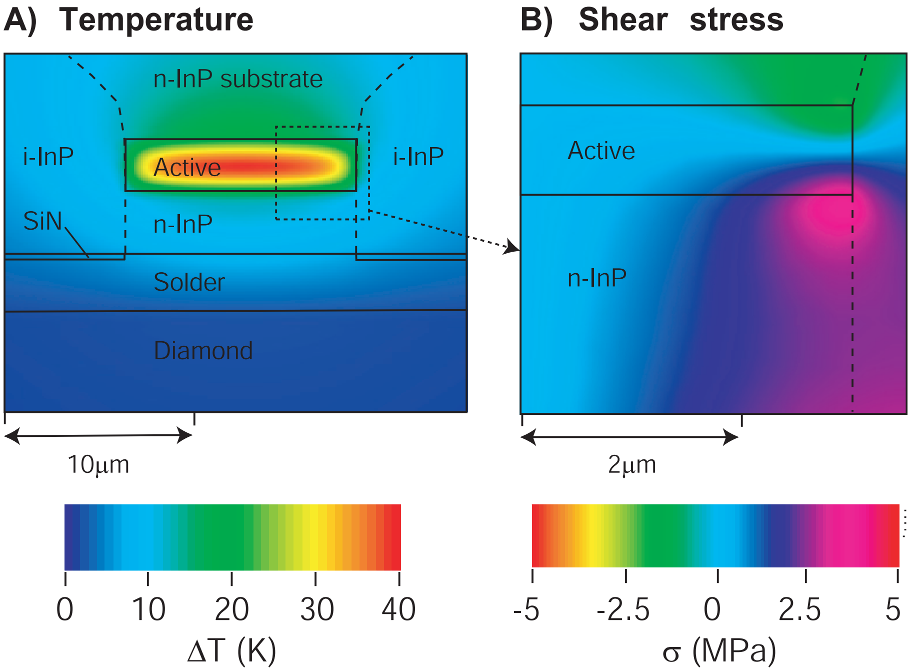

Figure 4.4: (A)Computed temperature contours around the active lasing region of the buried heterostructure QC laser at room temperature. The solid lines display the geometry of the different materials used in the simulation, and the dashed lines represent the geometry of the laser. (B) Computed thermally induced stress in the active region. The maximum stress occurs at the corner of the active region.

Unfortunately, the growth of lateral i-InP material can induce leakage currents. An estimation of the current which flows through the side of the active region in lateral overgrowth geometry is given by the space in short n-i-n structures. As reported by A. A. Grinberg and S. Luryi [109], the current through an n-i-n structure with equal donor concentration N (10^{17} cm^{-3}) in both n layers and an intrinsic (i) base of thickness L_{active} (2 μm) in the approximation of high field regime takes the form

$$\overline{J} = \frac{9}{8}\frac{\overline{V}^2}{\overline{L}^3} \tag{4.3.3}$$

where $\overline{J}$, $\overline{V}$, and $\overline{L}$ are the dimensionless current density, potential, and thickness respectively. The expressions for the potential $\overline{V} = \frac{eV}{kT}$ and the thickness $\overline{L} = L_{active}/\sqrt{\frac{\varepsilon\varepsilon_0 kT}{e^2 N}}$ are converted in MKSA units (by changing the factor $\frac{1}{4\pi} \rightarrow \varepsilon_0$ and the Boltzmann constant k[CGS]→k[MKSA]). Values of 386 and 148 are calculated, respectively, assuming a bias V=10 V and a temperature of T=300 K. The current density is given by $J = \overline{J} N \mu kT/\sqrt{\frac{\varepsilon\varepsilon_0 kT}{e^2 N}}$ and a value of 40 kA/cm^2 is found for a mobility $\mu = 3000$ cm^2/Vs.

As a result, improving the structure by introduction of a buried heterostructure led to an intrinsically high leakage current. The interface between the laser ridge and the overgrowth seems to be a key parameter since we can attribute to it an increase or decrease of the leakage current. This can explain the difficulty to reproduce the first performance of buried heterostructures presented in the next section. Current-voltage characteristics of some of fabricated, but non-lasing buried heterostructures and the laser of the next section are reported in Fig 4.5. The estimated leakage currents in these experimental structures are not as high as the simple model predictions, but they were nevertheless sufficiently large to prevent these structures from lasing. However, this problem was solved by doping the InP lateral overgrowth of the buried heterostructure with Fe$^+$ [55].

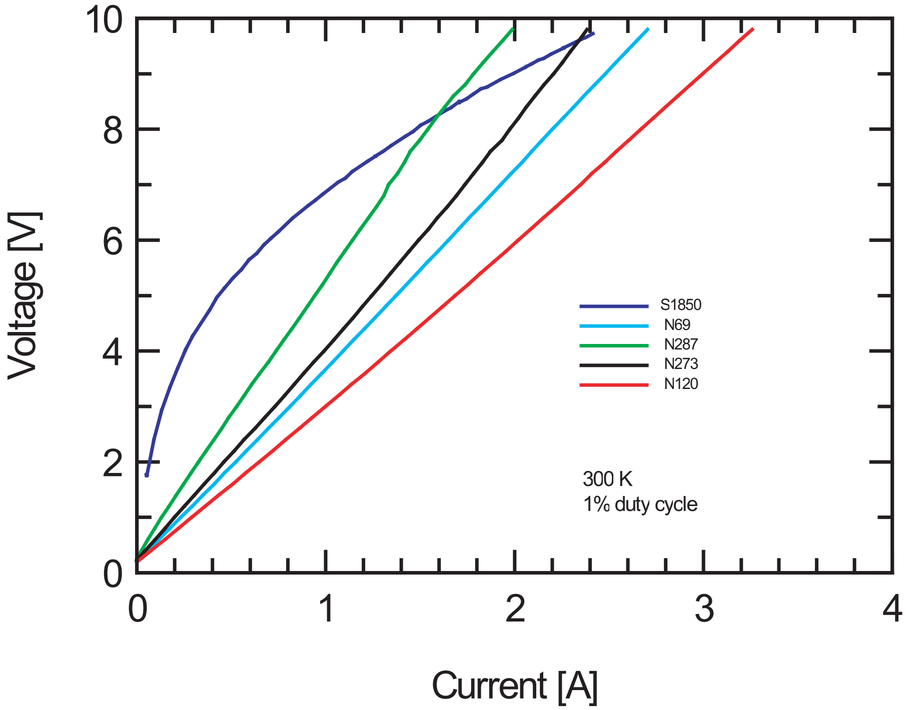

Figure 4.5: Current-voltage characteristic of non lasing buried structures

4.3.3 BH QC laser performances

The first above room temperature CW operated QC lasers (S1850) were based on a double-phonon resonance active region and fabricated as narrow stripe, planarized, buried heterostructure devices. The laser structure is identical to the one described in Fig. 3.2.

To enable a large temperature tuning range, lasers were mounted on the cold finger of an N_2-flow cryostat. As usual, the light from the facet was collected by an f/0.8 optics and the output power was measured with a calibrated thermopile detector. Fig. 4.6 shows voltage bias and CW optical output power collected from one facet of a 1.5 mm-long junction-down mounted DFB laser. The laser emitted 18 mW of optical power, exhibited a threshold current of 400 mA, and a slope efficiency dP/dI of 78 mW/A at $T = 180$ K. The threshold current increased up to 730mA for the maximum operating temperature of $T = 250$ K for continuous wave operation, while the optical power was still 0.6 mW at 790mA.

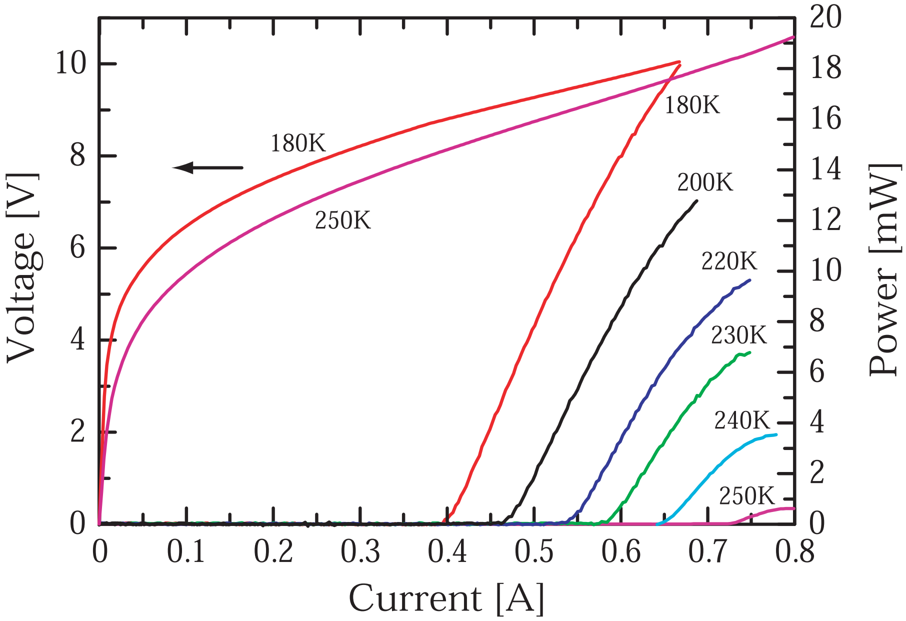

Figure 4.6: Voltage and optical power vs current of a 1.5mm-long uncoated DFB laser operated in CW mode at various heat sink temperatures between 180 K and 250 K.

The emission of the laser can usually be tuned by changing either current or temperature. A series of CW spectra was collected using a high-resolution (0.125 cm^{-1}) Fourier transform infrared spectrometer (FTIR) and a deuterated triglycine sulphate (DTGS) detector. Single-mode emission was observed with a sidemode suppression ratio (SMSR) of $\geq$ 27 dB for the entire investigated temperature and current range as shown in Fig. 4.7. The full-width at half- maximum (FWHM) is narrower than 0.125 cm^{-1}, limited by the spectrometer resolution. The emission spectra measured at a constant injection current of 680 mA and at different temperatures between 180 K and 245 K revealed a linear tuning of the center frequency from 1116.80 cm^{-1} to 1113.63 cm^{-1} with a tuning coefficient $\frac{1}{\nu}\frac{\Delta\nu}{\Delta T} = -6.98 \cdot 10^{-5}$ K^{-1}. The refractive index deduced using the Bragg wavelength λ_B and extrapolated to room-temperature using this tuning coefficient is $n_{eff} = \frac{\lambda_B}{2\Lambda} = 3.14$. The difference with the theoretical value of $n_{eff} = 3.18$ is attributed to an uncertainty in the refractive index of each individual layer and the evaluation of the Bragg wavelength. At a constant temperature of

203 K, the emission frequency shifts from 1118.48 cm^{-1} to 1116.80 cm^{-1} for various drive currents ranging from 500 mA to 680 mA with a linear tuning coefficient of $\Delta\nu/\Delta P = -0.764$ cm^{-1} W^{-1}. Since the emission frequency is a function of the temperature (which changes the averaged refractive index across the entire laser structure), we can deduce a thermal resistance R_{th} of the device with the above tuning coefficients using $R_{th} = \frac{\Delta T}{\Delta P} = \frac{\Delta\nu}{\Delta P} \cdot \left(\frac{\Delta\nu}{\Delta T}\right)^{-1}$ and find $R_{th} = 9.8$ K/W.

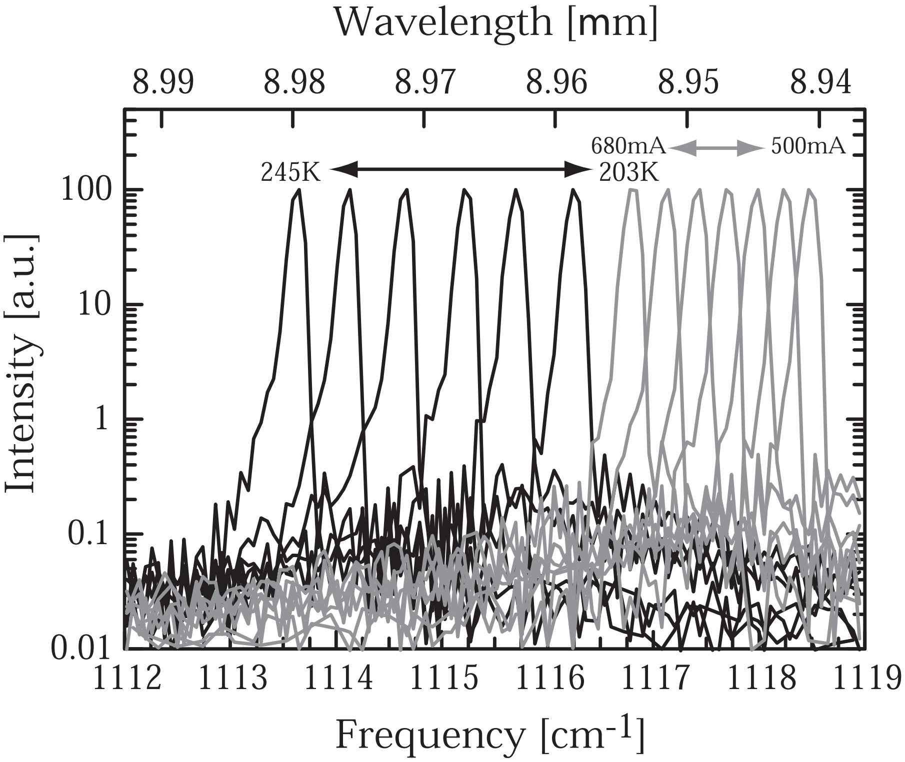

Figure 4.7: Series of high resolution CW spectra of the 1.5mm-long uncoated DFB device as a function of the temperature (T = 203, 212, 219, 225, 232, 239 and 245 K) at a constant drive current of 680 mA (black curves) and as a function of various drive currents ranging between 500 mA and 680 mA in steps of 30 mA at a constant temperature of 203 K (gray curves). The curves are normalized to the emission spectrum measured at 203 K, 680 mA. We deduced the two linear tuning coefficients $\Delta\nu/\Delta T = -0.078$ cm^{-1}/K and $\Delta\nu/\Delta P = -0.764$ cm^{-1} W^{-1}.

Following the model derived in 4.3.2 [41], the temperature dependence of the CW threshold current can then be predicted from the one measured in pulsed mode. The result of this procedure is displayed in Fig. 4.8. The small discrepancy between the measured CW threshold current and the calculated curve is probably due to the strong trapezoidal shape of the laser. The top width of the laser stripe is 6 to 8 μm and more than 18 μm on the bottom of the active region, as measured with an optical microscope. Using the trapezoidal shape of the active region, the refractive index and the overlap factor resulting from the calculation are respectively $n_{eff} = 3.18$ and $\Gamma = 46\%$. The effective index of the optical modes depends on a weighted average of the temperatures of the whole structure (including claddings), whereas the threshold current density will be controlled by the active region temperature only. For such a shape, the effective thermal resistance of the device becomes higher than the one extracted from the spectra. Moreover, narrow stripes will potentially lead to an increase of the top contact resistance and to leakage currents. These effects can also explain the slightly worse temperature behavior and the higher voltage bias of the DFB lasers compared to the Fabry-Pérot (FP) lasers fabricated with the same epilayer [41].

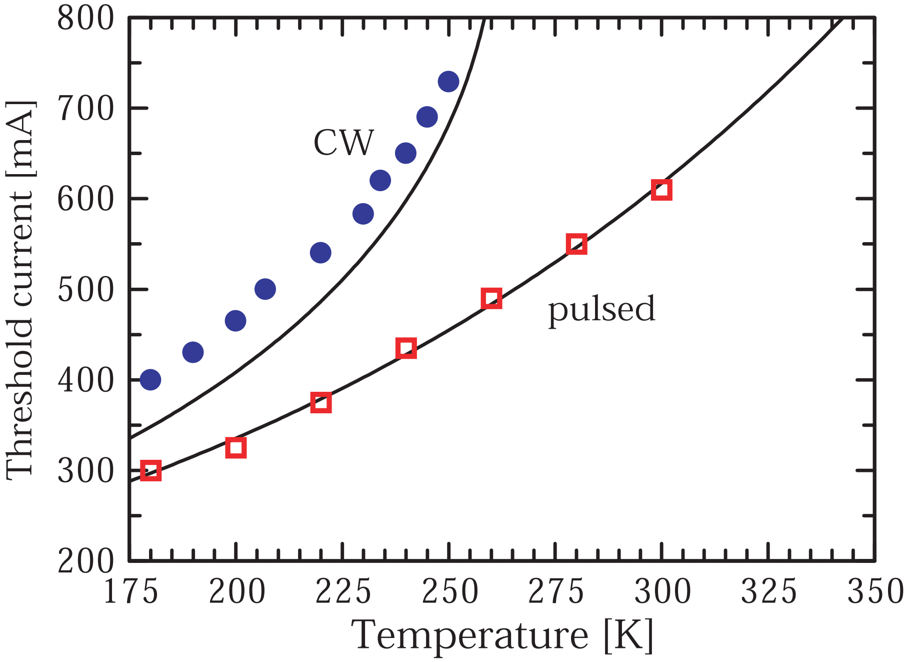

Figure 4.8: Threshold current as a function of heat sink temperature. The experimental pulsed data (open squares) are fitted by the relation $I_{th} = I_0 \cdot exp(T_{act}/T_0)$, with a characteristic temperature $T_0 = 164$ K and $I_0 = 99$ mA (lower solid line). Solid circles represent experimental CW threshold currents. The upper solid line is the dependence of the CW threshold current as a function of the heat sink temperature computed from the thermal model.

In Fig. 4.9 we present subthreshold continuous-wave luminescence spectra of the same device at 180, 200 and 220 K. The envelope of the Fabry-Pérot fringes is centered at about 1116 cm^{-1} with a spacing of the Fabry-Pérot modes of 0.98 cm^{-1}. The Bragg reflector's stopband width is $\Delta(\frac{1}{\lambda}) = 1.19$ cm^{-1} and located at 1120.3 (180 K), 1119.0 (200 K) and 1117.2 cm^{-1} (220 K). This allows us to deduce a grating coupling coefficient of $\kappa = \Delta\lambda\pi n_{eff}/\lambda^2 = 12$ cm^{-1}, using the experimental value of $n_{eff} = 3.14$. Based on the modal refractive index difference $\Delta n_{eff} = 1.1 \cdot 10^{-2}$, we obtain $\kappa = \Delta n_{eff}\pi/2\lambda = 19$ cm^{-1}. The higher calculated value can be attributed to non-ideal trapezoidal grating shape with less than 50 % duty-cycle. With the length of the device ($L = 1.5$ mm), we get $\kappa L = 1.8$ corresponding to a good single-mode operation efficiency and a SMSR of 30 dB [106] as obtained experimentally.

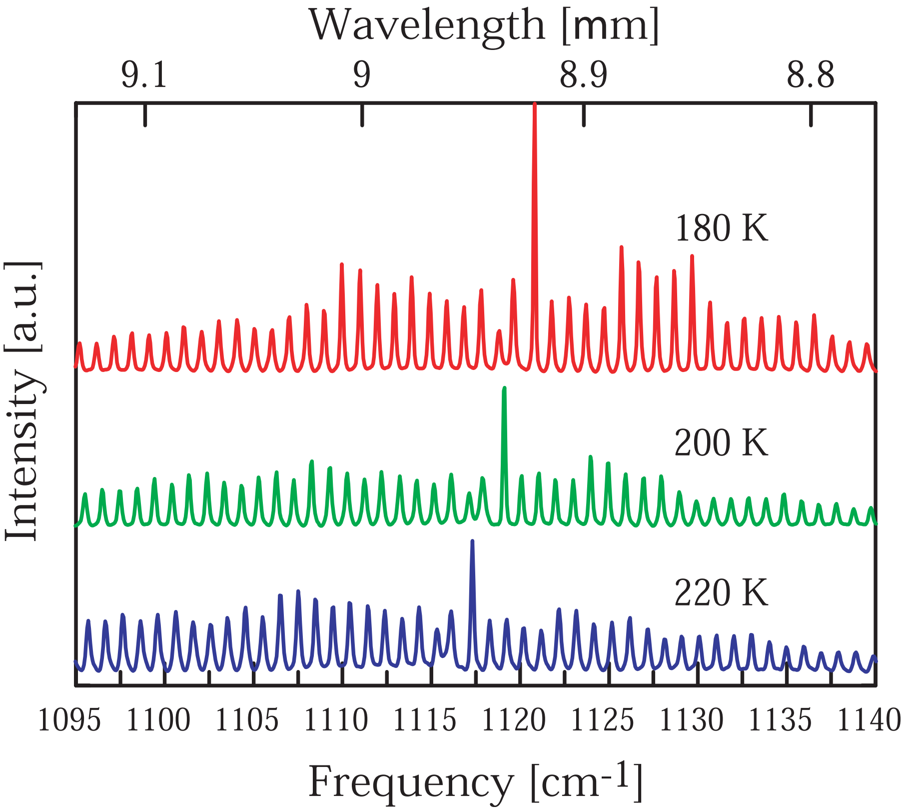

Figure 4.9: Subthreshold CW luminescence spectra at 180, 200 and 220 K. The curves are vertically displaced for clarity.

Because of the trapezoidal cross-section of the laser ridge, normalisation of the usual laser parameters such as threshold current density per unit area is somewhat arbitrary. As a comparison, the FP lasers from the same epilayer [41], using the same mounting and fabrication procedure, exhibit a linearly depending threshold current with laser width between 12 μm and 28 μm. The threshold current of the DFB laser reported here is comparable to a laser of 9-10 μm width accepting such a linear behavior. But assuming the electrical scaling of the current density versus the voltage curves with the FP lasers, the width of the DFB laser is estimated to 6-7 μm, which actually corresponds to the top active region width. The higher threshold current can be explained by the reduced overlap factor Γ (46 %) of the strong trapezoidal shape (see above) compared with the FP lasers ($\Gamma = 56\%$). Finally, supposing an identical thermal conductance as found for the FP lasers (G_{th} = 574 W/ (K cm^2)), the thermal resistance of the DFB laser (R_{th} = 9.8 K/W) gives a laser width of 11-12 μm. This higher value can be explained by a large contact area between the active region and the lateral InP regrowth resulting in a higher heat dissipation.

4.4 DFB-QC lasers emitting around 5.4 μm based on a bound-to-continuum active region

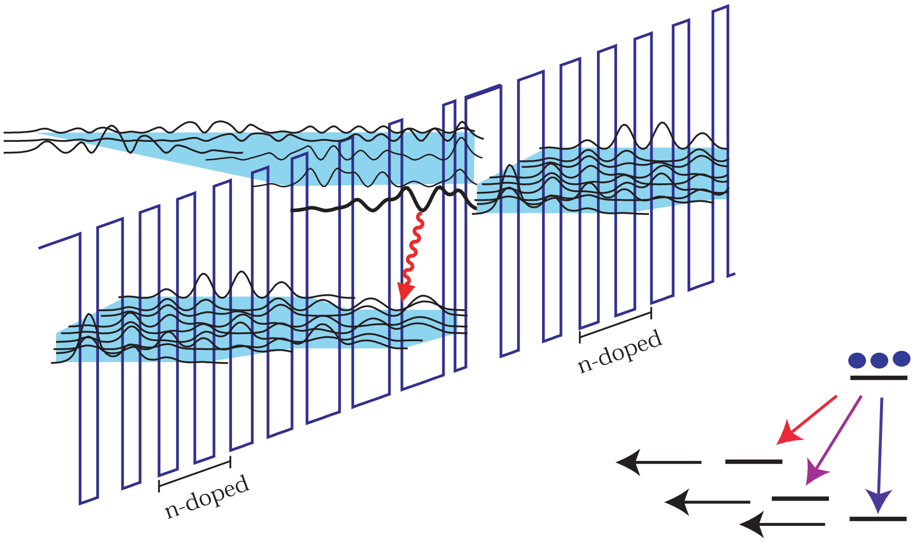

Figure 4.10: Schematic conduction band diagram of one stage of the structure under an applied electric field of 6.7 × 10^4 V/cm. The moduli squared of the relevant wave functions (in bold the upper state of the laser transition) are shown and the wavy arrow indicates the radiative transition. The layer sequence of one period of the structure, in nanometers and starting from the injection barrier, is **4.2**/1.3/**1.4**/ 5.0/**1.5**/4.4/**1.6**/3.9/**1.8**/2.9/**1.9**/2.6/ <u>**2.0**/2.3/**2.1**/2.2</u>/**2.3**/2.1/**3.0**/2.1 where $In_{0.44}Al_{0.56}As$ barriers are in bold, $In_{0.6}Ga_{0.4}As$ wells in roman and underlined numbers correspond to the doped layers.

The distributed feedback QC laser (Alpes Lasers SA, n419b12) used in the experiments of this paragraph are based on a bound-to-continuum design[110, 26, 68] as illustrated in Fig. 4.10. The heterostructure consists of strain-compensated $\mathrm{In_{0.6}Ga_{0.4}As}$ / $\mathrm{In_{0.44}Al_{0.56}As}$ layers on an n-doped InP substrate [27]. 25 active periods were grown, containing the partially n-doped injector region (Si, $\mathrm{n} = 1.0 \times 10^{17}\ \mathrm{cm}^{-3}$) and an undoped four quantum-well gain region,

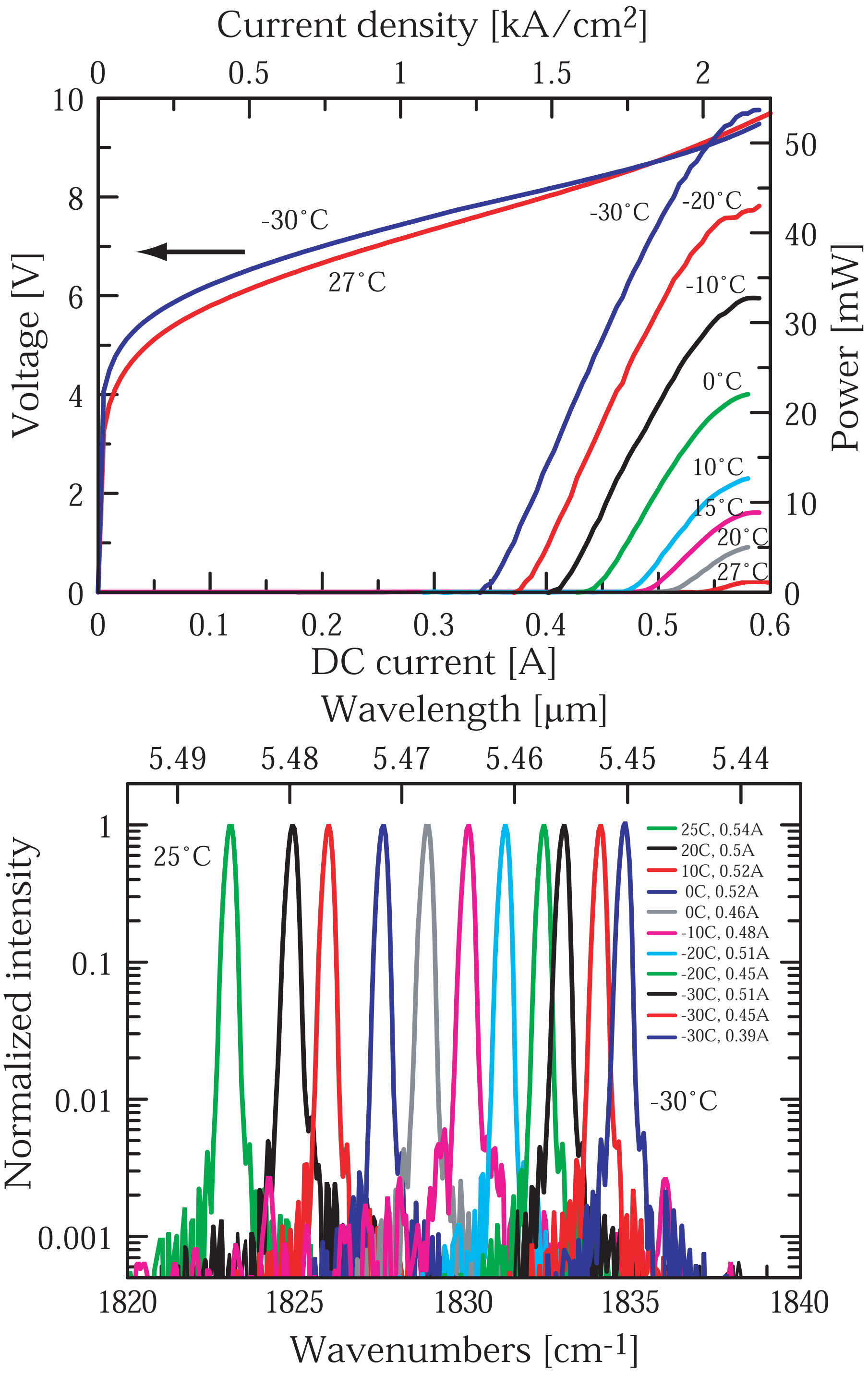

Figure 4.11: a) Optical power vs current of a 1.5 mm-long, 18 μm-wide DFB laser in CW mode for various heatsink temperatures ranging from -30 to 27°C and its voltage vs current curves at -30 and 27°C. b) High-resolution single-mode CW spectra as a function of temperature and injection current between -30 and 25°C (from the right to the left). With courtesy of Alpes Lasers SA.

The waveguide consists of an InGaAs bottom cladding layer (Si, n = 6×10^{16} cm^{-3}, thickness 0.2 μm), followed by the active region, and an upper InGaAs layer (Si, n = 6×10^{16} cm^{-3}, thickness 0.3 μm), which is the host layer of the etched DFB grating. These layers are grown by MBE and are followed by an InP top cladding (Si, n = 1×10^{17} cm^{-3}, thickness 2 μm), an InGaAs contact layer (Si, n = 7×10^{18} cm^{-3}, thickness 0.4 μm) and a highly doped InGaAs layer (Si, n = 1×10^{19} cm^{-3}, thickness 50 nm) grown by MOVPE. The DFB grating has a period of $\Lambda = 861.3$ nm ($n_{eff} = 3.129$, at 26°C). After MOVPE growth, the DFB lasers are fabricated into 12 to 18-μm-wide ridge waveguide devices by standard lithography processes. The substrate was then thinned down to $\sim 150\mu$m, and back contacts were evaporated. We then cleaved 1.5-mm-long bars and mounted them epi-up on copper heatsinks using indium paste. The QC lasers are mounted in a TE-cooled holder (LLH200, Alpes Lasers SA), the output power was measured by a calibrated thermopile detector and the spectra were recorded with an FTIR (Bruker Vertex 70) equipped with a DTGS detector.

As shown in Fig. 4.11 a), a 1.5 mm-long, 18 μm-wide, junction-up mounted DFB laser reaches a maximum operating temperature of 27°C with an output power of 1.2 mW and a threshold current density of 2.01 kA/cm^2. At -30°C, this device emits up to 54 mW with a threshold current density of 1.28 kA/cm^2. The temperature dependence of the CW threshold current density leads to a characteristic temperature of $T_0 = 170$ K, which is comparable with typical values in pulsed mode.

CW spectra collected using the FTIR are shown in Fig. 4.11 b). A single-mode emission is observed over the entire investigated temperature and current ranges, with a sidemode suppression ratio (SMSR) $>$ 25 dB and a full width at half maximum (FWHM) narrower than 0.2 cm^{-1} limited by the spectrometer resolution. The monomode emission spectra between -30 and 25°C reveal a tuning range between 1823.1cm^{-1} and 1835.9 cm^{-1}, i.e. over 12.8 cm^{-1} or 0.7%.

4.5 Upper limit linewidth measurement

In the following paragraph, a method to define the upper limit of the laser linewidth is presented. Spectra are commonly collected using a standard FTIR, with a limited resolution of 0.1 cm^{-1} (3 GHz). In order to obtain a better measurement, the linewidth of a DFB-QC laser is now measured by a heterodyne beating experiment.

In this experiment, which is schematically shown in Fig. 4.12, two collimated CW single mode mid-infrared laser beams, which were emitted by two identical DFB-QC lasers, were collinearly overlaid. After a common optical path length of roughly 1 m, the two beams were focalized onto a fast Mercury Cadmium Telluride (MCT) detector (Vigo Systems, PEM-L-3). The mixing of the two lasers results in a beating spectrum displayed on a spectrum analyzer (Agilent E4407B). The beating frequency corresponds then to the difference of the two optical frequencies and allows a measurement of $\Delta\nu$ down to the MHz range.

Similar devices as the ones presented in the latter section, with 1.5 mm-long and 14 μm-wide mounted junction-up mounted chips emit a maximum power of 48 mW at a temperature of -30°C. Single-mode emission is observed at -30°C for a tuning range from 1828 cm^{-1} to 1832 cm^{-1}. For the experiment, the two nominally identical devices are operated under constant current of 461 mA at 263 K for the first laser (the reference) and of 316 mA at 243 K for the second laser (without the added modulation). The dc powers were generated by stabilized current sources (ILX Lightwave, LDC-3744 and LDX-3232) and the temperatures were controlled by Peltier coolers. Under these conditions, single mode emission at 5.46 μm with average optical powers of 5 and 10 mW respectively are observed.

The mixing of two beams is obtained by the overlaying of two parallel beams. The alignment of the beams from far behind the beam splitter ($\sim$5 m) on a sensitive and small size cooled detector guarantees parallel beams. In parallel, the optimization of the signal with a fine adjustment of the beam splitter on a second removable detector close behind the latter ensures an ideal overlap of the beams. The optical components are aligned with the help of the reference laser, and then the test laser is superimposed by the use of the beam-splitter. Finally, care was taken to avoid optical feedback in the QCL's by introducing a slight misalignment to the fast detector.

The mixing of the two lasers results in a beating spectrum. Acquired at 100 MHz with a sweep time of 5 ms and a resolution bandwidth of 1 MHz, a typical beat note has a full width at half maximum of 6 MHz as shown in Fig. 4.13. The measured linewidth is attributed to fluctuations in the drive current and, to a lesser extent, to the temperature stabilization.

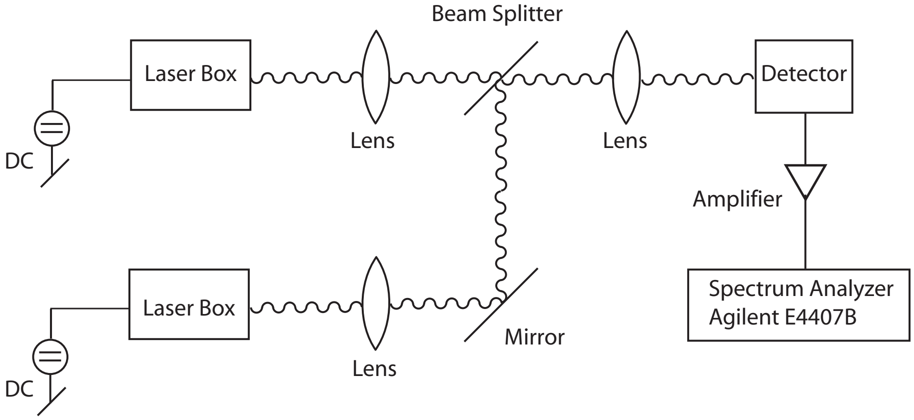

Figure 4.12: Schematic drawing of the optical heterodyne setup. The two QCL beams are overlaid from behind the beam splitter and until they reach the fast MCT detector.

This measure is clearly an upper limit for the laser linewidth. Let us compare this value to the calculated laser linewidth of our device by the formula[70]:

$$\Delta\nu = \frac{\pi h\nu\Delta\nu_c^2}{P}\frac{\alpha_m}{\alpha_{tot}}\frac{n_{2t}}{n_{2t}-n_{1t}}(1+\alpha^2) \tag{4.5.4}$$

where $h\nu$ is the lasing energy, α_{tot} the total losses of the cavity, α_m the mirror losses, P the output power, $\Delta\nu_c = \frac{\alpha c}{2\pi n}$ the full width of half maximum of the cavity resonance, n_{1t} and n_{2t} the populations of the upper and lover states of the laser transition at threshold, respectively, and α the linewidth enhancement factor. Using the rate equation, the expression of the sheet densities can be expressed as followed

$$\frac{n_{2t}}{n_{2t}-n_{1t}} = (1-\frac{\tau_1}{\tau_{21}}-\frac{qn_1^{therm}}{\tau_2 J_{th}})^{-1} \tag{4.5.5}$$

where τ_1 and τ_2 are the lifetimes of the upper and lower states, τ_{21}^{-1} the scattering rate from level 2 to 1, n_1^{therm} the thermal population of level 1, and J_{th} the threshold current density. Introducing our device lifetimes in the latter expression leads to a Schawlow-Townes linewidth on order of 600 Hz. Given the fact that $\Delta\nu$ measured is 10^4 times as large as the theoretical linewidth $\Delta\nu$, the linewidth determined by the beating experiment as shown in this chapter must be broadened due to thermal effects. Based on standard temperature tuning values of DFB-QC lasers, a temperature instability on the order of 3 mK can be estimated. It becomes thus clear that an improved method for determining the correct linewidth of such devices needs to be implemented, This will be done in the following chapters.

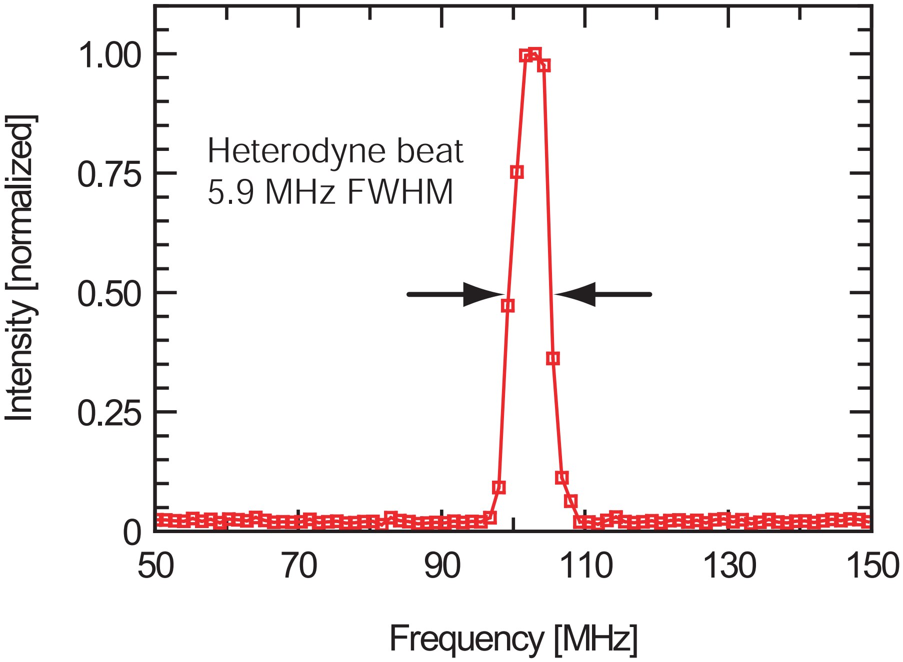

Figure 4.13: RF spectrum of heterodyne beating between the two CW DFB QC lasers mixed onto a high-speed HgCdTe detector.

Chapter 5

Direct intensity modulation of QC lasers

Direct intensity modulation of QC lasers by modulating the injection current is investigated in this Chapter. The main motivation for the realization of such a high-frequency setup operating near room temperature and using Peltier cooling is the direct measurement of the linewidth enhancement factor. This part of the work will be described in the following Chapter. On the other hand, such a setup will also be interesting for potential applications such as high-speed free-space optical telecommunication [111, 112] systems or frequency modulation spectroscopy [113].

The high frequency generation limits of the laser housing used for these measurements were first characterized with a narrow linewidth (5.4 μm) photovoltaic quantum cascade detector operating up to 16 GHz and being developed in the group of D. Hofstetter and M. Graf. Subtraction of the detector response measured in a direct modulation experiment from the one obtained in a heterodyne measurement resulted in a 'housing characteristics' for high frequency generation. A simple electrical RLC circuit was used to explain the 2 GHz (3 dB point) frequency limitation; it showed good agreement with the experimental data. Rather than being based on the physics of intersubband devices (see Theory), the overall system limitation is attributed to the QC laser top contact metallization as well as the inductance of the bonding wires.

For having access to a larger range of laser emission wavelengths (9.1 and 5.4 μm), a commercial high-frequency infrared Mercury Cadmium Telluride (MCT) detector (PEM-L-3 from Vigo Systems) was used in the following experiment. Limited by the electrical frequency response of this particular detector, a direct intensity modulation was measured up to 700 MHz.

In order to increase this frequency limitation even further, an indirect detection based on a commercial Silicon (Si) detector and a non-linear up-conversion in the form of sum-frequency generation was performed. The realization of this experiment was carried out in collaboration with the GAP Optic group of Prof. N. Gisin at Geneva University, by K. Karstad, A. Stefanov, and coworkers. A modulation frequency up to 800 MHz at 9.2 μm was measured; this encouraging result demonstrates the possible use of Si high bandwidth detectors, which are well established in telecommunication systems, for mid-infrared detection.

5.1 High-frequency generation

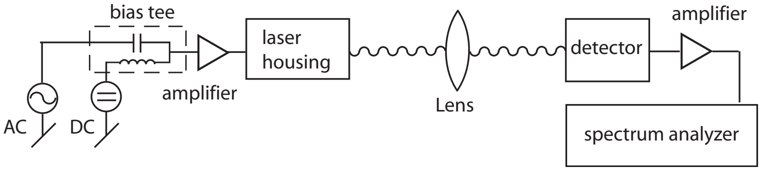

Figure 5.1: Circuit diagram of the experimental high-frequency setup

A schematic picture of the electronics of the direct high-frequency modulation system is displayed in Fig. 5.1. To achieve a direct modulation, a small sinusoidal current modulation is added to the drive direct subthreshold current via a Bias-T and is fed to the QC laser packaged for a high-speed operation. Using lenses, the light output was transmitted to the detector over a distance of 1 m. The resulting photocurrent was amplified and fed into a microwave spectrum analyzer, where the modulation amplitude was measured.

Since cables, connectors, amplifiers, and generators were used well within their specified frequency limits, the losses attributed to them are assumed to be negligibly small. In this configuration, the only contributions to frequency limitation are attributed to the laser and detector packaging. The frequency limitation of the frequency generation system is first calibrated by a high-frequency photovoltaic detector.

5.1.1 Calibration with a photovoltaic detector

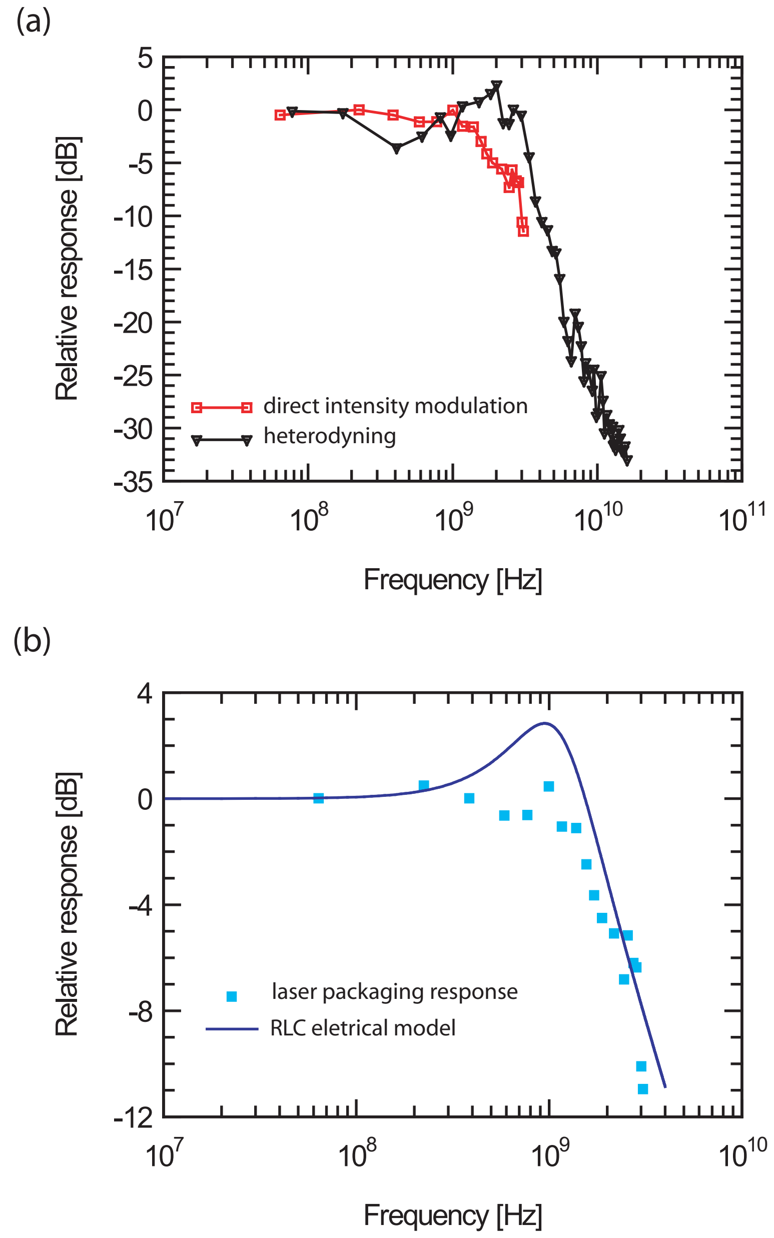

Figure 5.2: (a) Frequency response of the photovoltaic detector by heterodyning (black triangles) and the direct amplitude modulation experiment (red squares). (b) Response of the frequency generation system (blue squares).

A photovoltaic quantum cascade detector utilizes intersubband transitions [114]. The design of this structure is based on an optical transition between two bound states in a single active well. After vertical excitation, the electron in the upper state is injected into a phonon ladder by resonant tunnelling. From there, relaxation into the ground state of the next active region period takes place. The current is characterized by the transport of the excited electrons in one direction only. The particularity of this detector is its narrow linewidth ensured by a vertical bound-to-bound transition (reduced interface scattering). The transition energy is adapted to detect the emission of a bound-to-continuum DFB QC laser emitting at 5.4 μm (described in 4.4).

In order to achieve a high-frequency modulation with constant amplitude for the calibration of the detector response, optical heterodyning was performed by D. Hofstetter and coworkers (see measurement principle in 4.5). As illustrated in Fig. 5.2(a), a frequency limitation of 16 GHz was measured and attributed to the impedance of the contacting 2.5 mm bonding wire. In parallel, a direct modulation intensity experiment was also performed with the same detector as shown in Fig. 5.2(a). This latter experiment was obtained by the modulation of the DFB-QC laser by a 3 GHz bandwidth transmitter (Rhode and Schwarz SML03) at a temperature of -33 C with a dc current of 320 mA (8 mW output power). The collected signal was amplified (MITEQ AFS-5, 26 dB, 21 GHz and HP83006, 26 dB, 26.5 GHz) and acquired by a 26.5 GHz spectral analyzer (Agilent E4407B).

By subtracting the two curves (squares in Fig. 5.2(b)), the frequency response of the generating system is obtained. As the figure shows, the modulation response remains relatively flat up to roughly 1 GHz. As discussed in the following subsection with a simple electrical model, the observed modulation response can be explained entirely by the laser's insufficient high-frequency packaging.

5.1.2 Laser high-frequency packaging

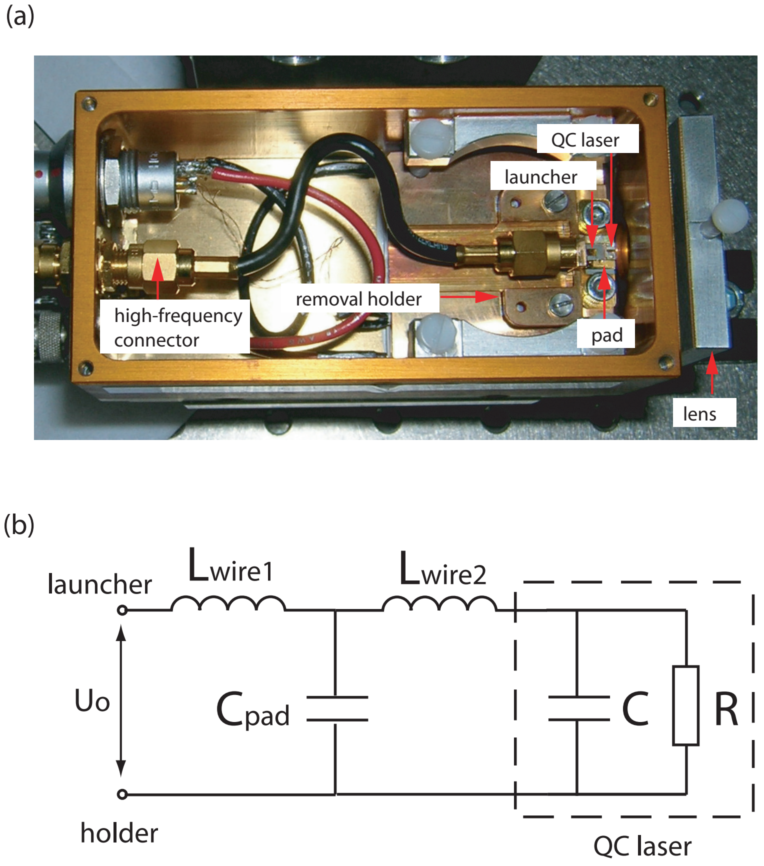

Figure 5.3: (a) Photograph of the high frequency housing setup (b) and corresponding RLC electrical model.

A picture of the laser housing is shown in Fig 5.3(a). The connection between the launcher at the end of the 50-Ohm cable and the laser is ensured via the pad by bond wires. The laser and the launcher are fixed on a copper piece screwed in the plate on the Peltier cooler and can be removed for the bonding. The equivalent RLC circuit is displayed in Fig 5.3(b). According to this model, the ratio between the measured bias and the modulated voltage as a function of frequency, $\frac{U_{meas}}{Umod}(\omega)$, can be described by:

$$\frac{U_{meas}}{Umod}(\omega) = \frac{i\omega RC_{pad}(R + i\omega L_{wire2}(1 + i\omega RC))}{R + i\omega L_{wire2}(1 + i\omega RC) - \omega^2 L_{wire1} C_{pad}(R + i\omega L_{wire2}(1 + i\omega RC))} \tag{5.1.1}$$

where ω is the angular frequency, R=5 Ω is the differential resistance of the laser, C the parasitic capacitance of the laser, and L_{wire1} and L_{wire2} are parasitic inductances of bond wires. Due to its low value (measured a value of 4 pF) and the considered frequency limitation, the capacitance of the pad C_{pad} is negligible (confirmed with similar result obtained with C_{pad}=0 in simulation). On the other hand, we can estimate the value of C, L_{wire1} and L_{wire2} based on the physical dimension. For the capacitance of the laser with a surface of A=480x1500 μm^2, a thickness d=300 nm, and using SiO$_2$ as dielectric (ε=7.5, ε_0=8.85x10^{-12} A s/V m) we get C=$\varepsilon\varepsilon_0$(A/d)=166 pF (the capacitance of the active zone is on the order of 1.5 pF and can be neglected). For a gold wire with a length of l=3 mm and 1.5 mm, a radius r=12.5 μm, and μ_0=4π10^{-7} H/m, we get an inductance of L=(1/2π)μ_0l[ln(2l)/r-1]=3.1 and 1.5 nH respectively. Using the expression of the RLC circuit and these calculated values, the frequency dependence of the packaging of the QC laser housing is plotted in Fig. 5.2(b) and agrees with the experimental curve. Aside from a small resonance peak around 1 GHz, which we ascribed to a too large estimation of C, the experimental data is well fitted by the theoretical curve. On the other hand, the frequency limit is strongly depending on the inductance of bond wires. Therefore, the presently used configuration is not ideal: due to the height of the launcher, long wire bonds are needed to connect the it to the pad. This height was initially planned to connect the launcher directly to the laser without damaging the latter, but bad adhesion of the launcher resulted in a pad for the connection. For very high frequency limits, an optimized impedance matching with microstrip lines should be implemented.

5.2 MCT detector

5.2.1 Large bandwidth detecor

For the purpose of having a detector with a higher room temperature sensitivity and a larger detection wavelength range, high frequency experiments with a commercial Mercury Cadmium Telluride (MCT) detector were performed.

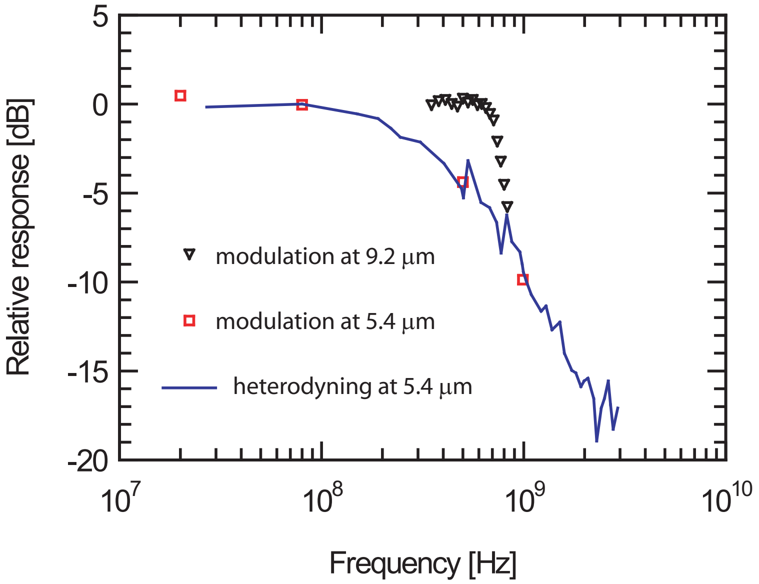

Figure 5.4: Frequency response of the MCT detector at 5.4 μm by heterodyning (blue line) and the direct intensity modulation experiment at 5.4 (red squares) and 9.1 μm (black triangles)

The MCT photodiode is an interband detector based on a semiconductor with a small bandgap energy. Photons with an energy larger than the direct energy gap create electron-hole pairs which are being spatially separated by the internal electrical field across the p-n-junction. Relative to the size of the energy bandgap, the signal detection is in the 2-12 μm range.

To exploit the spectrally broad detection capability, two direct intensity modulation experiments were performed with a QC-BH-laser emitting at 9.1 μm and a QC-DFB-laser emitting at 5.4 μm (similar to those reported in 4.3.3 and 4.5 respectively). The laser emitting at 9.1 μm was modulated (Marconi 2022, 1 GHz, and a 50 dB amplifier, with a total peak to peak amplitude of 0.79 V) at a temperature of -20 C with a constant current of 870 mA. The signal acquired by a 3 GHz spectrum analyzer (Agilent E4402B) after an amplification of 38 dB (Sonoma Instruments 317) is reported in Fig. 5.4. As a result, a cut-off point at 763 MHz is obtained.

A similar detection scheme was used for the modulation experiment (Philips PM 53905, 1 GHz, and a 50 dB amplifier, with a total peak to peak amplitude of 0.4 V) using the 5.4 μm wavelength laser operating with a dc current of 316 mA at a temperature of -30 C. The cut-off frequency of 380 MHz obtained in this latter experiment, see Fig. 5.4, does not agree very well with the measurement at 9.1 μm. The exact reason for this behavior is not clear yet; however, in order to separate at least the influence of the detector itself onto the above experiments, we made an optical heterodyne experiment with one of the lasers.

For this purpose, two similar 5.4 μm wavelength QC-DFB lasers were used (setup and lasers described in 4.4 and 4.5). The comparison of the detector response under optical heterodyning with the one under direct intensity modulation in Fig. 5.4 demonstrates that the frequency limitation is in this case mostly due to the detector. This behavior confirms also the calibration of the high frequency generation with a flat modulation response until 1GHz (Fig. 5.2(b)).

5.2.2 Calibration of the modulation

For the measurements of Henry's linewidth enhancement factor using the technique described in the following chapter, it is important to characterize the modulation of a directly modulated laser. Since higher order harmonics start to occur if the modulation current exceeds the value (I-I_{th}), it is important to know the limit RF amplitude for the laser. The calibration of the modulation was measured at a low modulation frequency of 80 MHz.

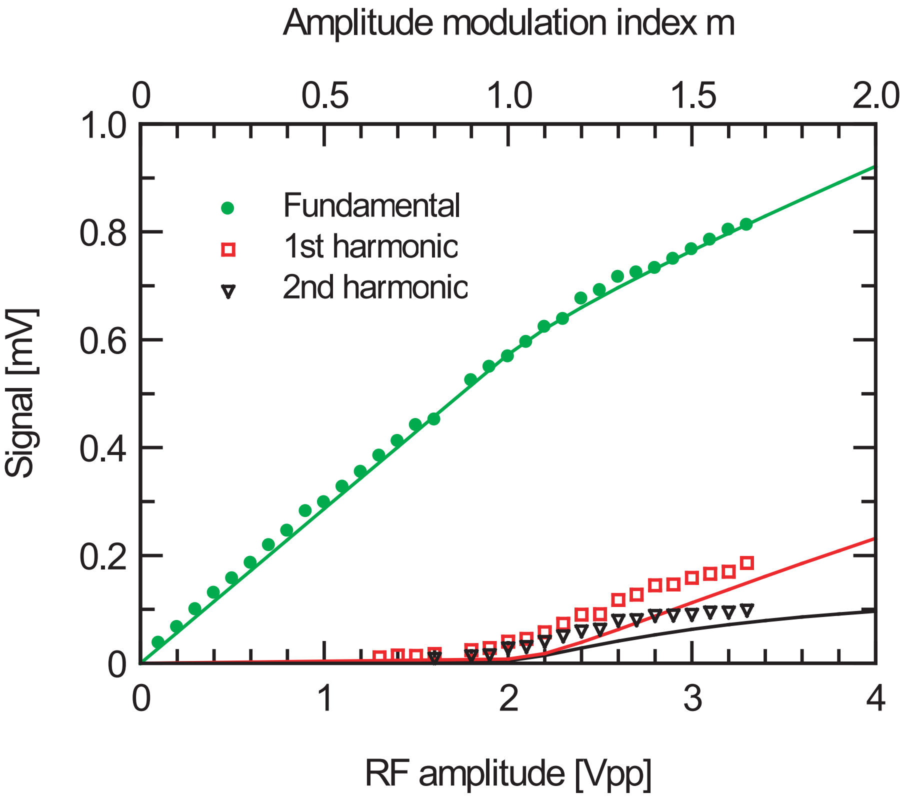

Figure 5.5: The calibration of the amplitude modulation index m

The modulation index m was measured with a direct detection using the fast MCT detector. The calibration of the amplitude modulation index m is achieved by monitoring the strength of the fundamental peak and the first sidebands of the amplitude modulation at the modulation frequency as a function of RF power. All these peaks have been measured with an RF spectrum analyzer. Such sidebands start to show up as soon as the sinusoidal modulation leads to a drop of the injection current below the lasing threshold. A change in slope of the linear dependence between amplitude of the fundamental frequency peak and the RF amplitude indicates the point where 100% modulation is achieved (m = 1) as reported in Fig. 5.5. The slight discrepancy of the measurement with the theory is due to the source and harmonic generation for large signal modulation (m > 0.5). A modulation current value of I_{mod}=72 mA peak-to-peak was confirmed by the measured light-current curve. It is clear that heating effects can be made partly responsible for the higher harmonic peaks appearing even below m = 1.0. For this reason, only the size of the fundamental peak was taken into account for the fitting procedure. The latter was based on a Fourier transform of truncated sine-curves.

5.3 Up-conversion to a Si detector

Yet another possibility to detect high frequency modulated signals at mid-infrared wavelengths is the use of an up-conversion in a non-linear optical crystal, and subsequent detection with a standard Si-photodiode. Although no linewidth measurements were performed using this setup, the frequency modulation measurements will be shown here for completeness.

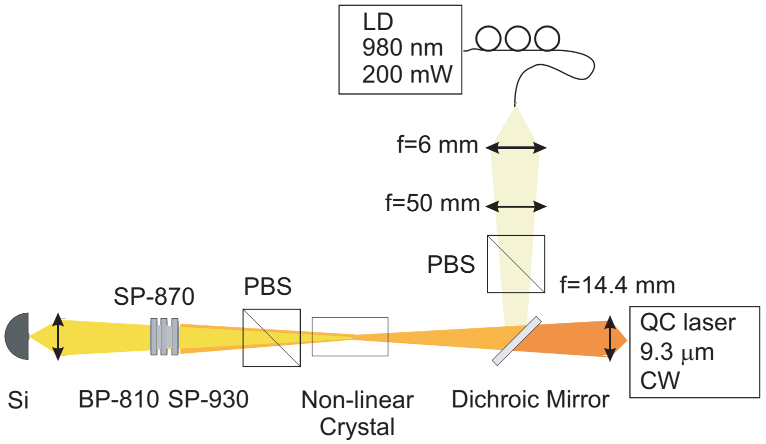

Figure 5.6: Schematic of the experiment of the upconversion detection on a Si detector: the laser diode pump (LD) is focused out of the fiber into the crystal with two lenses. It is overlapped on the mid-IR beam using a Germanium window as a dichroic mirror. The pump is filtered with PBS and filters.

The approach was to detect the radiation indirectly on a Silicon avalanche photo diode (APD), APD-110, from MenloSystems with a quoted bandwidth of 800 MHz, via nonlinear sum-frequency generation. The goal of this approach was to achieve faster detection with a high bandwidth commercial detector.

Fig. 5.6 shows a schematics of the optical path used for an upconversion detection of the

QC laser. The nonlinear up-conversion of the source was done in a Silver Thiagollate (AGS) crystal. The highly divergent QC laser CW source emitting at 9.3 μm was collimated with a high numerical aperture (NA) aspheric Germanium infinite conjugate lens and focused into the crystal with a second aspheric lens. It then entered the APD through a germanium window with 95 % transmission at 9.3 μm and 50 % reflectance at 980 nm. The pump beam for the up-conversion process was provided by a 200 mW pigtailed 980 nm diode laser, delivered through a polarization controller and an APC end-connector. The pump laser was collimated with a standard high NA aspheric lens and passed through a polarizing beam splitter (PBS), selecting the polarization parallel with the source beam. The polarization controller was adjusted to maximize transmission through the PBS. After the PBS, the pump beam was focused into the crystal with a standard lens doublet via reflection on the Germanium window. On the far side of the crystal, we used a second PBS rotated 90 degrees relative to the first one and some filters (a narrow band interference filter, as well as a long and short wavelength pass filter) to block the pump and source beam. A lens doublet was used to focus the up-converted light onto a Si APD with a 500 μm cross-section.

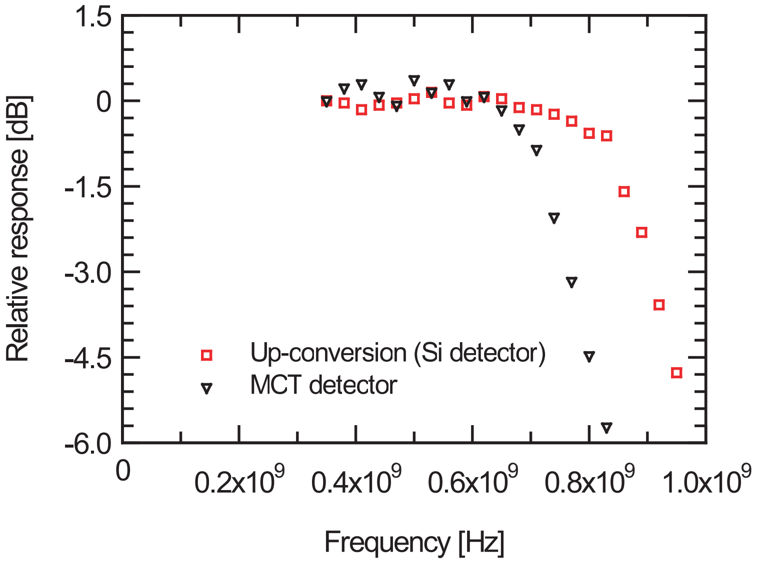

Figure 5.7: Comparison of the frequency response of the MCT (black triangles) and the upconversion system based on a Si detector (red squares)

In the final stage, the signal of the Si detector was amplified with a Sonoma 317 Broadband Amplifier, and connected to a spectrum analyzer used to measure the relative modulation amplitude as shown in Fig. 5.7. An upper frequency limitation up to 800 MHz was achieved for the upconversion technique due to the high bandwidth of the Si detector.

This experiment shows a nice measurement alternative to typical mid-infrared detectors. It uses the well developed Si-based technology used in telecommunication to characterize QC lasers. In particular, single photon counting[115] as well as quantum key distribution[116] have been performed based on this system.

Chapter 6

Direct measurement of the linewidth enhancement factor of QC lasers

As shown in sect. 2.5.2, a direct-current induced intensity or amplitude modulation (AM) results in a simultaneous frequency modulation (FM) in the electric field. A direct measurement of the FM by an optical heterodyne experiment (sect. 4.5) is performed. The mixing of two lasers emitting at closely spaced emission frequencies, which corresponds to an RF beating signal at the frequency difference, is measured on a fast detector and sent to a spectrum analyzer. The ratio between the central line and the first sideband intensities determines the α factor.

For frequencies below 100 MHz, the amount of FM is mainly attributed to the current heating. For higher frequencies, the amount of FM is only due to the carrier-density variation. As for QC laser the carrier variation should not affect the linewidth enhancement factor, no FM should appear on the power spectrum.

6.1 Setup

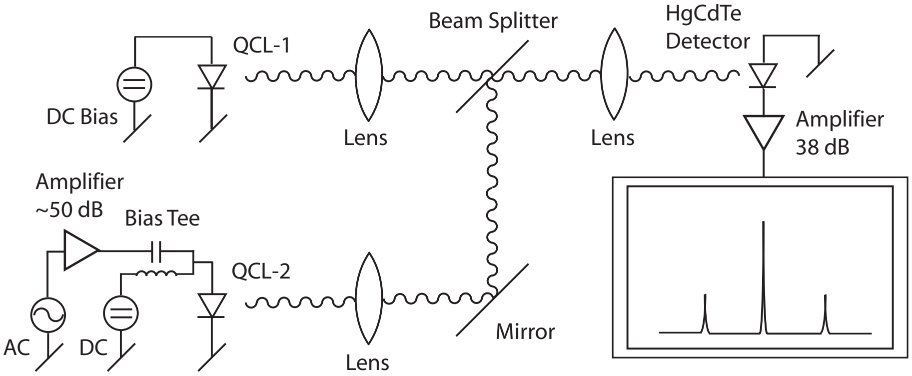

Figure 6.1: Setup for measuring the linewidth enhancement factor α based on heterodyning of a reference distributed feedback quantum cascade laser (QCL-1) with a high-frequency modulated distributed feedback quantum cascade laser (QCL-2). The beams are superimposed by a ZnSe beam splitter and mixed onto a high-speed MCT detector connected to a spectrum analyzer.

We employed a direct measurement of the linewidth enhancement factor that uses a variant of the experiment proposed by Harder et al.[92]. The optical setup is shown schematically in Fig. 6.1. Unlike the original setup, the optical spectrum is no longer measured with a scanning Fabry-Perot interferometer. By using optical heterodyning, we mixed the optical frequency of the laser down to frequencies in the RF range. This allowed us to utilize an RF spectrum analyzer as spectrometer. Heterodyning was obtained by optically mixing a reference distributed feedback (DFB) laser with an AM modulated DFB laser on a fast, room temperature, MCT detector (described in section 5.4). The principal optical components of the setup consist of two ZnSe lenses (f/1 and f/1.5) to collect the two QCL's radiations, a ZnSe beam splitter to superimpose the beams geometrically and a germanium lens (f/2) to focalize and mix them onto the detector. The detector signal is directly displayed in a 9 kHz-3 GHz spectrum analyzer (Agilent, E4402B) via a 38 dB amplifier. The mixing of the two beams depends on some critical alignment procedures to overlay the two beams.

The alignment procedure can be skipped in a first lecture. First, the focal length of the lenses should be precisely determined. This was ensured by aligning the lenses of the two laser beams far behind the beam splitter ($\sim$ 5 m) on a small and sensitive detector. In addition, in order to guarantee a sufficient overlap of the two beams, the beam splitter was horizontally adjusted to maximize the two signals on a detector placed just behind the beam splitter. Once the signals were optimized on the detector used for the alignment, the beams were focused on the fast detector. The latter was tilted to avoid optical feedback in the QC lasers. During the entire procedure, the reference laser was first used to align the optical components, and the beam splitter was used to align the test laser.

The two DFB QC lasers used in this experiment are described in section 4.4. They operate under constant currents of 461 mA at 263 K for the reference laser and of 316 mA at 243 K for the test laser. The electrical powers are generated by stabilized current sources (ILX Lightwave, LDC-3744 and LDX-3232) and the temperatures are controlled by Peltier coolers from commercial suppliers (Alpes Lasers, TC-51). Under these conditions, single mode emissions at 5.46 μm with average optical powers of 10 and 5 mW for the reference and test lasers, respectively, are observed.

6.2 Measurements

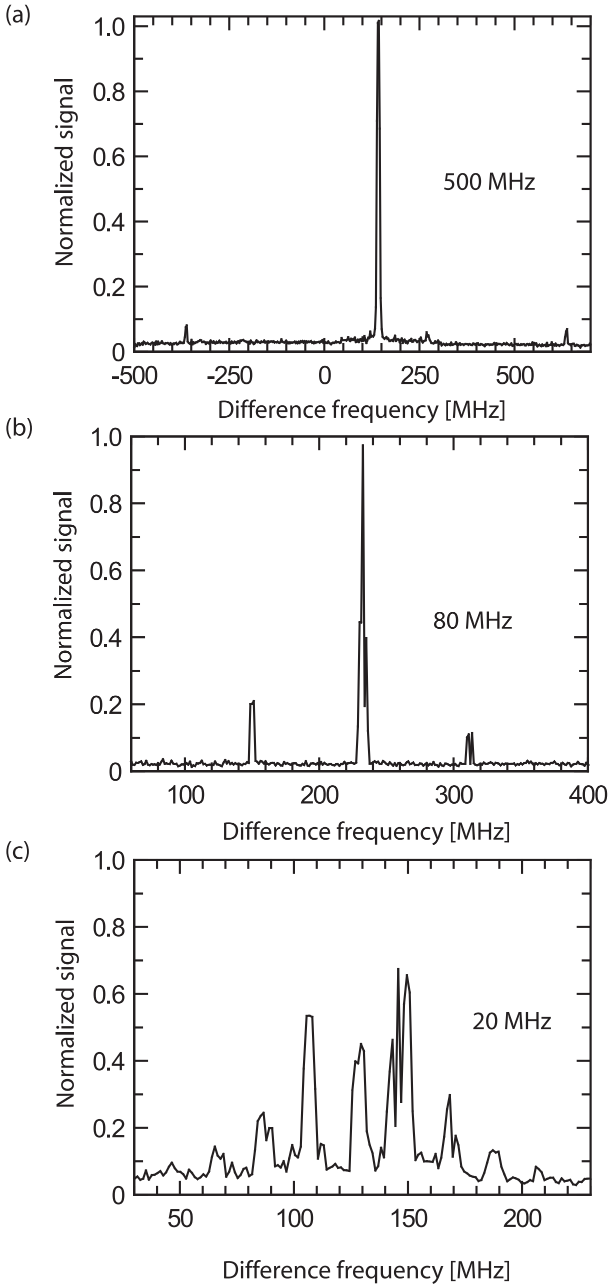

Figure 6.2: Spectra with same modulation index of m=0.4 are reported for three different frequency modulations of (a) 500,(b) 80, (c) 20 MHz. The spectra are normalized with the amplitude of the unmodulated beat note signal.

Normalized optical spectra of the modulated QCL with a modulation index amplitude of $m = 0.4$ and modulation frequencies of (a) 500 MHz (b) 80 MHz and (c) 20 MHz are shown in Fig. 6.2.

At 500 MHz, the spectra show only one pair of symmetric sidebands as expected and illustrated in Fig. 6.3(a). The measured value of the sideband amplitude (0.13) is close to the calculated value for a pure AM modulation (0.1) corresponding to the Fourier transform of Equ. 2.5.21. This result implies a low value of α. The symmetric sideband peaks are explained by the calculated phase of ψ=0 for this specific carrier-density variation.

For lower modulation frequencies, the first sideband amplitudes increase first (80 MHz), followed by the appearance of higher order sidebands (20 MHz) (Fig. 6.2). These results clearly indicate an increase in the amount of FM modulation with decreasing modulation frequency (Fig. 6.3). This behavior is attributed to the thermal chirp described in sect. 2.5.2. The phase associated to this FM behavior is ψ=π, attributed to the delay of the temperature response due the current modulation heating. However, the spectra are not symmetric as it is expected. This is explained by our simple model that predicts an abrupt phase transition at 100 MHz from π to 0 (Fig. 2.4). This transition is in fact a smooth one, and the measurements at 20 and 80 MHz correspond to a phase transition, that implies an uncertainty on the phase and thus on the α factor determination.

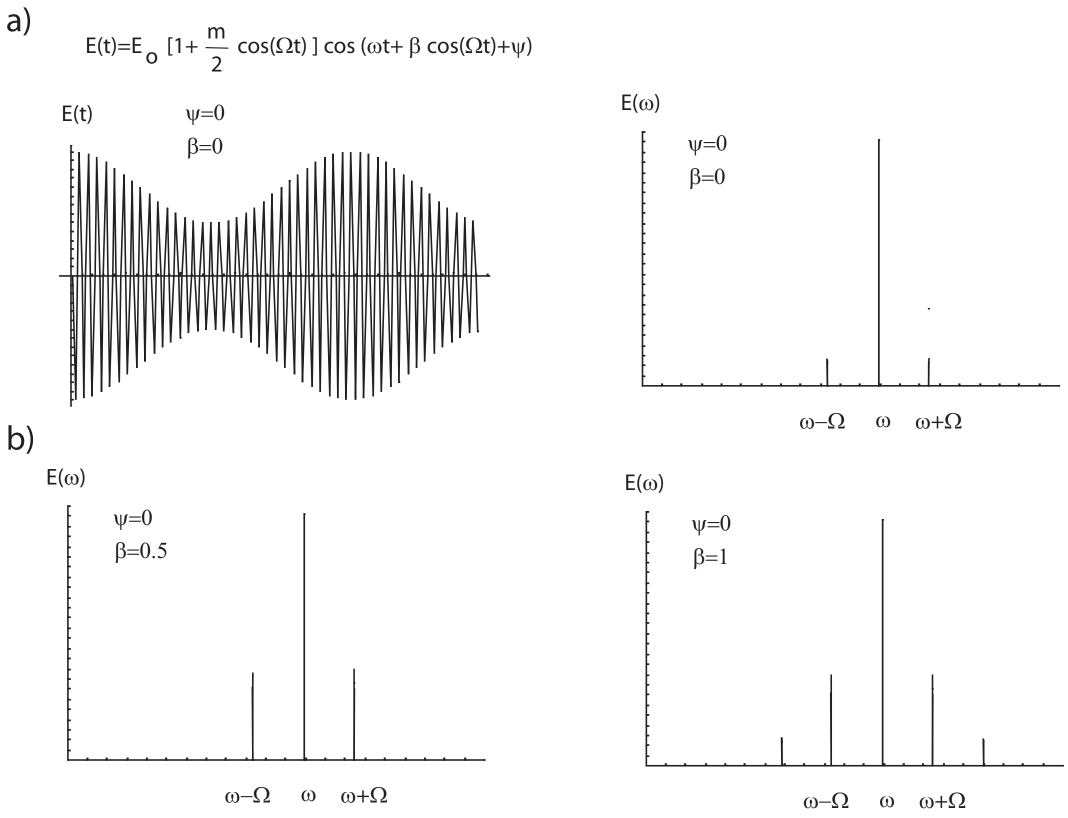

Figure 6.3: a) The time domain display of an AM carrier as well as its associated frequency domain (spectrum analyzer). This is the expected spectrum for high frequency modulation for a negligible α factor. b) Effect of an increasing FM on the spectrum analyzer corresponding to the effect of current modulation heating at low frequencies.

Systematic measurements of the center line and the average of the first sideband peak amplitudes as a function of modulation depth for various frequencies up to 990 MHz are reported in Fig. 6.4. The investigated frequencies are limited by the radio-frequency generator (Philips PM53905). The increasing importance of FM modulation for decreasing frequency is also clearly apparent. This FM modulation is attributed to thermal effects due to the device heating by the current modulation as discussed above.

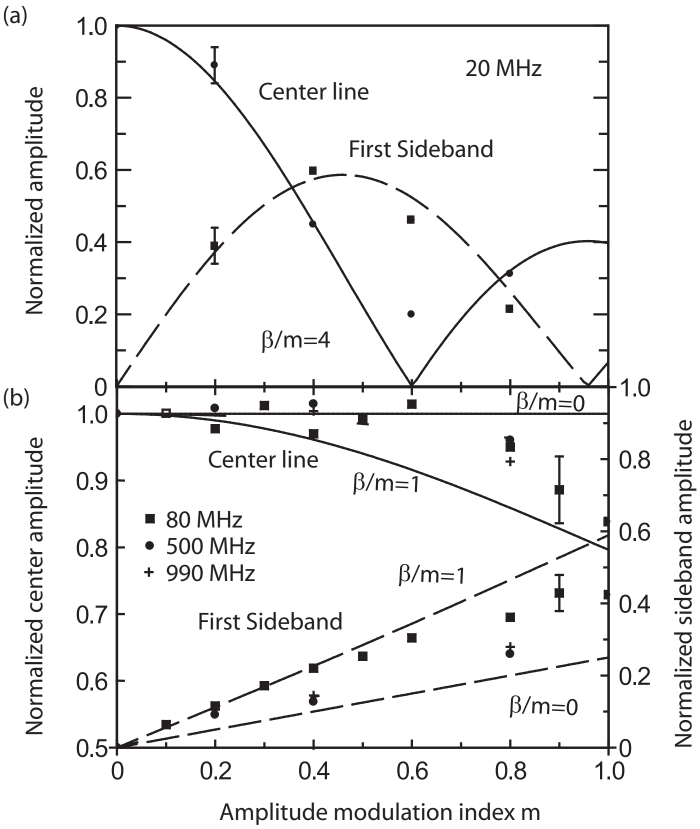

Figure 6.4: (a) Normalized amplitude for the central line (circles) and first sidebands (squares) observed in the power spectra for a modulation frequency of 20MHz. Solid lines correspond to the calculated spectral amplitudes of central line for different values of β. Dashed lines represent the value of first sideband amplitudes. (b) Higher frequency modulations of 80 (circles), 500 (squares), 990 MHz (crosses).

6.3 Spectral analysis

In order to determine α, the amplitude ratio of the first sidebands and the main peak needs to be considered. This is shown by the simulated curves in figure 6.4: the higher the normalized sideband amplitude, the larger the linewidth enhancement factor.

The detected signal of the mixing of the fields of the modulated (E_m(t) from Equ. 2.5.21) and the reference lasers ($E_r(t) = E_2 \cos(\omega_2 t)$, where E_2 is the amplitude and ω_2 the frequency of the reference laser), is given by

$$I(t) = \frac{1}{T_{det}} \int_{T_{det}} |E_m(t) + E_r(t)|^2 dt = \int_{T_{det}} (E_m^2(t) + I_{mr}(t) + E_r^2(t)) dt \tag{6.3.1}$$

where T_{det} is the integration time of the detector. Due to the bandwidth limit of the detector and the sampling at T_{det} ($\omega_1 - \omega_2 \ll \frac{2\pi}{T_{det}}$), the detected intensity is approximated by the mixing product $I_{mr}(t)$. To obtain this latter, the modulated field E$_m$(t) is expanded into Bessel's functions (in general, by the use of Chowning's formula, $\cos[\omega t + \beta \sin(\Omega t + \theta) + \varphi] = \sum_k J_k(\beta) \cos([(\omega + k\Omega)t + k\theta] + \varphi)$, where J_k are the n^{th} order Bessel functions) and the amplitudes $I_{mr}^0(\omega_1 - \omega_2)$ for the center line and $I_{mr}^0(\omega_1 - \omega_2 \pm \Omega)$ for the first sidebands are calculated. By doing so, spectral densities of the radiation at the center frequency ω_1 - ω_2 and of the first sidebands at $(\omega_1 - \omega_2) \pm \Omega$ are given by

$$\begin{aligned} I^2(\omega_1 - \omega_2) &= \frac{I_0}{4}[J_0^2(\beta) + m^2 J_1^2(\beta) \cos^2 \psi] && (6.3.2) \\ I^2((\omega_1 - \omega_2) \pm \Omega) &= \frac{I_0}{4}[J_1^2(\beta) + \\ (\frac{m}{4}[J_0(\beta) + J_2(\beta)])^2 &\mp \frac{m}{2} J_1(\beta)[J_0(\beta) + J_2(\beta) \sin \psi]] && (6.3.3) \end{aligned}$$

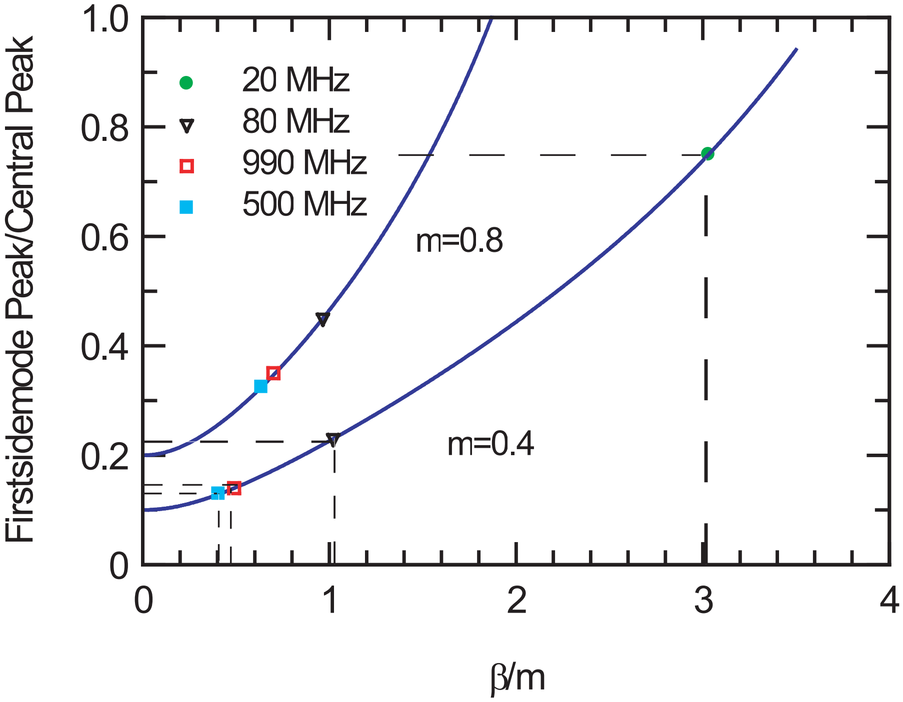

Figure 6.5: Ratio of the sideband peaks by the center line in function of β/m. This relation is given by the Bessel functions calculated by the mixing of two beams.

From these equations, the linewidth enhancement factor α is found graphically by measuring the ratio of the first sideband with the center line amplitude for an intensity modulation index of m=0.4 as represented in Fig 6.5. The corresponding values of α are 8.2 ± 0.5, 2.0 ± 1.0, 0.8 ± 1.4 and 1.0 ± 1.6 for 20, 80, 500 and 990 MHz respectively. They are illustrated with the thermal behavior due to the modulation current heating in Fig. 6.6.

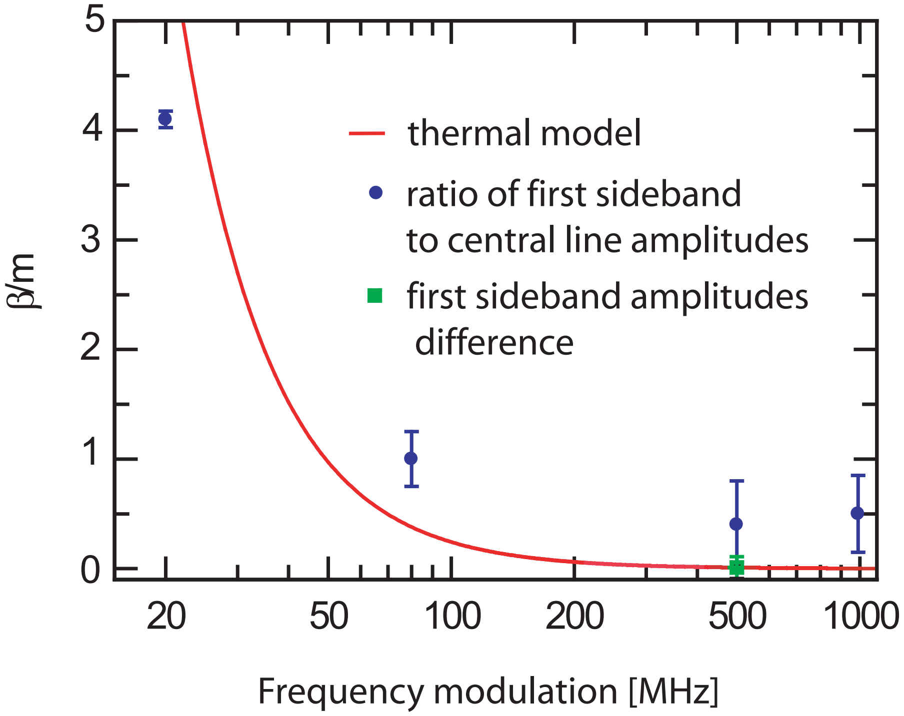

Figure 6.6: Linewidth enhancement factor is plotted as a function of modulation frequency. The first measurement is obtained with the measurement of the ratio of the average of the first sideband to the central peak amplitudes (squares) and the second measurement correspond to the measurement of the difference of first sidebands amplitude (triangles). The solid line corresponds to the thermal model values considering the thermal chirping which is in agreement with the experimental values.

For 500 MHz, the difference of first sideband amplitudes can be used to deduce the carrier density. As the RF source itself seems to increase the sidebands peaks (see the amplitude modulation calibration), this technique results in a better accuracy with a value of α=0.02±0.2.

For a QC laser emission close to its gain peak (5.44 μm), a linewidth enhancement factor of $\alpha = 0.06$ is expected[70]. The accuracy of the present measurements is limited by the current stabilization. Due to current instabilities, the beat note has a large frequency uncertainty. This effect limits the signal integration time and the accuracy on the mean of the sideband amplitudes. A more accurate determination of α is thus expected with a better current stabilization[117]. Additional improvements are potentially possible by the use of an improved laser housing for direct current modulation, and a faster detector with a flat response up to several GHz, for instance a quantum cascade detector. Overall, we have performed a measurement of the linewidth enhancement factor of a mid-infrared QC laser. The experimental result, although having a relatively large uncertainty, confirms the theoretical predication of α being close to zero.

Chapter 7

Conclusions

Quantum cascade lasers are nowadays the most advanced mid- to far-infrared light sources and are even commercially available. Thanks to their rapid development within the last decade, they open new avenues for interesting experiments in basic physics, as well as in applied sciences. Falling in the latter category are all applications of spectroscopy, especially in the mid-infrared wavelength range. Being rather on the basic science side are experiments involving for instance effects of high magnetic fields on the operation of quantum cascade lasers. For the spectroscopy work, most people need lasers emitting in a single longitudinal and lateral mode. The most convenient way to achieve singlemode operation is without any doubt the use of distributed feedback, where an optically periodic structure is introduced into the laser cavity. For precise spectroscopic systems, the knowledge of the laser linewidth constitutes an important piece of information.

While several attempts were made in the past to determine the linewidth of DFB-QC lasers, most of these experiments suffered from either the insufficient precision of the method used of the quality of the laser. In the latter case, the fact that the lasers would function in CW mode only at low temperatures was certainly a large hindrance to make a decent experiment. For this reason, this work focused on two aspects: First, nearly room temperature operated singlemode DFB lasers were fabricated and characterized in terms of threshold current and emission wavelength. Second, these lasers were incorporated into a sophisticated measurement system involving optical heterodyning and direct current modulation.

One big task of the presented work was the optimization of the fabrication procedure, especially in terms of active layer doping, and geometrical optimization of the structure. The correct cross section of the optical waveguide has indeed a big influence on the laser performance, and needs to be controlled more carefully than possible with simple chemical wet etching procedures. Another important aspect is the quality of the regrowth used for fabrication of buried heterostructures. It has turned out that a leakage current-free laser structure based on this concept is not so straight-forward to realize. Several attempts were necessary to come with a growth recipe that resulted in negligibly small leakage currents.

The best devices fabricated during this thesis had threshold currents on the order of 350mA and emitted in the 5.4 μm wavelength region. Several milliwatts of singlemode output power could be observed from such lasers. We then built an optical heterodyne experiment which overlaid two of such singlemode laser beams with closely spaced emission wavelengths. One of the lasers was, in addition, directly current modulated in order to induce, via Henry's α-factor, an additional frequency modulation. The beating between the two lasers was used to being able to measure optical frequency down-converted in the GHz range accessible for an RF spectrum analyzer.

As a main result of this thesis, we obtained a Henry linewidth enhancement factor on the order of 0.2, which is very close to the theoretical prediction. Further improvements of the measurement setup such as temperature stabilization, faster detectors, and better RF modulation capabilities of the laser housing box could lead to a more precise determination of this value.

Acknowledgements

I would like to express my heartfelt thanks to Professor Philipp Aebi for taking time to read my thesis and did me the honour of being my thesis director.

I would like to express my deepest sense of gratitude to Dr Daniel Hofstetter. He provided endless help in bringing this manuscript in its final shape. Without his encouragement, this achievement would never have been possible. He provided various critical comments and suggested many important additions or improvements. It was only because of his continuous support that my work resulted in its present finalised form.

I would like to express my deepest appreciation to Professor Jérôme Faist to give me the golden opportunity to do this work. I am grateful to him to put his valuable knowledge and patience at my disposal and to suggest the topic of this work. It has been a greatly enriching experience to me to work under his creative guidance in the human well-being, work ethic and keen interest atmosphere he inspired in the group.

I would like to warmly thank my colleagues of the crystal growth team to providing the essential and excellent samples for this work, namely Dr Mattias Beck, to whom I am also grateful as grower for his processing assistance and his generous support, Dr Marcella Giovannini and Nicolas Hoyler. Thank you also to Dr Emilio Gini from ETH Zürich to providing the important crystal regrowth required for the buried heterostructure fabrication and additionally to Professor Hans Melchior and Professor Heinz Jäckel.

My special thanks to the member of Professor Jérôme Faist group for their friendship, fruitful discussions, and everyday help and encouragement. In particular, I would like to thank the first former PhD students of the group, Dr Stéphane Blaser, for providing me the figure of the cover of the applied physics letters and his constant full support and great friendship, and Dr Michel Rochat for his creativity through humour and playfulness. I would like also to thank Dr Dmitri Yarekha and Dr Lorenzo Sirigu for our excellent collaboration. Thanks as well to my PhD colleagues, my old and close friend Laurent Diehl, who shared with me the ups and downs of life in and outside the lab during 9 years, my very good friend Giacomo Scalari with who I developed a great complicity in a very few time and who allowed me to take my first steps in Italian language, Lassaad Ajili who shared our office, and likely Richard Maulini, Tobias Gresch, Romain Terazzi and Yuriy Fedoryshyn. All of you have a special place in my mind and I keep such excellent memories of the good times we have spent together. Affectionate thoughts for our dearly departed friend and colleague Harrald Willenberg.

I would like to thank the member of the Dr Daniel Hosfstetter group, Marcel Graf, Esther Baumann and Fabrizio Giorgetta for their help and friendship.

I would like to thank the member of the Alpes Lasers start-up for their friendship and good collaboration, namely Dr Antoine Müller, Dr Yargo Bonetti, Hege Andersen, Dr Lubos Hvozdara, Guillaume Vandeputte and Sophie Brunner.

I would like to thank Professor Nicolas Gisin, Dr Hugo Zbinden, André Stefanov, Ketil Karstad and Gilherme Temporao of Geneva University for our fruitful collaboration.

Also, I would like to thank Professor Frank Tittel and Dr Damien Weidmann of Rice University in Houston for our effective collaboration.

Last but not least, I would like to thanks my parents, my brother and my friends without you none of this would indeed be possible.

This work was supported by the Swiss National Science Foundation.

Bibliography

[1] M. Tacke. Lead salt lasers. In Manfred Helm, editor, *Long wavelength infrared emitters based on quantum wells and superlattices*, volume 6, chapter 9, pages 347–396. Gordon and breach Science, Amsterdam, 2000.

[2] W.W. Bewley, C.L. Canedy, M. Kim, C.S. Kim, J.A. Nodle, J.R. Lindle, I. Vurgaftman, and J.R. Meyer. Interband cascade laser operating to 269k at $\lambda = 4.05\mu$m. *IEE Elect. Lett.*, 43(05):283–284, 2007.

[3] C.L. Canedy, W.W. Bewley, M. Kim, C.S. Kim, J.A. Nolde, D.C. Larrabee, J.R. Lindle, I. Vurgaftman, and J.R. Meyer. High-temperature interband cascade lasers emitting at $\lambda = 3.6 - 4.3\mu$m. *Appl. Phys. Lett.*, 90:181120–1–181120–3, 2007.

[4] M.E. Flatté, J.T. Olesberg, and C.H. Grein. Ideal performance of cascade and noncascade intersubband and interband long-wavelength semiconductor lasers. *Appl. Phys. Lett.*, 75(14):2020–2022, 1999.

[5] D. Weidmann, F.K. Tittel, T. Aellen, M. Beck, D. Hofstetter, J. Faist, and S. Blaser. Mid-infrared trace-gas sensing with a quasi-continuous-wave peltier-cooled distributed feedback quantum cascade laser. *Appl. Phys. B*, 79(07):907–913, 2004.

[6] Z.I. Alferov. Nobel lecture: The double heterostructure concept and its applications in physics, electronics and technology. *Rev. Mod. Phys.*, 73:767–782, 2001.

[7] R.F. Kazarinov and R.A. Suris. Electric and electromagnetic properties of semiconductors with a superlattice. *Sov. Phys. Semicond.*, 6(1):120–131, 1972.

[8] R.F. Kazarinov and R.A. Suris. Possibility of the amplification of electromagnetic waves in a semiconductor with a superlattice. *Sov. Phys. Semicond.*, 5(4):707–709, 1971.

[9] F. Capasso, K. Mohammed, and A.Y. Cho. Resonant tunneling through double barriers, perpendicular quantum transport phenomena in superlattices, and their device applications. *IEEE J. Quantum Electron.*, 22(9):1853–1869, 1986.

[10] P. Yuh and K.L. Wang. Novel infrared band-aligned superlattice laser. *Appl. Phys. Lett.*, 51(18):1404–1406, 1987.

[11] H.C. Liu. A novel superlattice infrared source. *J. Appl. Phys.*, 63(8):2856–2858, 1988.

[12] S.I. Borenstain and J. Katz. Evaluation of the feasibility of a far-infrared laser based on intersubband transitions in gaas quantum wells. *Appl. Phys. Lett.*, 55(7):654–656, 1989.

[13] A. Kastalsky, V.J. Goldman, and J.H. Abeles. Possibility of infrared laser in a resonant tunneling structure. *Appl. Phys. Lett.*, 59(21):2636–2638, 1991.

[14] Q. Hu and S. Feng. Feasibility of far-infrared lasers using multiple semiconductor quantum wells. *Appl. Phys. Lett.*, 59(23):2923–2925, 1991.

[15] G.N. Henderson, L.C. West, T.K. Gaylord, C.W. Roberts, E.N. Glytsis, and M.T. Asom. Optical transitions to above-barrier quasibound states in asymmetric semiconductor heterostructures. *Appl. Phys. Lett.*, 62(12):1432–1434, 1993.

[16] L.C. West and S.J. Eglash. First observation of an extremely large-dipole infrared transition within the conduction band of a gaas quantum well. *Appl. Phys. Lett.*, 46(12):1156–1158, 1985.

[17] M. Helm, E. Colas, P. England, F. DeRosa, and S.J. Allen. Observation of grating-induced intersubband emission from gaas/algaas superlattices. *Appl. Phys. Lett.*, 53(18):1714–1716, 1988.

[18] M. Helm, P. England, E. Colas, F. DeRosa, and S.J. Allen. Intersubband emission from semiconductor superlattices excited by sequential resonant tunneling. *Phys. Rev. Lett.*, 63(1):74–77, 1989.

[19] J. Faist, F. Capasso, D.L. Sivco, C. Sirtori, A.L. Hutchinson, and A.Y. Cho. Quantum cascade laser. *Science*, 264:553–556, 1994.

[20] A. Cho. *Molecular Beam Epitaxy.* AIP Press, Woodbury, NW, 1994.

[21] G. Scamarcio, F. Capasso, C. Sirtori, J. Faist, A.L. Hutchinson, D.L. Sivco, and A.Y. Cho. High-power infrared (8 - micrometer wavelength) superlattice lasers. *Science*, 276:773–776, 1997.

[22] A. Tredicucci, F. Capasso, C. Gmachl, D.L. Sivco, A.L. Hutchinson, and A.Y. Cho. High performance interminiband quantum cascade lasers with graded superlattices. *Appl. Phys. Lett.*, 73(15):2101–2103, 1998.

[23] J. Faist, F. Capasso, C. Sirtori, D.L. Sivco, A.L. Hutchinson, and A.Y. Cho. Vertical transition quantum cascade laser with bragg confined excited state. *Appl. Phys. Lett.*, 66(5):538–540, 1995.

[24] J. Faist, F. Capasso, C. Sirtori, D.L. Sivco, A.L. Hutchinson, M.S. Hybertsen, and A.Y. Cho. Quantum cascade lasers without intersubband population inversion. *Phys. Rev. Lett.*, 76(3):411–414, 1996.

[25] D. Hofstetter, M. Beck, T. Aellen, and J. Faist. High-temperature operation of distributed feedback quantum-cascade lasers at 5.3 μm. *Appl. Phys. Lett.*, 78(4):396–398, 2001.

[26] J. Faist, D. Hofstetter, M. Beck, T. Aellen, M. Rochat, and S. Blaser. Bound-to-continuum and two-phonon resonance quantum cascade lasers for high duty cycle, high temperature operation. *IEEE J. Quantum Electron.*, 38(6):533–546, 2002.

[27] J. Faist, F. Capasso, D.L. Sivco, A.L. Hutchinson, S.G. Chu, and A.Y. Cho. Short wavelength ($\lambda \sim 3.4$ μm) quantum cascade laser based on strained compensated ingaas/alinas. *Appl. Phys. Lett.*, 72(6):680–682, 1998.

[28] R. Colombelli, F. Capasso, C. Gmachl, A.L. Hutchinson, D.L. Sivco, A. Tredicucci, M.C. Wanke, A.M. Sergent, and A.Y. Cho. Far-infrared surface-plasmon quantum-cascade lasers at 21.5 μm and 24 μm wavelengths. *Appl. Phys. Lett.*, 78(18):2620–2622, 2001.

[29] C. Sirtori, P. Kruck, S. Barbieri, P. Collot, J. Nagle, M. Beck, J. Faist, and U. Oesterle. Gaas/al$_x$ga$_{1-x}$as quantum cascade lasers. *Appl. Phys. Lett.*, 73(24):3486–3488, 1998.

[30] L.R. Wilson, D.A. Carder, J.W. Cockburn, R.P. Green, D.G. Revin, M.J. Steer, M. Hopkinson, G. Hill, and R. Airey. Intervalley scattering in gaas-alas quantum cascade lasers. *Appl. Phys. Lett.*, 81(8):1378–1380, 2002.

[31] J. Ulrich, J. Kreuter, W. Schrenk, G. Strasser, and K. Unterrainer. Long wavelength (15 and 23 μm) gaas/algaas quantum cascade lasers. *Appl. Phys. Lett.*, 80(20):3691–3693, 2002.

[32] R. Köhler, A. Tredicucci, F. Beltram, H.E. Beere, E.H. Linfield, A.G. Davies, D.A. Ritchie, R.C. Iotti, and F. Rossi. Terahertz semiconductor-heterostructure laser. *Nature*, 417:156–159, 2002.

[33] C. Walther, G. Scalari, J. Faist, H. Beere, and D. Ritchie. Low frequency terahertz quantum cascade laser operating from 1.6 to 1.8 thz. *Appl. Phys. Lett.*, 89:231121–, 2006.

[34] K. Ohtani and H. Ohno. Inas/alsb quantum cascade lasers operating at 10 μm. *Appl. Phys. Lett.*, 82(7):1003–1005, 2003.

[35] R. Teissier, D. Barate, A. Vicet, C. Alibert, A.N. Baranov, X. Marcadet, C. Renard, M. Garcia, C. Sirtori, D. Revin, and J. Cockburn. Room temperature operation of inas/alsb quantum cascade lasers. *Appl. Phys. Lett.*, 85(02):167–169, 2004.

[36] D.G. Revin, L.R. Wilson, E.A. Zibik, R.P. Green, J.W. Cockburn, M.J. Steer, R.J. Airey, and M. Hopkinson. Ingaas/alassb quantum cascade lasers. *Appl. Phys. Lett.*, 85(18):3992–3994, 2004.

[37] Q. Yang, C. Manz, W. Bronner, K. Köhler, and J. Wagner. Room-temperature short-wavelength ($\lambda \sim 3.7-3.9\mu$m) gainas/alassb quantum-cascade lasers. *Appl. Phys. Lett.*, 88:121127–1–121127–3, 2006.

[38] C. Gmachl, H.M. Ng, and A.Y. Cho. Intersubband absorption in gan/algan multiple quantum wells in the wavelength range of $\lambda \sim$ 1.75-4.2 μm. *Appl. Phys. Lett.*, 77(3):334–336, 2000.

[39] G. Dehlinger, L. Diehl, U. Gennser, H. Sigg, J. Faist, K. Ensslin, D. Grützmacher, and E. Müller. Intersubband electroluminescence from silicon-based quantum cascade structures. *Science*, 290:2277–2280, 2000.

[40] L. Diehl, S. Mentese, E. Müller, D. Grützmacher, H. Sigg, U. Gennser, I. Sagnes, Y. Campidelli, O. Kermarrec, D. Bensahel, and J. Faist. Electroluminescence from strain-compensated $\mathrm{si}_{0.2}\mathrm{ge}_{0.8}$/si quantum-cascade structures based on a bound-to-continuum transition. *Appl. Phys. Lett.*, 81(25):4700–4702, 2002.

[41] M. Beck, D. Hofstetter, T. Aellen, J. Faist, U. Oesterle, M. Ilegems, E. Gini, and H. Melchior. Continuous wave operation of a mid-infrared semiconductor laser at room temperature. *Science*, 295:301–305, 2002.

[42] D. Hofstetter, M. Beck, T. Aellen, J. Faist, U. Oesterle, M. Ilegems, E. Gini, and H. Melchior. Continuous wave operation of a 9.3 μm quantum cascade laser on a peltier cooler. *Appl. Phys. Lett.*, 78(14):1964–1966, 2001.

[43] D.A. Yarekha, M. Beck, S. Blaser, T. Aellen, E. Gini, D. Hofstetter, and J. Faist. Continuous-wave operation of quantum cascade laser emitting near 5.6 μm. *IEE Elect. Lett.*, 39(15):1123–1124, 2003.

[44] J.S. Yu, S. Slivken, A. Evans, L. Doris, and M. Razeghi. High-power continuous-wave operation of a 6 μm quantum-cascade laser at room temperature. *Appl. Phys. Lett.*, 83(13):2503–2505, 2003.

[45] J.S. Yu, S. Slivken, S.R. Darvish, A. Evans, B. Gokden, and M. Razeghi. High-power, room-temperature, and continuous-wave operation of distributed-feedback quantum-cascade lasers at lambda $\sim$ 4.8 μm. *Appl. Phys. Lett.*, 87:041104–1–041104–3, 2005.

[46] W.W. Bewley, J.R. Lindle, C.S. Kim, I. Vurgaftman, J.R. Meyer, A.J. Evans, J.S. Yu, S. Slivken, and M. Razeghi. Beam steering in high-power cw quantum-cascade lasers. *IEEE J. Quantum Electron.*, 41(06):833–841, 2005.

[47] J.S. Yu, A. Evans, S. Slivken, S.R. Darvish, and M. Razeghi. Short wavelength ($\lambda \sim 4.3\mu$m) high-performance continuous-wave quantum-cascade lasers. *IEEE Photon. Technol. Lett.*, 17(06):1154–1156, 2005.

[48] A. Evans, J. Nguyen, S. Slivken, J.S. Yu, S.R. Darvish, and M. Razeghi. Quantum-cascade lasers operating in continuous-wave mode above 90°c at $\lambda \sim 5.25\mu$m. *Appl. Phys. Lett.*, 88:051105–1–051105–3, 2006.

[49] J.S. Yu, S.R. Darvish, A. Evans, J. Nguyen, S. Slivken, and M. Razeghi. Room-temperature continuous-wave operation of quantum-cascade lasers at $\lambda \sim 4\mu$m. *Appl. Phys. Lett.*, 88:041111–1–041111–3, 2006.

[50] J.S. Yu, S. Slivken, A. Evans, S.R. Darvish, J. Nguyen, and M. Razeghi. High power $\lambda \sim 9.5\mu$m quantum-cascade lasers operating above room temperature in continuous-wave mode. *Appl. Phys. Lett.*, 88:091113–1–091113–3, 2006.

[51] J.S. Yu, A. Evans, S. Slivken, S.R. Darvish, and M. Razeghi. Temperature dependent characteristics of $\lambda \sim 3.8\mu$m room-temperature continuous-wave quantum-cascade lasers. *Appl. Phys. Lett.*, 88:251118–1–251118–3, 2006.

[52] S.R. Darvish, W. Zhang, A. Evans, J.S. Yu, S. Slivken, and M. Razeghi. High-power, continuous-wave operation of distributed-feedback quantum-cascade lasers at $\lambda \sim 7.8\mu$m. *Appl. Phys. Lett.*, 89:251119–1–251119–3, 2006.

[53] J.S. Roberts, R.P. Green, L.R. Wilson, E.A. Zibik, D.G. Revin, J.W. Cockburn, and R.J. Airey. Quantum cascade lasers grown by metalorganic vapor phase epitaxy. *Appl. Phys. Lett.*, 82(24):4221–4223, 2003.

[54] R.P. Green, A. Krysa, J.S. Roberts, D.G. Revin, L.R. Wilson, E.A. Zibik, W.H. Ng, and J.W. Cockburn. Room-temperature operation of ingaas/alinas quantum cascade lasers grown by metalorganic vapor phase epitaxy. *Appl. Phys. Lett.*, 83(10):1921–1922, 2003.

[55] M. Troccoli, S. Corzine, D. Bour, J. Zhu, O. Assayag, L. Diehl, B. Lee, G. Höfler, and F. Capasso. Room temperature continuous-wave operation of quantum-cascade lasers grown by metal organic vapour phase epitaxy. *IEE Elect. Lett.*, 41(19):1059–1060, 2005.

[56] L. Diehl, D. Bour, S. Corzine, J. Zhu, G. Höfler, M. Loncar, M. Troccoli, and F. Capasso. High-power quantum cascade lasers grown by low-pressure metal organic vapor-phase epitaxy operating in continuous wave above 400k. *Appl. Phys. Lett.*, 88:201115–1–201115–3, 2006.

[57] L. Diehl, D. Bour, S. Corzine, J. Zhu, G. Höfler, M. Loncar, M. Troccoli, and F. Capasso. High-temperature continuous wave operation of strain-balanced quantum cascade lasers grown by metal organic vapor-phase epitaxy. *Appl. Phys. Lett.*, 89:081101–1–081101–3, 2006.

[58] J. Faist, C. Gmachl, F. Capasso, C. Sirtori, D.L. Sivco, J.N. Baillargeon, and A.Y. Cho. Distributed feedback quantum cascade lasers. *Appl. Phys. Lett.*, 70(20):2670–2672, 1997.

[59] C. Gmachl, F. Capasso, J. Faist, A.L. Hutchinson, A. Tredicucci, D.L. Sivco, J.N. Baillargeon, S.G. Chu, and A.Y. Cho. Continuous-wave and high-power pulsed operation of index-coupled distributed quantum cascade laser at $\lambda \sim 8.5$ μm. *Appl. Phys. Lett.*, 72(12):1430–1432, 1998.

[60] C. Gmachl, F. Capasso, A. Tredicucci, D.L. Sivco, J.N. Baillargeon, A.L. Hutchinson, and A.Y. Cho. High power, continuous-wave, current-tunable, single-mode quantum-cascade distributed-feedback lasers at $\lambda \sim 5.2$ and $\lambda \sim 7.95$ μm. *Opt. Lett.*, 25(4):230–232, 2000.

[61] R. Köhler, C. Gmachl, A. Tredicucci, F. Capasso, D.L. Sivco, S.G. Chu, and A.Y. Cho. Single-mode tunable pulsed, and continuous wave quantum-cascade distributed feedback lasers at $\lambda \sim 4.6$ - 4.7 μm. *Appl. Phys. Lett.*, 76(9):1092–1094, 2000.

[62] R. Köhler, C. Gmachl, F. Capasso, A. Tredicucci, D.L. Sivco, and A.Y. Cho. Single-mode tunable quantum cascade lasers in the spectral range of the co_2 laser at $\lambda = 9.5$ - 10.5 μm. *IEEE Photon. Technol. Lett.*, 12(5):474–476, 2000.

[63] W. Schrenk, N. Finger, S. Gianordoli, L. Hvozdara, G. Strasser, and E. Gornik. Gaas/algaas distributed feedback quantum cascade lasers. *Appl. Phys. Lett.*, 76(3):253–255, 2000.

[64] W. Schrenk, N. Finger, S. Gianordoli, E. Gornik, and G. Strasser. Continuous-wave operation of distributed feedback alas/gaas superlattice quantum-cascade lasers. *Appl. Phys. Lett.*, 77(21):3328–3330, 2000.

[65] D. Hofstetter, M. Beck, T. Aellen, J. Faist, U. Oesterle, M. Ilegems, E. Gini, and H. Melchior. Distributed-feedback quantum cascade lasers emitting in the 9-μm band with inp top cladding layers. *IEEE Photon. Technol. Lett.*, 14(1):18–20, 2002.

[66] T. Aellen, S. Blaser, M. Beck, D. Hofstetter, J. Faist, and E. Gini. Continuous-wave distributed-feedback quantum-cascade lasers on a peltier cooler. *Appl. Phys. Lett.*, 83(10):1929–1931, 2003.

[67] S.R. Darvish, S. Slivken, A. Evans, J.S. Yu, and M. Razeghi. Room-temperature, high-power, and continuous-wave operation of distributed-feedback quantum-cascade lasers at $\lambda \sim 9.6\mu$m. *Appl. Phys. Lett.*, 88:201114–1–201114–3, 2006.

[68] S. Blaser, D.A. Yarekha, L. Hvozdara, Y. Bonetti, A. Muller, M. Giovannini, and J. Faist. Room-temperature, continuous-wave, single-mode quantum-cascade lasers at $\lambda \sim 5.4$ μm. *Appl. Phys. Lett.*, 86:41109–1–41109–3, 2005.

[69] A. Wittmann, M. Giovannini, J. Faist, L. Hvozdara, S. Blaser, D. Hofstetter, and E. Gini. Room temperature, continuous wave operation of distributed feedback quantum cascade lasers with widely spaced operation frequencies. *Appl. Phys. Lett.*, 89:141116–1–141116–3, 2006.

[70] R. Maulini, D.A. Yarekha, J. Bulliard, M. Giovannini, J. Faist, and E. Gini. Continuous-wave operation of a broadly tunable thermoelectrically cooled external cavity quantum-cascade laser. *Opt. Lett.*, 30(19):2584–2586, 2005.

[71] J. Faist, F. Capasso, C. Sirtori, D.L. Sivco, A.L. Hutchinson, and A.Y. Cho. Continuous wave operation of a vertical transition quantum cascade laser above t=80 k. *Appl. Phys. Lett.*, 67(21):3057–3059, 1995.

[72] M. Lerttamrab, S.L. Chuang, C. Gmachl, D.L. Sivco, F. Capasso, and A.Y. Cho. Linewidth enhancement factor of a type-i quantum-cascade laser. *J. Appl. Phys.*, 94(08):5426–5428, 2003.

[73] J. Kim, M. Lerttamrab, S.L. Chuang, C. Gmachl, D.L. Sivco, F. Capasso, and A.Y. Cho. Theoretical and experimental study of optical gain and linewidth enhancement factor of type-i quantum-cascade lasers. *IEEE J. Quantum Electron.*, 40(12):1663–1674, 2004.

[74] J.V. Staden, T. Gensty, W. Elsässer, G. Giuliani, and C. Mann. Measurements of the *alpha* factor of a distributed-feedback quantum cascade laser by an optical feedback self-mixing technique. *Opt. Lett.*, 31(17):2574–2576, 2006.

[75] G. Bastard. *Wave mechanics applied to semiconductor heterostructures.* Les éditions de physique, Les Ulis, France, 1988.

[76] E. Rosencher and B. Vinter. *Optoélectronique.* Masson, Paris, 1998.

[77] C. Sirtori, F. Capasso, J. Faist, and S. Scandolo. Nonparabolicity and a sum rule associated with bound-to-bound and bound-to-continuum intersubband transitions in quantum wells. *Phys. Rev. B*, 50(12):8663–8674, 1994.

[78] D.F. Nelson, R.C. Miller, and D.A. Kleinman. Band nonparabolicity effects in semiconductor quantum wells. *Phys. Rev. B*, 35(14):7770–7773, 1987.

[79] R. Ferreira and G. Bastard. Evaluation of some scattering times for electrons in unbiased and biased single-and multiple-quantum-well structures. *Phys. Rev. B*, 40(2):1074–1086, 1989.

[80] P.J. Price. Two-dimensional electron transport in semiconductor layers i: phonon scattering. *Ann. Phys. (San Diego)*, 133(2):217–239, 1981.

[81] P.J. Price. Two-dimensional electron transport in semiconductor layers ii: screening. *J. Vac. Sci. Technol.*, 19(3):599–603, 1981.

[82] A. Yariv. *Quantum electronics.* John Wiley & Sons, New-York, 3^{rd} edition, 1989.

[83] J. Faist, F. Capasso, C. Sirtori, D.L. Sivco, J.N. Baillargeon, A.L. Hutchinson, S.G. Chu, and A.Y. Cho. High power mid-infrared ($\lambda \sim 5$ μm) quantum cascade lasers operating above room temperature. *Appl. Phys. Lett.*, 68(26):3680–3682, 1996.

[84] J. Faist, F. Capasso, C. Sirtori, D.L. Sivco, A.L. Hutchinson, S.G. Chu, and A.Y. Cho. Narrowing of the intersubband electroluminescent spectrum in coupled-quantum well heterostructures. *Appl. Phys. Lett.*, 65(1):94–96, 1994.

[85] C.H. Henry. Theory of the linewidth of semiconductor lasers. *IEEE J. Quantum Electron.*, 18(02):259–264, 1982.

[86] M. Osinski and J. Buus. Linewidth broadening factor in semiconductor lasers - an overview. *IEEE J. Quantum Electron.*, 23(01):9–29, 1987.

[87] C. Sirtori, F. Capasso, J. Faist, A.L. Hutchinson, D.L. Sivco, and A.Y. Cho. Resonant tunneling in quantum cascade lasers. *IEEE J. Quantum Electron.*, 34(9):1722–1729, 1998.

[88] N. Mustafa, L. Pesquera, C.Y. Cheung, and K.A. Stone. Terahertz bandwidth prediction for amplitude modulation response of unipolar intersubband semiconductor lasers. *IEEE Photon. Technol. Lett.*, 11(5):527–529, 1999.

[89] R. Paiella, R. Martini, F. Capasso, C. Gmachl, H.Y. Hwang, D.L. Sivco, J.N. Baillargeon, A.Y. Cho, E.A. Whittaker, and H.C. Liu. High-frequency modulation without the relaxation oscillation resonance in quantum cascade lasers. *Appl. Phys. Lett.*, 79(16):2526–2528, 2001.

[90] J. Faist, F. Capasso, C. Sirtori, D.L. Sivco, and A.Y. Cho. Quantum cascade lasers. In H.C. Liu and F. Capasso, editors, *Intersubband transitions in quantum wells: Physics and device applications II*, volume 66, chapter 1, pages 1–83. Academic Press, 2000.

[91] S. Kobayashi, Y. Yamamoto, M. Ito, and T. Kimura. Direct frequency modulation in algaas semiconductor lasers. *IEEE J. Quantum Electron.*, 18(04):582–595, 1982.

[92] C. Harder, K. Vahala, and A. Yariv. Measurement of the linewidth enhancement factor α of semiconductor lasers. *Appl. Phys. Lett.*, 42(04):328–330, 1983.

[93] D. Welford and S.B. Alexander. Magnitude and phase characteristics of frequency modulation in directly modualted gaalas semiconductor diode lasers. *IEEE J. Lightwave Technol.*, 3(5):1092–1099, 1985.

[94] Y. Zhang, Y. He, and A. Li. Transient thermal analysis of inalas/ingaas/inp mid-infrared quantum cascade lasers. *Chin. Phys. Lett.*, 20(05):678–681, 2003.

[95] K.L. Campman, H. Schmidt, A. Imamoglu, and A.C. Gossard. Interface roughness and alloy-disorder scattering contributions to intersubband transition linewidths. *Appl. Phys. Lett.*, 69(17):2554–2556, 1996.

[96] T. Unuma, T. Takahashi, T. Noda, M. Yoshita, H. Sakaki, M. Baba, and H. Akiyama. Effects of interface roughness and phonon scattering on intersubband absorption linewidth in a gaas quantum well. *Appl. Phys. Lett.*, 78(22):3448–3450, 2001.

[97] S. Tsujino, A. Borak, E. Müller, M. Scheinert, C.V. Falub, H. Sigg, D. Grützmacher, M. Giovannini, and J. Faist. Interface-roughness-induced broadening of intersubband electroluminescence in p-sige and n-gainas/alinas quantum cascade structures. *Appl. Phys. Lett.*, 86(06):062113–1–062113–3, 2005.

[98] P. Offermans, P.M. Koenraad, J.H. Wolter, M. Beck, T. Aellen, and J. Faist. Digital alloy interface grading of an inalas/ingaas quantum cascade laser structure studied by cross-sectional scanning tunneling microscopy. *Appl. Phys. Lett.*, 83(20):4131–4133, 2003.

[99] S. Barbieri, C. Sirtori, H. Page, M. Stellmacher, and J. Nagle. Design strategies for gaas-based unipolar lasers: Optimum injector-active region coupling via resonant tunneling. *Appl. Phys. Lett.*, 78(3):282–284, 2001.

[100] Q.K. Yang, C. Mann, F. Fuchs, R. Kiefer, K. Köhler, N. Rollbühler, H. Schneider, and J. Wagner. Improvement of $\lambda \sim 5\mu$m quantum cascade lasers by blocking barriers in the active regions. *Appl. Phys. Lett.*, 80(12):2048–2050, 2002.

[101] M. Giehler, R. Hey, H. Kostial, S. Cronenberg, T. Ohtsuka, and L. Schrottke. Lasing properties of gaas/(al,ga)as quantum-cascade lasers as a function of injector doping density. *Appl. Phys. Lett.*, 82(5):671–673, 2003.

[102] M. Giehler, H. Kostial, R. Hey, and H.T. Grahn. Effect of free-carrier absorption on the threshold current density of gaas/ (al,ga)as quantum-cascade lasers. *J. Appl. Phys.*, 96(9):4755–4761, 2004.

[103] V.D. Jovanovic, D. Indjin, N. Vukmirovic, Z. Ikonic, P. Harrison, E.H. Linfield, H. Page, X. Marcadet, C. Sirtori, C. Worrall, H.E. Beere, and D.A. Ritchie. Mechanisms of dynamic range limitations in gaas/algaas quantum-cascade lasers: Influence of injector doping. *Appl. Phys. Lett.*, 86:211117–1–211117–3, 2005.

[104] T. Aellen, M. Beck, N. Hoyler, M. Giovannini, and J. Faist. Doping in quantum cascade lasers. i. inalas-ingaas/inp midinfrared devices. *J. Appl. Phys.*, 100:043101–1–043101–4, 2006.

[105] J. Faist. Wallplug efficiency of quantum cascade lasers: Critical parameters and fundamental limits. *Appl. Phys. Lett.*, 90:253512–1–253512–3, 2007.

[106] H. Kogelnik and C. Shank. Coupled-wave theory of distributed feedback lasers. *J. Appl. Phys.*, 43(05):2327–2335, 1972.

[107] C. Gmachl, J. Faist, J.N. Baillargeon, F. Capasso, C. Sirtori, D.L. Sivco, S.G. Chu, and A.Y. Cho. Complex-coupled quantum cascade distributed-feedback laser. *IEEE Photon. Technol. Lett.*, 9(8):1090–1092, 1997.

[108] J. Faist, A. Tredicucci, F. Capasso, C. Sirtori, D.L. Sivco, J.N. Baillargeon, A.L. Hutchinson, and A.Y. Cho. High-power continuous-wave quantum cascade lasers. *IEEE J. Quantum Electron.*, 34(2):336–343, 1998.

[109] A.A. Grinberg and S. Luryi. Space-charge-limited current and capacitance in double-junction diodes. *J. Appl. Phys.*, 61(3):1181–1189, 1987.

[110] J. Faist, M. Beck, T. Aellen, and E. Gini. Quantum cascade lasers based on a bound-to-continuum transition. *Appl. Phys. Lett.*, 78(2):147–149, 2001.

[111] R. Martini, C. Gmachl, J. Falciglia, F.G. Curti, C.G. Bethea, F. Capasso, E.A. Whittaker, R. Paiella, A. Tredicucci, A.L. Hutchinson, D.L. Sivco, and A.Y. Cho. High-speed modulation and free-space optical audio/video transmission using quantum cascade lasers. *IEE Elect. Lett.*, 37(3):102–103, 2001.

[112] S. Blaser, D. Hofstetter, M. Beck, and J. Faist. Free-space optical data link using peltier-cooled quantum cascade laser. *IEE Elect. Lett.*, 37(12):778–780, 2001.

[113] W. Lenth. Optical heterodyne spectroscopy with frequency- and amplitude-modulated semiconductor lasers. *Opt. Lett.*, 08(11):575–577, 1983.

[114] D. Hofstetter, M. Graf, T. Aellen, J. Faist, L. Hvozdara, and S. Blaser. 23 ghz operation of a room temperature photovoltaic quantum cascade detector at 5.35 μm. *Appl. Phys. Lett.*, 89:061119–1–061119–3, 2006.

[115] G. Temporao, S. Tanzilli, H. Zbinden, N. Gisin, T. Aellen, M. Giovannini, and J. Faist. Mid-infrared single-photon counting. *Opt. Lett.*, 31(08):1094–1096, 2006.

[116] G. Temporao, H. Zbinden, S. Tanzilli, N. Gisin, and J.P. Weid. Feasibility study of free-space quantum key distribution in the mid-infrared. *QIC*, 8(1):1–11, 2008.

[117] M.S. Taubman, T.L. Myers, B.D. Cannon, R.M. Williams, F. Capasso, C. Gmachl, D.L. Sivco, and A.Y. Cho. Frequency stabilization of quantum-cascade lasers by use of optical cavities. *Opt. Lett.*, 27(24):2164–2166, 2002.

Published work

- D. Hofstetter, T. Aellen, M. Beck, and J. Faist, High average power 1st order distributed feedback quantum cascade lasers, IEEE Photon. Technol. Lett. **12**, 1610–1612 (2000).
- J. Faist, M. Beck, T. Aellen, and E. Gini, Quantum-cascade lasers based on a bound-to-continuum transition, Appl. Phys. Lett. **78**, 147–149 (2001).
- D. Hofstetter, M. Beck, T. Aellen, and J. Faist, High temperature operation of distributed feedback quantum cascade lasers at 5.3 μm, Appl. Phys. Lett. **78**, 396–398 (2001).
- D. Hofstetter, M. Beck, T. Aellen, J. Faist, U. Oesterle, M. Ilegems, E. Gini, and H. Melchior, Continuous wave operation of quantum cascade lasers at 9.3 μm on a Peltier cooler, Appl. Phys. Lett. **79**, 1964–1966 (2001).
- D. Hofstetter, M. Beck, T. Aellen, J. Faist, U. Oesterle, M. Ilegems, E. Gini, and H. Melchior, Distributed feedback quantum cascade lasers with InP top cladding layers, IEEE Photon. Technol. Lett. **14**, 18–20 (2002).
- M. Beck, D. Hofstetter, T. Aellen, J. Faist, U. Oesterle, M. Ilegems, E. Gini, and H. Melchior, Continuous wave operation of a mid-infrared semiconductor laser at room temperature, Science **295**, 301–305 (2002).
- T. Aellen, M. Beck, D. Hofstetter, J. Faist, U. Oesterle, M. Ilegems, E. Gini, and H. Melchior, Graded interface 9.3 μm quantum cascade lasers (presented paper), 29th Int. Symp. Compound Semiconductors, Inst. Phys. Conf. Ser. **174**, 455–462 (2002).
- J. Faist, D. Hofstetter, M. Beck, and T. Aellen, Bound-to-continuum and two-phono-resonance quantum-cascade lasers for high duty cycle, high-temperature (invited paper) IEEE J. Quantum Electron. **38**, 533–546 (2002).
- D. Weidmann, L. Joly, V. Parpillon, D. Courtois, Y. Bonetti, T. Aellen, M. Beck, J. Faist, and D. Hofstetter, Free-running 9.1-μm distributed-feedback quantum cascade laser linewidth measurement by heterodyning with a $C^{18}O_2$ laser, Opt. Lett. **28**, 704–706 (2003).

- D. A. Yarekha, M. Beck, S. Blaser, T. Aellen, E. Gini, D. Hofstetter, and J. Faist, Continuous-wave operation of quantum cascade laser emitting near 5.6 μm, IEE Elect. Lett. **39**, 1123–1124 (2003).
- D. Hofstetter, M. Beck, T. Aellen, and S. Blaser, High-frequency modulation of a quantum cascade laser using a monolithically integrated intra-cavity modulator, IEE Photon. Technol. Lett. **15**, 1044–1046 (2003).
- T. Aellen, S. Blaser, M. Beck, D. Hofstetter, J. Faist, and E. Gini, Continuous-wave distributed-feedback quantum-cascade lasers on a Peltier cooler, Appl. Phys. Lett. **83**, 1929–1931 (2003).
- L. Joly, V. Zéniari, B. Parvitte, D. Weidmann, D. Courtois, Y. Bonetti, T. Aellen, M. Beck, J. Faist, and D. Hofstetter, Spectroscopic study of the ν_1 band of SO_2 using a continuous-wave DFB QCL at 9.1 μm, Appl. Phys. B **77**, 703–706 (2003).
- P. Offermans, P. M. Koenraad, J.H. Wolter, M. Beck, T. Aellen, and J. Faist, Digital alloy interface grading of an InAlAs/InGaAs quantum cascade laser structure studied by cross-sectional scanning tunneling microscopy, Appl. Phys. Lett. **83**, 4131–4133 (2003).
- D. Weidmann, F. K. Tittel, T. Aellen, M. Beck, D. Hofstetter, J. Faist, and S. Blaser Mid-infrared trace-gas sensing with a quasi-continuous-wave Peltier-cooled distributed feedback quantum cascade laser, Appl. Phys. B **79**, 907–913 (2004).
- K. Karstad, A. Stefanov, M. Wegmuller, H. Zbinden, N. Gisin, T. Aellen, M. Beck, and J. Faist, Detection of mid-IR radiation by sum frequency generation for free space optical communication Opt. Las. Eng. **43**, 537–544 (2005).
- G. Temporao, S. Tanzilli, H. Zbinden, N. Gisin, T. Aellen, M. Giovannini and J. Faist, Mid-infrared single-photon counting, Opt. Lett. **31**, 1094–1096 (2006).
- D. Hofstetter, M. Graf, T. Aellen, J. Faist, L. Hvozdara, and S. Blaser, 23 GHz operation of a room temperature photovoltaic quantum cascade detector at 5.35 μm, Appl. Phys. Lett. **89**, 061119 (2006).
- T. Aellen, M. Beck, N. Hoyler, M. Giovannini, and J. Faist, Doping in quantum cascade lasers. I. InAlAs-InGaAs/InP midinfrared devices, J. Appl. Phys. **100**, 043101 (2006).
- T. Aellen, R. Maulini, R. Terazzi, N. Hoyler, M. Giovannini, J. Faist, S. Blaser, and L. Hvozdara, Direct measurement of the linewidth enhancement factor by optical heterodyning of an amplitude-modulated quantum cascade laser, Appl. Phys. Lett. **89**, 091121 (2006).
- L. Diehl, B. G. Lee, P. Behroozi, F. Capasso, T. Aellen, D. Hofstetter, M. Beck, and J. Faist, Microfluidic tuning of distributed feedback quantum cascade lasers, Opt. Exp. **14**, 11660–11667 (2006).

- G. Temporao, H. Zbinden, S. Tanzilli, N. Gisin, T. Aellen, M. Giovannini, J. Faist, and J. P. Von der Weid, Feasibility study of free-space quantum key distribution in the mid-infrared, Quant. Info. and Comput. **8**, 1–11 (2008).